# Metal-Insulator Transition in Niobium Dioxide Thin Films

---

A Dissertation

Presented to

the faculty of the School of Engineering and Applied Science

University of Virginia

---

in partial fulfillment

of the requirements for the degree

Doctor of Philosophy

by

Yuhan Wang

May

2017

APPROVAL SHEET

The dissertation

is submitted in partial fulfillment of the requirements

for the degree of

Doctor of Philosophy

Yuhan Wang

AUTHOR

The dissertation has been read and approved by the examining committee:

Jiwei Lu

Advisor

Jerrold Floro

Stuart Wolf

Robert Weikle

Arthur Lichtenberger

Accepted for the School of Engineering and Applied Science:

Craig H. Benson, Dean, School of Engineering and Applied Science

May

2017

# Table of Contents

# Acknowledgement

This dissertation would not have been possible without the support and assistance from many people. First and foremost, I would like to express my gratitude to my advisors, Prof. Jiwei Lu and Prof. Stuart Wolf, for their guidance and mentoring throughout my time at University of Virginia. They have been extremely supportive and encouraging, providing valuable mentorship and insightful feedback on my work.

I would like to thank all the current and former members of the Wolf/Lu group for their collaboration, assistance and friendship, including Salinporn Kittiwatanakul, Ryan B. Comes, Hongxue Liu, Nam Dao, Yishen Cui, Man Gu, Nattawut Anuniwat, Yonghang Pei, and Linqiang Luo. I appreciate their tutoring on experimental tool use, discussion with them on research questions, and their help with experiments during the passed five years. I would also like to thank all of the members of the faculty and staff of Department of MSE and nanoSTAR.

I would like to acknowledge Ryan B. Comes for the X-ray Photoemission Spectroscopy measurements performed Pacific Northwest National Laboratory and helpful discussion. The Rutherford backscattering measurement in this work was performed by collaborators Ryan B. Comes and Tamara F. Isaace-Smith at Auburn University and Nate Newman and Matthew Edwards at Arizona State University. I would like to express my thanks to their help on my research work.

Finally, and most importantly my thanks go to my beloved family, for their love and support throughout the path. Without their support and encouragement, I would not be

where I am today.

# Abstract

Metal-insulator transition (MIT) in $NbO_2$ has not been studied extensively since its discovery. The phase transition in $NbO_2$ can be triggered by different external excitations, and the transition temperature (1081 K) is much higher than those of other materials with MIT property, which promises extended temperature range in circuit applications. Despite of the potential applications, there was no significant advances in the research on MIT of $NbO_2$, both on understanding of underlying mechanisms and insights to the modulation of MIT, largely attributed to the difficulty in synthesizing phase pure $NbO_2$.

My dissertation has been focused on investigating the MIT on thin film $NbO_2$ synthesized by a reactive bias target ion beam deposition (RBTIBD) technique. Epitaxial phase pure $NbO_2$ films were grown on sapphire (0001) substrates, and effect of deposition conditions ($Ar/O_2$ mixture flow rate and substrate heating) on film quality was investigated. It was found that film quality was sensitive to the Nb/O stoichiometry that could be effectively tuned by the $Ar/O_2$ mixture flow rate, while being much less sensitive to substrate heating within the investigated range. Comprehensive structural and transport characterization was conducted on film deposited under optimized conditions. A thin layer (1-2 nm) of $Nb_2O_5$ was discovered at the surface due to spontaneous oxidation in the ambient environment. In addition, I investigated the cation substitution as a path to modify microstructures and transport properties of $NbO_2$ films. In particular, effect of V substitution was studied by depositing substitutionally alloyed $V_xNb_{1-x}O_2$ films considering similarities between $VO_2$ and $NbO_2$. Structural analysis suggested that the V substitution broke

the Nb-Nb dimers in tetragonal $NbO_2$ lattice. With the increase of V concentration, film lattice transited from distorted rutile structure to regular rutile structure.

The effect of applied electric field on the MIT of $NbO_2$ was studied on metal/$NbO_2$/TiN/Si structures. *In-situ* Nb capping was employed to prevent the formation of $Nb_2O_5$. Unipolar threshold switching characteristics was observed, with repeatability of several hundreds of cycles and thermal stability up to 150 °C. By comparing MIT characteristics of structures with and without $Nb_2O_5$, it was found that the presence of $Nb_2O_5$ resulted in a significantly larger threshold electric field ($\sim$ 250 kV/cm) for transition and more visible hysteresis. With *in-situ* Nb capping, the threshold electric field was 50-80 kV/cm. Band diagrams for both structures were proposed to explain the drastic differences. This new insight on the interfacial oxide can lead to very low power phase transition switches for electronic applications.

# List of Figures

# List of Tables

# Chapter 1

# Introduction

## 1.1 Motivation

Metal-insulator transition (MIT) exhibited by many transition metal oxides has been a long-standing interesting research topic in condensed matter materials science, with experimental and theoretical efforts to understand this phenomenon being ongoing for decades. Depending on the kind of material, underlying physical mechanisms that give rise to the MIT can be electron-electron interaction (Mott transition), electron-phonon interaction (Peierls transition) and disorder-induce localization (Anderson localization). [1] In recent years, thanks to the advances in oxide thin film growth techniques, there has been a growing emphasis on exploring device applications of this intriguing phenomenon. Materials with MIT property exhibit non-linear responses in physical, especially electrical properties to external stimuli (which can be thermal, electrical, optical, magnetic, strain, etc.) [2], thus have many potential applications such as ultrafast electrical switches [3], memristive devices [4], optical modulators [5], and thermal sensors [6].

To realize wide application of the MIT property, a big challenge yet to overcome is the low transition temperature of MIT ($T_{MIT}$). Figure 1.1 shows some selected oxides which exhibit temperature-driven MIT, and only a few of them show $T_{MIT}$ near or above room temperature. [2] Vanadium dioxide ($VO_2$) has attracted considerable research interest

during the past decades, due to its MIT that occurs near room temperature ($\sim$ 340 K), with abrupt and significant (several orders of magnitude across the transition) change in electrical conductivity and other physical properties. [7] However, the application of $VO_2$, especially as switching devices in circuits, is still limited by the low $T_{MIT}$. With such low $T_{MIT}$, undesirable switching is easily triggered by Joule heating, resulting in errors in circuit operation.

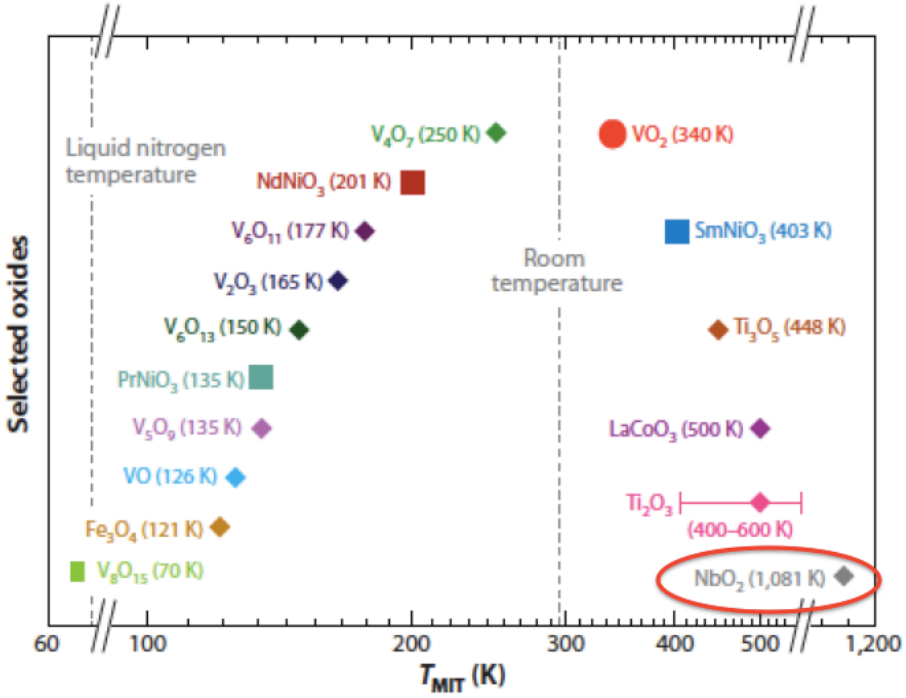


Figure 1.1: Transition temperature ($T_{MIT}$) of some selected oxides (bulk). [2]

Meanwhile, niobium dioxide ($NbO_2$), being a neighboring oxide, has received much less attention. The MIT in niobium oxides was discovered in as early as 1960s, which occurs at certain temperature [8, 9], electric bias [10], or optical excitation [11]. The transition properties of $NbO_2$ has much in common with that of $VO_2$, while the much higher $T_{MIT}$ ($\sim$ 1081 K) makes it less susceptible to Joule heating and therefore more appealing in circuit applications. However, after the MIT was first discovered in 1960s and studied

in bulk materials, there was a period when there were few studies on this material, largely due to challenges in synthesizing high quality $NbO_2$. In very recent years, thanks to the improvement in thin film synthesis techniques, a resurgence in the research on this material is taking place, with particular interest on the MIT under electric field. [12–15] This property promises potential applications such as selector devices in resistive random access memories (ReRAM), with the high $T_{MIT}$ of $NbO_2$ makes it more compelling in circuit application.

## 1.2 Objectives

Physical properties of $NbO_2$ films are sensitive to film quality in terms of phase purity, defects distribution, etc. Therefore the capability to control the quality of synthesized films is imperative to both understanding of underlying mechanisms and improvement of device performance. In this work, a unique reactive target bias ion beam deposition (RBTIBD) technique is employed to develop reproducible high quality $NbO_2$ thin films. Deposition condition variables, including $Ar/O_2$ flow rate, substrate heating, and vanadium substitution are studied to understand the effect on film properties.

$NbO_2$ has great potential in application mainly due to its MIT under electric field. Upon the success in synthesizing phase pure $NbO_2$ films, this property is investigated by fabricating vertical devices based on the deposited $NbO_2$ films and applying electric field through the devices. Electrical conduction and MIT mechanisms are explored, which will benefit further improvement of device performance.

## 1.3 Overview of dissertation

The work presented in this dissertation is the experimental study on MIT of $NbO_2$ thin films synthesized by RBTIBD technique. Dissertation is organized around three topics: epitaxial $NbO_2$ films, substitutionally alloyed $V_xNb_{1-x}O_2$ films and MIT under electric field.

Chapter 2 provides background information on structural and transport properties of $NbO_2$, and an introduction to MIT of this materials including phenomena and mechanisms.

Chapter 3 describes experimental techniques employed in this study, including the RBTIBD technique and the deposition procedures, as well as structural and transport characterization techniques.

Chapter 4 discusses experimental results on epitaxial $NbO_2$ films grown by RBTIBD technique. Effect of $Ar/O_2$ flow and substrate temperature on film properties is discussed. Structural and transport properties of the film deposited under optimized growth conditions are characterized.

Chapter 5 presents synthesis of substitutionally alloyed $V_xNb_{1-x}O_2$ films. Approaches of composition control using RBTIBD technique are explored. Effect of vanadium substitution on structural and transport properties is discussed.

Chapter 6 demonstrates MIT characteristics under electric field in metal/NbO2/TiN/Si structures. MIT in two type of structures are characterized, and respective band diagrams are proposed. Mechnism of MIT under electric field is briefly discussed.

Chapter 7 summarizes the key discoveries and observations, and discusses strategies for future development.

# Chapter 2

# Background

## 2.1 Structural properties

### 2.1.1 Crystal structure

$NbO_2$ adopts a rutile structure ($P4_2/mnm$) above 1081 K and a tetragonal structure ($I4_1/a$) at lower temperature. The lattice parameters of high temperature rutile $NbO_2$ are $a_R$ = 4.846 Å and $c_R$ = 3.032 Å. The low temperature tetragonal lattice can be viewed as a distorted rutile lattice containing 32 formulas per unit cell, with $a_T$ = 13.702 Å and $c_T$ = 5.985 Å. [16] The relations between the tetragonal unit cell and the rutile unit cell of $NbO_2$ can be represented by $a_T \cong 2\sqrt{2}a_R$, $c_T \cong 2c_R$, as is shown in Figure 2.1. [17, 18].

The structure of rutile $NbO_2$ can be understood as chains of edge-sharing (along $c$-axis) $NbO_6$ octahedra connected at corners, with regular Nb-Nb spacing along $c$-axis. Similarly, the structure of tetragonal $NbO_2$ can be interpreted as chains of distorted $NbO_6$ octahedra linked together. In tegragonal $NbO_2$, the displacement of Nb ions from the octahedra centers leads to a pairing of Nb ions along $c$-axis with the Nb-Nb distances being alternately 2.71 Å and 3.30 Å, as well as a zigzag displacement along the rutile [110] or [1$\bar{1}$0] directions with variation of Nb-O distances between 1.91 Å and 2.25 Å. [16, 19, 20]

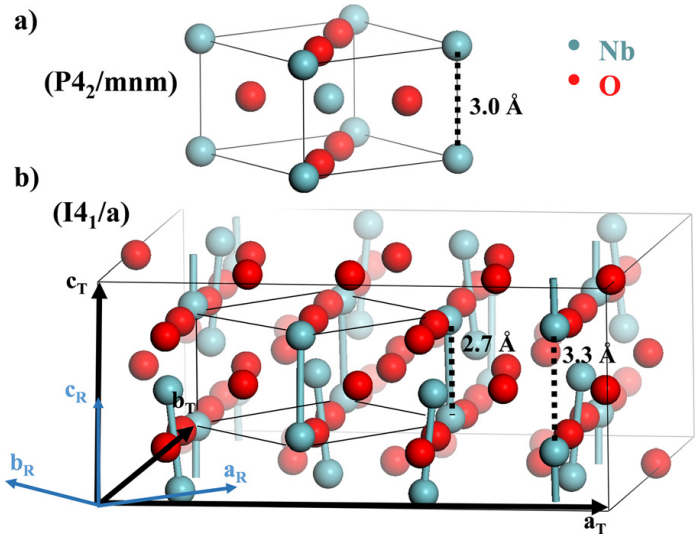


Figure 2.1: (a) Unit cell of the high temperature phase of $NbO_2$ with rutile crystal structure; (b) Unit cell of the low temperature phase of $NbO_2$ containing 32 formula unites of $NbO_2$. [17]

### 2.1.2 Synthesis of $NbO_2$ thin films

Despite the attractive attributes of $NbO_2$, experimental studies on this material, especially on thin films, has remained limited due to the challenges in synthesis. The Nb-O system is a complicated system, in which niobium can exist in four charge states: 0 in Nb, $2^+$ in NbO, $4^+$ in $NbO_2$, and $5^+$ in $Nb_2O_5$. In the phase diagram by Elliot which is shown by Figure 2.2 [21], it is shown that these oxide phases only exist within narrow single-phase fields with negligible deviation from exact stoichiometry. Besides these stable oxides of niobium, there are also metastable oxides $NbO_x$ within $0 < x < 1$ and $2.4 < x < 2.5$. [22] Moreover, the complexity of the Nb-O system is also exhibited by the existence of polymorphs of some oxide states, especially $Nb_2O_5$, some of which have similar crystal structures. In the review work on niobium oxides and niobates systems, Nico [22] provided a list of reported niobium oxides with different polymorphs, with the respective crystal structural information, as shown in Table 2.1. Since $NbO_2$ is not the most stable

oxidation state of niobium and only exist in small range of stoichiometry, it is therefore technically difficult to prepare phase pure $NbO_2$ thin films.

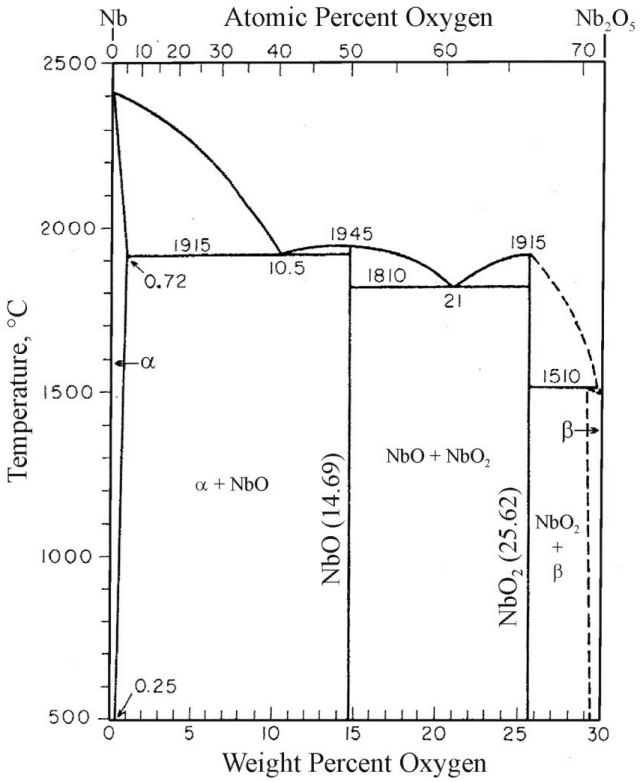


Figure 2.2: Niobium-oxygen phase diagram. [21]

| Phase | Crystal system | Lattice parameters | Space group |
|---|---|---|---|
| NbO | Cubic | $a$ = 4.210 Å | $O_h^1$ |
| $NbO_2$ | Tetragonal | $a$ = 13.696 Å | $C_{4h}^6$ |
| | | $c$ = 5.981 Å | |
| | Rutile | $a$ = 4.841 Å /$a$ = 4.55 Å | $D_{4h}^{14}$ |
| | | $c$ = 2.992 Å /$c$ = 2.86 Å | |
| | Monoclinic | $a$ = 12.03 Å | $C_{2h}$ |
| | | $b$ = 14.37 Å | |
| | | $c$ = 10.36 Å,β = 121.17 ° | |
| $Nb_{12}O_{29}$ | Monoclinic | $a$ = 15.686 Å | $C_{2h}^3$ |
| | | $b$ = 3.831 Å | |
| | | $c$ = 20.71 Å, β = 121.17 ° | |
| | Orthorhombic | $a$ = 3.832 Å | $D_{2h}^{17}$ |
| | | $b$ = 2.740 Å | |
| | | $c$ = 28.890 Å | |
| $Nb_{22}O_{54}$ | Monoclinic | $a$ = 15.749 Å | $C_{2h}^1$ |
| | | $b$ = 3.824 Å | |
| | | $c$ = 17.8521 Å, β = 102.03 ° | |
| T-$Nb_2O_5$ | Orthorhombic | $a$ = 6.175 Å | $D_{2h}^9$ |
| | | $b$ = 29.175 Å | |
| | | $c$ = 3.390 Å | |
| B-$Nb_2O_5$ | Monoclinic | $a$ = 12.73 Å | $C_{2h}^6$ |
| | | $b$ = 4.88 Å | |
| | | $c$ = 5.56 Å, β = 105.1 ° | |
| H-$Nb_2O_5$ | Monoclinic | $a$ = 21.153 Å/$a$ = 21.163 Å | $C_{2h}^1$ |
| | | $b$ = 3.8233 Å/$b$ = 3.824 Å | |
| | | $c$ = 19.356 Å/$c$ = 19.355 Å | |
| | | β = 119.80 ° | |
| N-$Nb_2O_5$ | Monoclinic | $a$ = 28.51 Å | $C_{2h}^3$ |
| | | $b$ = 3.830 Å | |
| | | $c$ = 17.48 Å,β = 120.8 ° | |
| Z-$Nb_2O_5$ | Monoclinic | $a$ = 5.219 Å | $C_2^1$ |
| | | $b$ = 4.699 Å | |
| | | $c$ = 5.928 Å,β = 108.56 ° | |
| R-$Nb_2O_5$ | Monoclinic | $a$ = 12.79 Å | $C_{2h}^3$ |
| | | $b$ = 3.826 Å | |
| | | $c$ = 3.983 Å, β = 90.75 ° | |
| M-$Nb_2O_5$ | Tetragonal | $a$ = 20.44 Å | $D_{4h}^{17}$ |
| | | $b$ = 3.832 Å | |
| P-$Nb_2O_5$ | Tetragonal | $a$ = 3.876 Å | $D_4^{10}$ |
| | | $b$ = 25.43 Å | |
| TT-$Nb_2O_5$ | Pseudohexagonal | $a$ = 3.607 Å/$a$ = 3.600 Å | $D_4^{10}$ |
| | | $c$ = 19.356 Å/$c$ = 19.355 Å | |
| | Monoclinic | $a$ = 7.23 Å | |
| | | $b$ = 15.7 Å | |
| | | $c$ = 7.18 Å, β = 119.08 ° | |

Table 2.1: Niobium oxides crystalline phases. [22]

After the early studies on bulk $NbO_2$ during 1960s and 1970s, experimental studies on $NbO_2$ has been slow for 20-30 years. In recent years, advances in oxide thin film synthesis techniques provide new opportunities to study and utilize $NbO_2$ thin films. The growth of crystalline $NbO_2$ thin films has been explored by techniques including reactive sputtering [18, 23, 24], molecular beam epitaxy (MBE) [25], chemical vapor transport method [26], thermally oxidization of Nb [27], etc. In particular, epitaxial thin films have been synthesized on $Al_2O_3$ (0001), MgO (111), $MgAl_2O_4$ (111) by reactive sputtering [18] and on $(La,Sr)_2(Al,Ta)_2O_6$ (LSAT) (111) and $SrTiO_3$ (STO) (111) by MBE [25]. However, highly pure $NbO_2$ thin films with good crystallinity remains challenging to synthesize, since it requires precise control of the amount of oxygen in a narrow window.

## 2.2 Transport properties

### 2.2.1 Band structure

Niobium atom has a $4d^4 5s^1$ electron configuration. Upon the formation of $NbO_2$, four electrons form bonds with O atoms, giving rise to a $4d^1$ system. The near-Fermi level energy band structure of $NbO_2$ is the result of hybridization of Nb 4*d* and O 2*p* orbitals stabilized by symmetry of crystalline field, which can be described based on the molecular orbital picture of $VO_2$ proposed by Goodenough. [20, 24, 28–31]

The hybridization between Nb 4*d* and O 2*p* orbitals leads to $\sigma$- and $\pi$-type overlap, with $e_g$ and $t_{2g}$ octahedral symmetry respectively due to the octahedral symmetry of $NbO_6$ octahedra. The bonding states are primarily of O 2*p* character and the antibonding states are dominated by Nb 4*d* orbitals, and stronger *p*-*d* overlap of the $\sigma$ bonding gives rise to larger splitting between $\sigma$ and $\sigma^*$. In addition, since the $NbO_6$ octahedra also share edges along *c*-axis, the orthorhombic component of the crystalline field further degenerates the

antibonding π bands into $d_{\|}$ band and $e_g^{\pi}$ band, in which the $d_{\|}$ band also involves in σ-type *d*-*d* overlap along *c*-axis.

As is illustrated by Figure 2.3 (a), in $NbO_2$ phase with regular rutile lattice, $d_{\|}$ band overlaps with $e_g^{\pi}$ band, with Fermi level lying in the middle. Therefore the two bands are partially filled, giving rise to the metallic state. In tetraganol $NbO_2$ phase, the $d_{\|}$ band is split into the bonding band $d_{\|}$ which lies below $E_F$ and the antibonding band $d_{\|}^*$ which lies above $E_F$. The $e_g^{\pi}$ band that locates between the $d_{\|}$ band and $d_{\|}^*$ band is lifted above the $E_F$ and depopulated, giving rise to a small band gap (Figure 2.3 (b)).

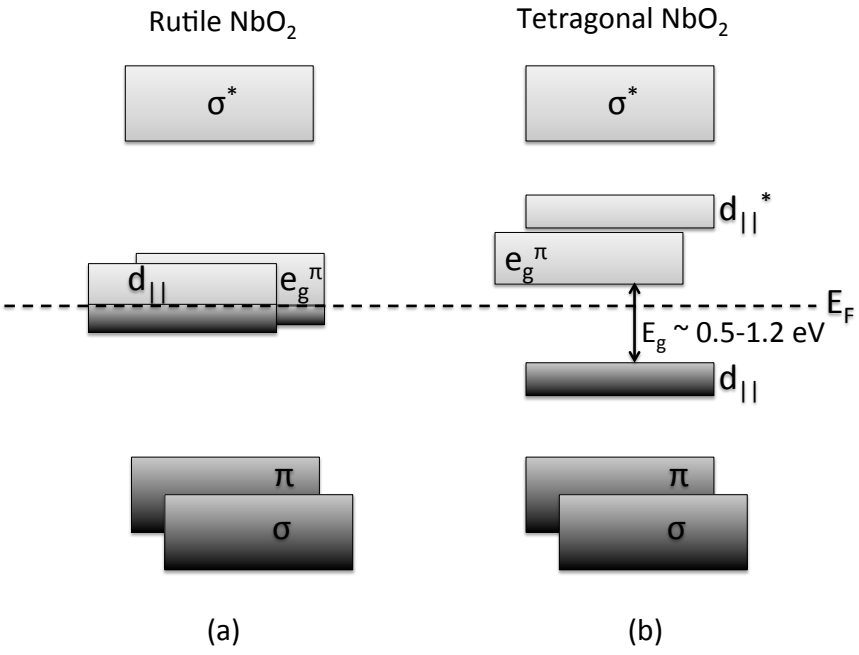


Figure 2.3: Band structure diagrams of $NbO_2$ near Fermi Level in (a) rutile and (b) tetragonal phases. [20, 24, 28–31]

Regarding the size of band gap, there is a wide range of values reported in experimental studies. The experimentally determined $E_g$ ranges from $\sim$ 0.5 eV to $\sim$ 1.2 eV,

with the variance being related to the difference in sample quality and measurement techniques. [9, 32–35] Recently, in an attempt to put an end to the inconsistency of $NbO_2$ band gap, theoretical calculation using the local density approximation (LDA) method with a Hubbard $U$ correction gave an indirect band gap of 1.15 eV, and experimental studies on epitaxial $NbO_2$ thin films reported an indirect band gap of $\sim$ 1 eV. [25, 36]

### 2.2.2 Extrinsic conduction mechanisms

The electronic structure of a $NbO_2$ sample, which determines its electrical transport properties, is defined by the band structure of crystalline $NbO_2$ as well as prevalent defect states especially in deposited films. Therefore, besides the intrinsic band conduction, some extrinsic electrical transport mechanisms also need to be considered in appropriate temperature ranges. [37]

#### 2.2.2.1 Small polaron hopping

Due to the electron-phonon interaction, charge carrier can minimize its free energy by spatially localizing and becoming trapped by the potential well created by displacing the ions around it. The formation of a small polaron is favorable when the lowering of energy due to trapping of the carrier is large compared to the energy penalty caused by displacing the ions around it, which is easily satisfied in materials with narrow condition band and strong electron-phonon interaction. [38–40]

The motion of localized polarons can be realized through hopping, which is assisted by thermally activated phonons. Therefore the hopping rate has an Arrhenius temperature dependence with an activation energy.

$$\mu_{SPH}(T) = \mu_{0,SPH}(T) exp(-\frac{W}{k_B T}) \tag{2.1}$$

in which $\mu_{0,SPH}(T) \propto 1/T^{3/2}$ and $W \cong \frac{1}{2}W_p$ for non-adiabatic limit wherein hopping is much slower that lattice vibration; $\mu_{0,SPH}(T) \propto 1/T$ and $W \cong (\frac{1}{2}W_p - t)$ for adiabatic limit wherein carriers hop to response lattice vibration immediately. $W_P$ is the carrier energy change upon polaron formation and $t$ is a measure of the amount of orbital overlap to characterize the strength of interaction between hopping sites. [37, 38, 41]

Besides the energy barrier for hopping, another activation term associated with the carrier generation also contribute to the Arrhenius temperature dependence of conductivity. [38, 41, 42]

#### 2.2.2.2 Hopping via (localized) defect states

Due to the prevalence of imperfections in deposited films, charge carriers hopping between localized defect states can make significant contribution to the electrical transport at relatively low temperatures or when the density of defects is high. The problem was first treated by the random resistance network suggested by Miller and Abrahams. [43]

• In non-crystalline semiconductors, while the basic electronic structure can be maintained by the short-range order of lattice, the lack of long-range order results in localized states. According to the framework of strong localization developed by Anderson and Mott, the localized states exist beyond the non-localized states as broad tails extending into the band gap, separated by energy levels called "mobility edge" ($E_C$ or $E_V$, as is shown in Figure 2.4). [44, 45]

It has been shown that for polycrystalline samples, the defects at grain boundaries can also lead to static energetic disorder, resulting in localized band-tail states. Electrical transport can be conducted by carriers excited into band-tail states and hop between the localized states. The conductivity can be expressed as

$$\sigma(T) = \sigma_0 \cdot exp(-\frac{W}{k_B T}), \quad W = (E_A - E_F) + w \ \ or \ \ (E_F - E_B) + w \tag{2.2}$$

where $E_A - E_F$ (or $(E_F - E_B)$) is the carrier excitation energy and $w$ is the activation energy of hopping which decreases with the decrease of temperature, taking into account the variable range nature of hopping. [42]

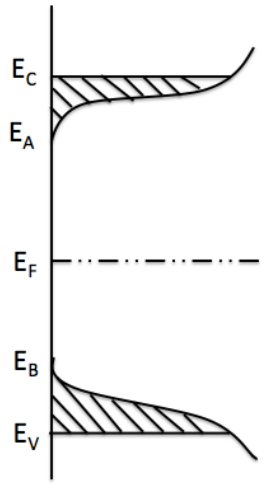


Figure 2.4: Schematic band structure showing localized states (shaded) and mobility edges. [42]

• When the density of states (DOS) of defect states has a maximum at $E_0$ and the DOS near Fermi level $E_F$ is small, carriers hop the closet distance possible to the nearest neighbor sites. This case is termed as the nearest neighbor hopping (NNH), and the conductivity is expressed as

$$\sigma_{NNH}(T) = \sigma_{0,NNH} \cdot exp(-\frac{W_{NNH}}{k_B T}), \quad W_{NNH} = \mid E_0 - E_F \mid \tag{2.3}$$

• At reduced temperature, conduction can be dominated by states in the vicinity of $E_F$, the DOS of which is much smaller. The average hopping distance will be much larger than the distance between nearest neighbors and dependent on temperature (hence termed as "variable range hopping (VRH)"). For the model propose by Mott, the DOS near Fermi

level $N(E_F)$ is treated as a finite constant. The conductivity is given by

$$\sigma_{Mott}(T) = \sigma_{0,Mott} \cdot exp(-\frac{T_{Mott}}{T})^{1/(d+1)} \tag{2.4}$$

in which $d$ is the spatial dimensionality. [42]

• For Mott's VRH model, the DOS near Fermi level ($N(E_F)$) is treated as a constant on the assumption that the Coulomb interaction between hopping sites is neglected. With this interaction being taken into account, carriers on states near $E_F$ will be redistributed to reduce the total energy. This leads to a "Coulomb gap" at $E_F$, with $N(E_F)$=0. Assuming the DOS near $E_F$ can be described by $N(E) = c \mid E - E_F \mid^n$ ($c$ is a constant), instead of Eq. 2.6 the following expression holds [39, 46, 47]

$$\sigma(T) = \sigma_0 \cdot exp(-\frac{T_0}{T})^{(n+1)/(n+4)} \tag{2.5}$$

The case where $n$=2 is often observed, which is known as Efros-Shklovskii VRH. The conduction can be described as [48]

$$\sigma_{ES}(T) = \sigma_{0,ES} \cdot exp(-\frac{T_{ES}}{T})^{1/2} \tag{2.6}$$

#### 2.2.2.3 Zabrodskii - Zinov'eva method

As introduced above, different conduction processes can be expected in appropriate temperature ranges. The dependence of conductivity on temperature, or more specifically, the exponential dependence of $ln(\sigma)$ on $(1/T)$, is a useful indication of the conduction mechanism. Considering the situation observed frequently that the $\sigma$ vs. $T$ data can be fitted by different conduction models fairly well, a procedure developed by Zabrodskii and Zinov'eva [49] is often employed to analyze the $\sigma$ vs. $T$ data. A general expression is used

to describe the conduction process

$$\sigma(T) = \sigma_0 T^{-m} exp(-\frac{W}{T^p}) \tag{2.7}$$

and a parameter *M(T)* is defined as

$$M(T) = \frac{\partial ln[\sigma(T)]}{\partial ln(T)} = \frac{pW}{T^p} - m \tag{2.8}$$

Assuming that $m$ is much smaller than the first term of *M(T)*, then $M(T) \cong pW/T^p$. Therefore $ln[M(T)] = ln(pW) - pln(T)$, and the value of $p$ can be determined from the slope of *ln[M(T)]* vs. *ln(T)* plot.

#### 2.2.2.4 Temperature dependence of Seebeck coefficient

Seebeck coefficient $S$ is measured by $\Delta V/\Delta T$, where $\Delta V$ is the voltage difference between two points on a sample with a temperature difference $\Delta T$. A general expression of $S$ is given by [50]

$$S = -\frac{k_B}{e}\int(\frac{E-E_F}{k_B T})\frac{\sigma(E)}{\sigma}dE \tag{2.9}$$

For an $n$-type semiconductor, the expression of $S$ can be reduced into

$$S(T) = -\frac{k_B}{e}(\frac{E}{k_B T} + A) \tag{2.10}$$

The activation energy $E$ is determined by $(E_C - E_F)$ for crystalline semiconductor or when the conduction is conducted by non-localized electrons beyond the mobility edge, by $(E_A - E_F)$when conduction is carried among localized states in band tails, and by carrier generation energy for small polaron hopping. [42]

Therefore the Seebeck coefficient measurement provides a method to decouple carrier

concentration $n$ and mobility $\mu$ from measured conductivity and to determine wether an activation energy term exists in the carrier mobility. [37, 42]

For another case where conduction is carried by VRH among states near Fermi level, it was proposed that $S$ increases as $T^{1/2}$ for slowly varying DOS near $E_F$. [42, 51, 52] The opposite trend of temperature dependence can be employed to identify the existence of VRH among defect states near $E_F$.

### 2.2.3 Reported electrical transport properties

Below transition temperature ($T_{MIT}$), the distorted rutile phase of $NbO_2$ exhibits semiconducting behavior. The conductivity at room temperature is on the order of $\sim 10^{-4}\ \Omega^{-1}\cdot cm^{-1}$, and gradually increases with temperature until $\sim 10^{3}\ \Omega^{-1}\cdot cm^{-1}$ near $T_{MIT}$. [9, 53] Some early studies on bulk $NbO_2$ demonstrated that a departure from stoichiometric composition would sharply increase the conductivity [53–55], and a recent study on $NbO_2$ thin films also suggested similar trends [56].

It was proposed that under relatively low temperature (200 K - 450 K), the electrical transport of $NbO_2$ was conducted by thermally activated hopping of small polarons, and the activation energy obtained from fitting the conductivity data was $\sim$ 0.4 eV. [57, 58] With the increase of temperature, the intrinsic band conduction became dominating, with the activation energy decreased from $\sim$ (0.5-0.6) eV to zero as the temperature approached $T_{MIT}$. [35, 57] A progressive delocalization of electrons (from $\sim$ 600 K to $T_{MIT}$) was pointed out by Gervais through infrared reflectivity measurements. [59]

Moreover, studies on bulk single crystal $NbO_2$ samples demonstrated anisotropy in transport properties. Along the direction of $c$-axis, $NbO_2$ samples exhibit higher conductivity with lower activation energy, larger high-frequency dielectric constant and weaker electrons localization than along directions perpendicular to $c$-axis. [57, 59] Resistivity vs.

temperature results by B*é*lange et al. also suggested that the $NbO_2$ single crystal samples were semiconductor-like along *a*-axis and only metallic-like along *c*-axis, and the measurements on polycrystalline $NbO_2$ revealed the average properties. [57]

$NbO_2$ exhibits a negative Seebeck coefficient, indicating a *n*-type semiconductor. The magnitude of Seebeck coefficient is on the order of $\sim 10^3$ $\mu$V/K at room temperature and decreases to $\sim 10^2$ $\mu$V/K around 1000 K. [9, 57, 60]

All properties summarized above were obtained from bulk $NbO_2$ samples, and transport characterization on $NbO_2$ thin films is still very limited. Only recent study on epitaxial $NbO_2$ thin films on sapphire substrates by Wong et al. showed an activation energy for conduction of $\sim$ 0.16 eV between 300 K and 400 K. [24]

## 2.3 Metal insulator transition (MIT)

### 2.3.1 MIT properties

The conductivity of $NbO_2$ increases gradually with temperature until $\sim$1081 K, where the MIT of $NbO_2$ takes place with a $\sim$ 10 times increase in conductivity. Anomaly in other physical properties, including magnetic susceptibility and Seebeck coefficient has also been observed in bulk $NbO_2$. [8, 9, 57] The MIT around 1081 K is also accompanied by a transition in crystal structure, from the distorted rutile lattice to the regular rutile lattice. [61, 62]

Besides when being heated to the transition temperature ($\sim$ 1081 K), $NbO_2$ also exhibits transition in resistivity under electric field, which was first reported in 1960s. [10, 63] The reversible transition of resistivity under electric field demonstrates threshold switching (TS) characteristics, for which only high resistivity state is stable under low electric bias, while the low resistivity state collapses when the applied bias is reduced below certain

value. [64, 65] The I-V curves of $NbO_2$ under electric field exhibited unipolar characteristics. Recent studies on this property of $NbO_2$ thin films demonstrated reproducibility for 1000 cycles, thermal stability up to 160 °C, and switching speed $\sim$ 22 ns. [23] However, the nature of this transition in resistivity remains controversial, regarding wether it is thermally driven with the thermal power coming from Joule heating [66] or electronically triggered by certain threshold carrier concentration [67] or threshold electric field [13].

### 2.3.2 Mechanism of MIT

The simple one electron theory which describes the band structures and transport properties of materials is based on the assumption that electrons move freely in a periodic potential imposed by the ions and other electrons in the crystal. The periodicity of the potential results in the electron energy band gaps, and the situation of electrons filling the energy bands determines the solids to be metallic, semiconducting or insulating. However, for materials in which electrons have strong interaction with lattice, electrons, or local disorder that cannot be neglected or treated as perturbation, this model will fail in providing explanation for the transport phenomena. This situation happens to some transition metal oxides including $NbO_2$, therefore models with these interactions accounted are needed to explain the observed transport properties. [68]

#### 2.3.2.1 Peierls transition

A Peierls transition is a MIT induced by electron-phonon (electron-lattice) interaction. Figure 2.5 (a) shows a chain of $N$ equally spaced atoms with the period of $a$. Starting from the simplest model of 1-D lattice:

$$H = H^0 + V = \frac{p^2}{2m} + V(x) \tag{2.11}$$

in which $H^0$ is for the non-interacting electrons in the chain, and $V(x) = V(x+a)$ is the periodic potential of the chain of ions. By applying the perturbation theory, the periodicity of the potential results in the discontinuity of energy dispersion curves at the Brillouin zone boundaries and forms the band gaps. Accounting for the two spin states that each $k$ state can hold, each band can hold $2N$ electrons. For solids with only one electron per atom, the band will be half-filled and therefore the solid will be metallic. When the atoms in the chain are rearranged slightly, in a way that the spacing between the closest atoms alternates which is called dimerization, the periodicity of the crystal becomes $2a$. As is shown in Figure 2.5 (b), a new band gap will be formed at $k_F = \pi/2a$. For a solid with one electron per atom, the lowest band will be completely filled at ground state, leaving the upper band unfilled and giving rise to the insulating state. In this process, the electron energy reduction with the increase of atomic displacement $\delta$ is proportional to $\delta$, while the crystal elastic energy increase due to the distortion is proportional to $\delta^2$. As long as $\delta$ is below certain value, the distorted structure and insulating state is energetically preferred. Therefore it was predicted by R. Peierls that one dimensional (1-D) metal would not exist at 0 K. [69]

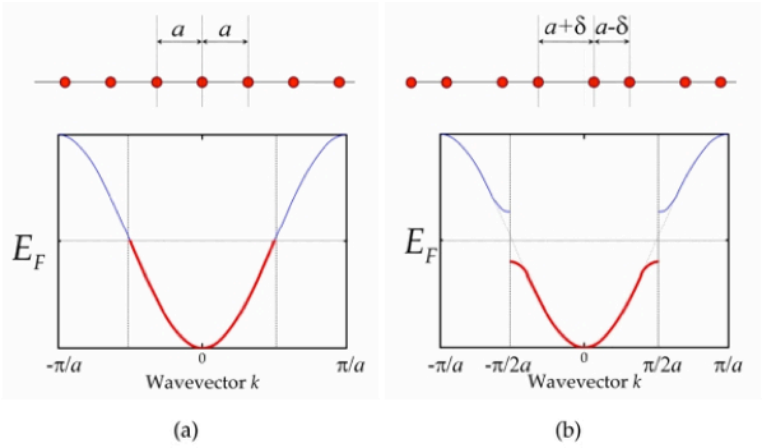


Figure 2.5: The atomic configuration and band structures of (a) a 1-D normal metal and (b) a Peierls insulator. [70]

At elevated temperature, the electron energy reduction decreases due to the Fermi distribution, therefore above certain temperature the undistorted structure is favored and the Peierls transition takes place.

Based on the description above, it can be deduced that for a Peierls transition to happen, the solid needs to be 1-D and has half-filled conduction band. The 1-D conduction structure can exist in 3-D crystals with certain atom chains along one direction being responsible for the electrical conduction.

#### 2.3.2.2 Mott transition

The theory of Mott transition was proposed to interpret the transition originated from the electron-electron interaction. [71–73] In solids that exhibit Mott transition, the Coulomb interaction between electrons, which is called "electron correlation", is so strong that cannot be neglected.

The Mott insulating state was first found in some transitional metal oxides despite that there were odd number of electrons per lattice site, which was not explicable based on the simple band theory. It can be understood from a tight-binding model, with $N$ primitive unit cells and one electron each site. If the Coulomb repulsion $U$ between electrons is negligible, $2N$ states can be held by the band accounting for the spin degeneracy, therefore the band is half-filled and solid is metallic. When there is strong electron correlation, a second electron that tries to sit in one site will feel strong Coulomb repulsion $U$ from the electron that already sit in that site. As is shown in Figure 2.6, if the repulsion $U$ is larger than the bandwidth $W$, it will split the half-filled band into a lower band (Lower Hubbard Band, LHB) fully filled by electrons taking an empty lattice site and an empty higher band (Upper Hubbard Band, UHB) for electrons trying to occupy a site that is already taken by an electron.

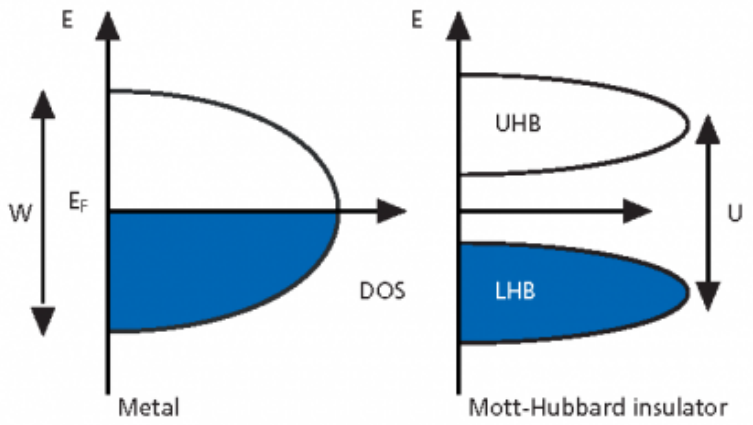


Figure 2.6: Band diagram illustrating the Mott transition. [74]

According to this model, the MIT due to electron-electron interaction can be discussed in two situations. When the band is half-filling, the decrease of Coulomb repulsion $U$ relative to the bandwidth $W$ will reduce the band gap between the LHB and UHB and eventually result in the MIT. As an example, in real materials the change of bandwidth can be induced by the change in atomic spacing. In the other situation, the MIT can be induced by the change in band-filling, realized by doping the UHB/LHB with electrons/holes. According to the experimental observation, there is a critical free carrier density required to induce the MIT. Based on the consideration that free electrons can screen the Coulomb potential from ions, Mott proposed the criterion for the MIT to occur:

$$n_c^{1/3} a_H \sim 0.2 \tag{2.12}$$

where $n_c$ is the critical carrier density for MIT to happen at T = 0 K, and $a_H$ is the effective Bohr radius of electrons. [73]

#### 2.3.2.3 Mechanisms of MIT in $NbO_2$

From the point view of band structure, two changes in band structure are required for the MIT in $NbO_2$ to happen: 1) an upshift of the $e_g^\pi$ band above $E_f$, leaving the $d_\parallel$ band half-filled, and 2) a split of the $d_\parallel$ band.

Currently, studies on MIT of $NbO_2$ remain limited. However, MIT of $NbO_2$ can be understood based on the intense studies on $VO_2$, a $3d^1$ system that also exhibits MIT accompanied by similar structural transition. The upshift of the $e_g^\pi$ band is due to the increased *p-d* overlap between Nb and O, caused by the reduced Nb-O spacing resulted from the zigzag-like displacement of Nb atoms. The upshift causes the depopulation of the $e_g^\pi$ band, leaving it empty and lying above $E_F$.

Dispute centers on the mechanism of $d_\parallel$ splitting, whether it is due to the metal dimerization or increased electron correlation. In Goodenough's model, the metal-metal paring parallel to *c*-axis leads to the splitting of $d_\parallel$ into filled bonding and empty antibonding bands. However, in his paper Goodenough also questioned the metal dimerization as the major driving force of the MIT. Instead, he proposed that the MIT was resulted mainly from the increased *p-d* overlap due to the antiferroelectric distortion of $VO_6$ octahedra (the anitparallel cation displacement toward the octahedral edge). The $d_\parallel$ splitting could also results from this distortion, due to the change of symmetry. [28] Another model proposed by Zylbersztejn and Mott attributed the MIT to electron-electron correlations in $d_\parallel$ band. In metallic phase, the correlation is significantly screened by the $e_g^\pi$ band overlaping with $d_\parallel$. Once the $e_g^\pi$ is upshifted due to the increased *p-d* overlap resulted from the antiferroelectric displacement of V atoms, the increased electron correlation will lead to the MIT. [75]

The MIT of $NbO_2$ happens at a much higher temperature ($\sim$ 1081 K) than $VO_2$ ($\sim$ 340 K) does. Since the $4d$ orbitals of $NbO_2$ are more dispersed in terms of energy and space that the $3d$ ones of $VO_2$, electron correlation effect should be less important in $NbO_2$ than

in $VO_2$. On the other hand, the broader $4d$ band of $NbO_2$ gives rise to stronger metal-metal bonding and therefore should contribute more to the much higher transition temperature of $NbO_2$, which was supported by the calculation by V. Eyert. [20, 76] Also very recently, calculation by Andrew O'Hara suggested that the transition was driven by Pererils type structural transition via dimerization of Nb atoms. [77]

# Chapter 3

# Experimental

## 3.1 Film growth

### 3.1.1 Reactive bias target ion beam deposition (RBTIBD)

Reactive bias target ion beam deposition (RBTIBD) combines the features of ion beam deposition (IBD) and sputtering, to address the limitation of conventional IBD in the preparation of clean interfaces in multilayer structures. [78–80] The system used in this study is the LANS model manufactured by 4Wave, Inc., the schematic of growth chamber of which is illustrated in Figure 3.1. As is shown in the figure, six metallic targets sit in a square geometry, in line with an ion source and a vertically positioned, 100 mm sample stage.

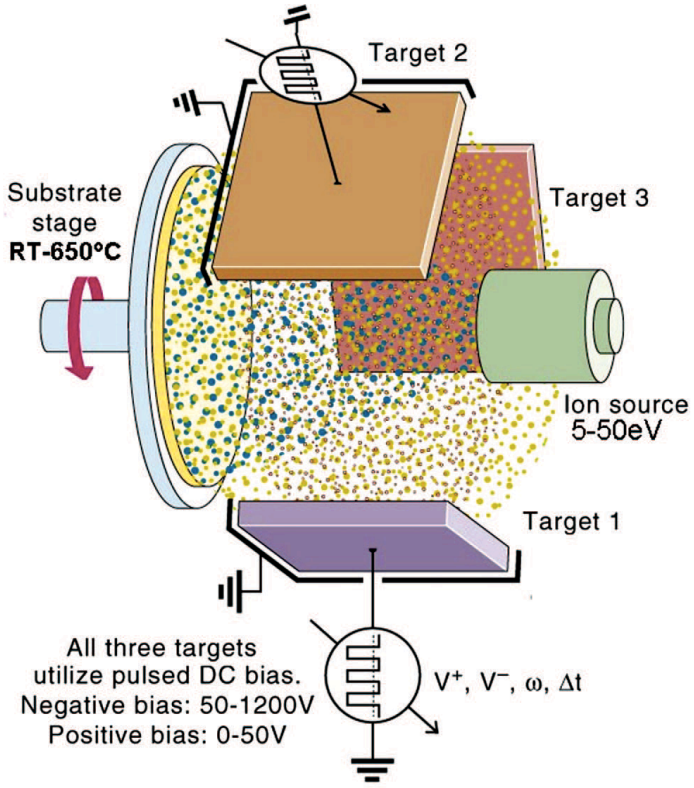


Figure 3.1: Schematic diagram of RBTIBD growth chamber.

RBTIBD utilizes a novel low energy ion source that combines a hollow cathode electron source (HCES) [81] and a Mark II end-Hall ion source [82] as anode, to provide a high density ion gas with low energy. [83] Electrons are emitted from HCES and flow towards anode, passing through a magnetic field. The interaction of electrons with magnetic field near the anode causes ionization of the inert gas. The HCES and anode ion source are each powered by a 0-100 V and 0-12 A supply, which can produce a flux of low energy (5-50 eV) ionized inert gas. The energy of ionized gas is not enough to cause any sputtering of targets or construction material inside the chamber. Three gas lines are fed into the chamber: two Ar gas lines, one connected to the HCES and the other connected to the anode; the third one is to supply reactive gas ($Ar/O_2$ 80/20 mixture in this study) through the anode. All gas used in this study is of ultra high purity (UHP) with 99.999% purity. The gas flow

rates of the three lines are each controlled by a digital mass flow controller (MFC), and the allowed flow rate ranges for the HCES Ar, anode Ar and reactive gas are 0-20 SCCM, 0-100 SCCM, 0-20 SCCM, respectively.

There are six metallic targets (diameter = 100 mm) installed in the system. The targets are made of 99.99% pure metals and are water-cooled during deposition through copper backing plates. A two-stage Y-shaped target shutter simultaneously shields three targets, while exposing the other three. This design allows co-sputtering of as many as three targets at one time. The targets are positioned in the way that they are parallel to the flux of ionized gas.

The targets are pulsed DC biased, in the way that targets are powered alternately by a large negative bias with a range of 2 kV/1 A and a small positive bias with a range of 60 V/ 5 A at a controlled frequency and pulse period. The pulse is controlled by a frequency generator with a frequency range of 1-75 kHz and the period is determined by 1/f. There are three frequency generators, each connecting to two targets, one of which is covered by the target shutter. Therefore one to three targets can be simultaneously powered at separated frequencies and pulse periods, allowing control of the composition during co-sputtering.

Sputtering of the target material occurs during the negative bias period. The large potential difference between the negatively charged target surface and the positively charged ion gas accelerates the ions towards the target surface at a nearly normal incidence angle, creating a thin plasma sheath ($\sim$ 2 mm) and inducing sputtering of the target material. The impact energy of ions onto target surface depends on the negative bias applied to the target, ranging from 50 eV to 2 keV. Since the thickness of plasma sheath ($\sim$ 2 mm) is much smaller than the distance between the ion source and target ($\sim$ 16 cm), the large negative bias has little effect on the ion trajectories from ion source to targets. The little part of ions that miss the targets and strike towards other hardware surfaces will have an un-accelerated low energy, which is below the threshold value to cause any sputtering of

construction material. While the Ar gas does not react with the target material, $O_2$ in the reactive gas mixture does chemically bond to the target material. Over time ($\sim$ few seconds) this will cause an insulating dielectric layer buildup at the target surface. This will lead to target poisoning, which will drastically reduce the sputtering yield. The small positive bias is designed to remove the dielectric buildup at target surface by repulsive potential force.

The sample stage, which is vertically positioned and aligned in line with the ion source, is kept rotating during deposition for the uniformity of deposited films. The substrate carrier is made from Tantalum (Ta), which has a high melting point (3290 K), low thermal expansion coefficient (6.3 $\mu$m/(m·K) at 25 °C), and non-ferrous nature. The stage is 3 mm thick and has a 4 inch diameter, and Ta clamps and Ti screws are used to mount substrates onto the stage.

Heating to the stage is supplied by an infrared heating lamp immediately behind the stage. The thermal output of the lamp is controlled by a variable voltage input, which is realized by a digital to analog convertor (DAC). The DAC value ranges from 0 to 35000, corresponding to the stage surface temperature from $\sim$75 °C to $\sim$650 °C. Using a standard *k*-type thermometer, the actual surface temperature of the stage can be directly measured. The relationship between the measured stage surface temperature and DAC values is calibrated prior to the deposition of a sample set, an example of which is shown in Figure 3.2.

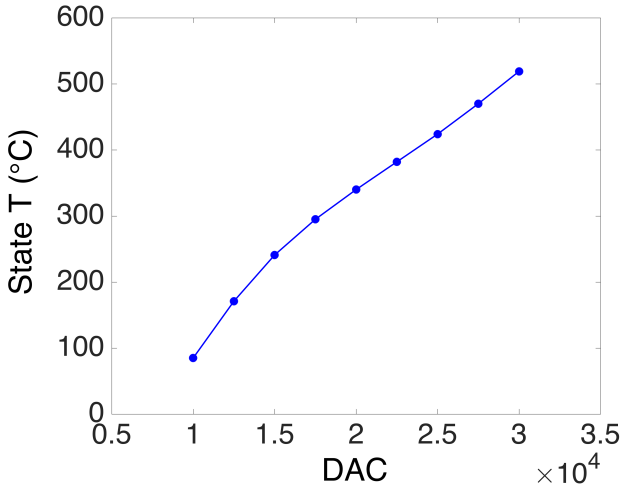


Figure 3.2: An example of DAC calibration for stage heater.

The base pressure of the main processing chamber is kept $\sim 10^{-8}$ Torr, obtained using a cryogenic pump. A load-lock mechanism is employed to load and remove samples without breaking the high vacuum in the main chamber. A mechanical rough pump is used to pump down the load lock chamber to 70-90 mTorr, every time before opening the high vacuum gate valve.

### 3.1.2 Deposition procedures

After loading substrates though the load lock, the main processing chamber needs to be pumped down below $9 \times 10^{-8}$ Torr before the deposition can be started. The HECS is first purged with 10 SCCM Ar gas for 30 minutes. This is followed by a degas procedure in which the tungsten filament inside the HECS is heated up for 30 minutes, to outgas any contamination on the surface. At the same time the degas starts, the stage heater is also ramped up to the desired DAC value (corresponding to the needed growth temperature) at a rate of 1000 DAC/min ($\sim$ 20 °C/min) according to the calibrated relation between

DAC value and measured stage surface temperature. It takes about 45 minutes for the temperature at the stage surface to stabilize. After the degas process, the ion source is turned on. Ar gas supply through the anode ion source is set to be 70 SCCM. The ion source is stabilized within 5 minutes. The stage is then set to start rotating at a speed of 10 rpm and the stage shutter is opened to allow the Ar ions to clean the substrate wafers for 3 minutes.

After pre-cleaning of substrates, the sputtering is then initiated by turning on the pulse generator and applying the DC voltage bias to needed targets. The negative bias applied to targets is -900 V and the positive bias is +20 V. After sputtering is induced, flow rate of the reactive gas mixture $Ar/O_2$ 80/20 is set to the desired value (2-8 SCCM). Before the real deposition taking place, 15 minutes is allowed for the conditions in the chamber to stabilize. A residual gas analyzer (RGA) is used to monitor the partial pressure of different gas species, especially $O_2$ in this study. The deposition cannot start until the partial pressure of $O_2$ observed by RGA is stable. The process pressure in chamber during deposition is $\sim$ 1 mTorr.

The deposition starts when the stage shutter, which is $\sim$2 mm above the stage, is opened and the substrate wafers are exposed to the ions in chamber. After the desired deposition time, the stage shutter is closed. For the growth of $NbO_2$, the reactive gas flow is then turned off to prevent further oxidation of the film. After that, the system is shut down in the following sequence: stage rotation, target bias, pulse frequency generator, HCES and anode power. The DAC value is set down to zero at a rate of 1000 DAC/min. At the same time, the Ar gas flow of 20 SCCM for HCES and 50 SCCM for anode are left on for 15 minutes and then only 20 SCCM for HCES with degas on for another 30 minutes. This is to prevent any material from re-depositing onto the HCES and anode part and cause contamination, resulting in the difficulty to start the ion source for next deposition. The stage needs to cool down for another $\sim$ 60 minutes to the ambient temperature before the

load lock can be retracted and the sample can be removed.

## 3.2 Structural characterization

### 3.2.1 X-Ray diffraction (XRD)

X-ray diffraction (XRD) is a powerful technique that is commonly used for crystal structural characterization, due to the wavelength of X-ray that is close to the atomic distances in materials and non-destructive nature of the measurements.

The principle of XRD can be briefly described as follows. [84] The incident X-ray is mainly scattered by electrons surrounding atoms in the sample, the intensity of which carries the same periodicity as the atomic structure. The intensity of diffracted X-ray has a strong angular dependence, which is described by the Bragg's law

$$\Delta\vec{k} = \vec{k_{in}} - \vec{k_{out}} = \vec{G_{hkl}} \tag{3.1}$$

in which $\vec{k_{in}}$ and $\vec{k_{out}}$ are wave vectors of the incident and diffracted X-ray beam, and $\vec{G_{hkl}}$ is the reciprocal lattice vector of the sample (Figure 3.3 (a)). In the direction that satisfies the Bragg's law, the intensity of the diffracted X-ray reaches a maximum and a peak will form in the XRD pattern.

By doing some transformation, the Bragg's law can also be illustrated in the real space, which is formulated as

$$2d_{hkl}\sin\theta = n\lambda \tag{3.2}$$

in which $d_{hkl}$ is the planer distance of the sample along certain direction, $\theta$ is the incident angle of X-ray with respect to sample surface, $n$ is certain integer and $\lambda$ is the wavelength of X-ray employed in the measurement. As is shown in Figure 3.3 (b), it can be understood

as that the incident X-ray is reflected by atoms in parallel planes and the reflected X-ray beam interferes with each other. Along directions in which the path difference of X-ray beam reflected by different planes is an integer number times of X-ray wavelength, the X-ray beam will interfere constructively and a peak will be created in the XRD pattern.

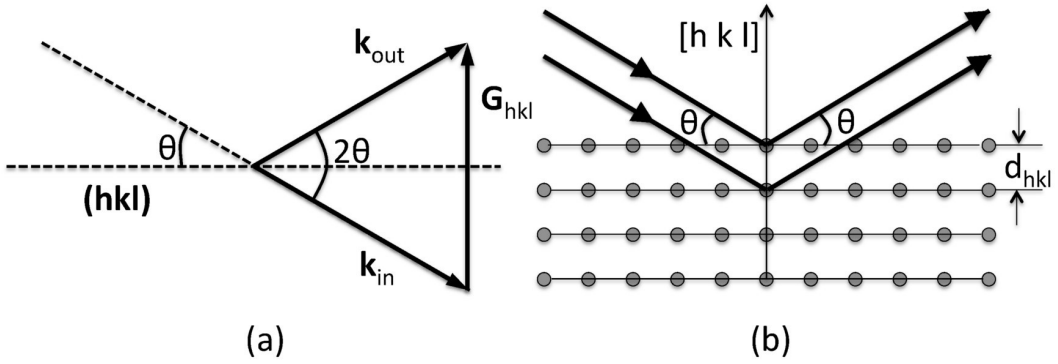


Figure 3.3: Geometry of the Bragg's law in (a) reciprocal space and (b) real space.

XRD scans in this study were performed using a SmartLab XRD system from Rigaku Inc., with a Cu Kα radiation ($\lambda$ = 1.54 $\AA$). Parallel beam option was employed, and a 2-bounce Ge(220)$\times$2 monochromator was used to provide X-ray beam with high monochromaticity. The attachment on which the sample stage is mounted has 3 axis to adjust the angles and positions of the sample. The geometry of the goniometer and sample stage is shown in Figure 3.4, with the angles involved in the scans of this study being labeled. As shown in Figure 3.4, the 2$\theta$ angle is defined as the angle between the incident X-ray beam and the direction of the detector (the detected diffracted X-ray beam), $\omega$ is the angle between the incident X-ray beam and the sample surface, $\chi$ is the tilted angle of the sample stage and $\phi$ is the stage's in-plane orientation.

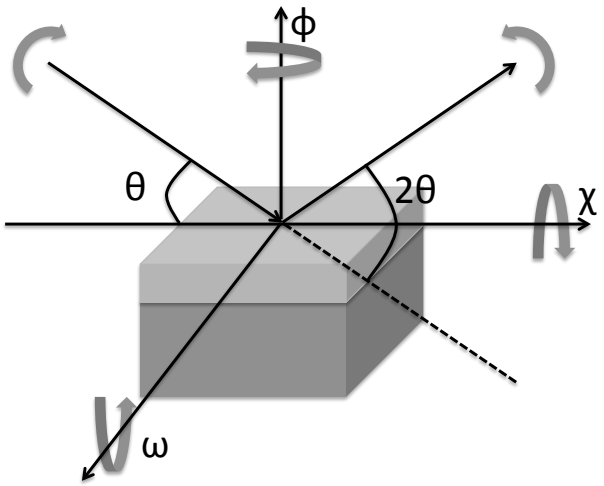


Figure 3.4: Schematic of axis in the X-ray diffractometer.

In this work, XRD scans employed in the structural characterization included 2θ-ω scan, ω scan with 2θ being fixed (i.e. the Rocking curve scan) and ϕ scan.

#### 3.2.1.1 2θ-ω scan

In the 2θ-ω scan scan, both the X-ray source and detector are scanning with the relationship $\omega = (2\theta)/2 \pm \varphi$. φ is a tiny angle used to correct the tilt of single crystalline substrate with respect to the sample surface. By doing a wide scan (2θ = 20° - 90° in this study), lattice planes in the film and the substrate that are parallel to the surface of the sample can be detected. In this study, 2θ-ω scans were used to determined the phase composition of the sample and distinguish between polycrystalline and highly textured films.

#### 3.2.1.2 ω scan (Rocking curve)

ω scan is performed by scanning ω in a $(2\theta)/2 \pm \Delta\omega$ range with 2θ being fixed at certain value which satisfies the Bragg's law. In ideal case, the ω scan for a prefect crystal will produce a single line at ω=(2θ)/2. In reality, the peak will have some width due to the

instrument broadening and defects in the crystalline sample. For high resolution XRD scan, the full width half maximum (FWHM) of the peak is influenced by the crystallites sizes as well as the tilt of the crystallites with respect to each other.

#### 3.2.1.3 $\phi$ scan

The $\phi$ scan is employed to determine the orientation relationship between the grown film and the substrate. Once the phase composition and lattice plane parallel to the film surface are identified, $\phi$ scan is performed by scanning $\phi$ in a 360° range while fixing $2\theta$, $\omega$ and $\chi$ at certain values. The value of $\chi$ is determined by making certain tilted lattice plane parallel to the horizontal plane, and the $2\theta$ and $\omega$ values are determined by the Bragg's law of this particular lattice plane. By doing such scans for both the film and the substrate, the orientation relationship between them can be determined.

### 3.2.2 X-Ray reflectivity (XRR)

X-ray reflectivity (XRR) technique was used to determine the thicknesses of grown films. A $2\theta/\omega$ scan was conducted within a small range of $2\theta$ = 0 - 5°, with the same optic configuration as in XRD scans.

The incoming X-ray beam intensity is completely reflected below a certain incident angle $\theta_c$, the value of which is typically below 1°. [85] Above $\theta_c$, part of the incoming intensity is reflected and part of it can transmit through the material. If the sample consists of more than one layer, the same thing will happen at the interfaces between different layers. The beam reflected by the surface and each interface will interfere with each other, and form oscillation of intensity with the variance of phase difference due to the $2\theta$ scan. Therefore, thickness of the measured film should be inversely proportional to the oscilla-

tion period and can be estimated as

$$t = \lambda/\Delta(2\theta) \tag{3.3}$$

in which $\Delta(2\theta)$ is the phase difference between the two consecutive peaks of XRR pattern. [86]

Besides the film thickness, simulation of XRR patterns can also provide information on film density and roughness of involved surface and interfaces. While the magnitude of oscillation is related to the difference between densities of different layers, the oscillation magnitude decays due to the roughness of film surface and interfaces. [87]

In this study, the measured XRR patterns were simulated by Rigaku GXRR software. Figure 3.5 shows an XRR pattern of a $NbO_2$ film deposited on sapphire substrate with a Nb capping layer. As is indicated by the simulation results, the thickness of $NbO_2$ and Nb layer were $\sim$111 nm and $\sim$2.6 nm, respectively.

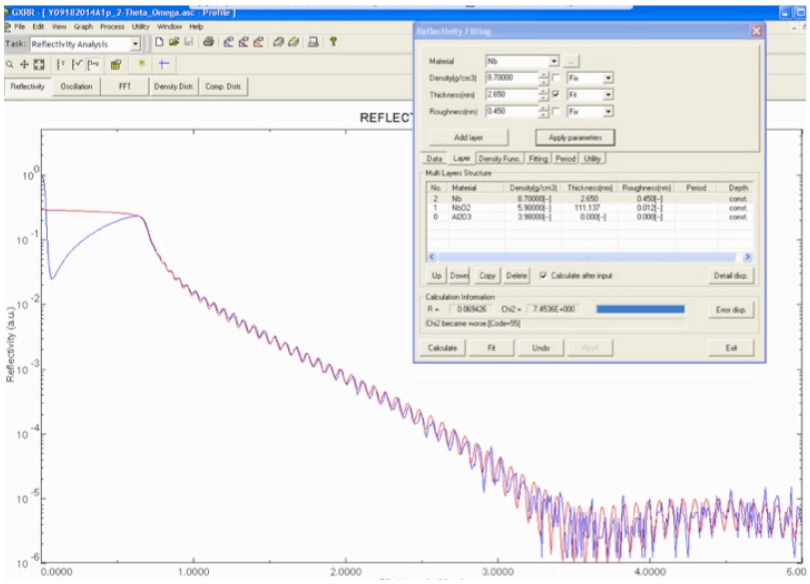


Figure 3.5: A measured XRR profile of a Nb/$NbO_2$/$c$-$Al_2O_3$ sample (blue) and corresponding simulated curve (red).

### 3.2.3 Atomic force microscopy (AFM)

The film surface morphology was characterized by atomic force microscopy (AFM) (Cypher, Asylum Research Inc.). A schematic of the working principle of AFM is shown in Figure 3.6.

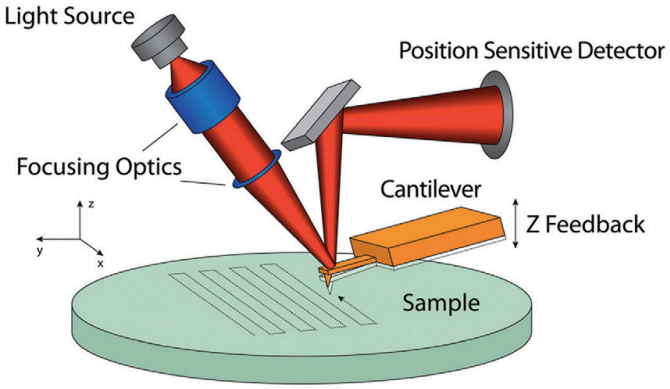


Figure 3.6: Schematic of AFM instrument. [88]

AFM provides a three-dimensional profile of the sample surface, by probing the force between a sharp tip and sample surface at a very short distance (0.2-10 nm). A cantilever with a sharp tip ($\sim$ 10 nm in radius) raster-scans the sample surface, and experiences the Van der Waals interaction between the tip and surface. A laser is bounced off the back of the cantilever onto a position sensitive photodiode detector, therefore the deflection of the cantilever can be characterized by changes in detected laser reflection.

All scans in this study were conducted using the tapping mode, during which the cantilever is oscillated near its resonant frequency. The scan rate was 1 Hz for $1\times1$ $\mu$m$^2$ image and 1.5 Hz for $20\times20$ $\mu$m$^2$ image. Due to the interaction between the tip and sample surface, the variation of tip-surface separation will result in the change in the oscillation amplitude of the cantilever. As the tip scans over the sample surface, the oscillation amplitude is maintained constant by adjusting the height of the tip, via a feedback-controlled

piezoelectric actuator. A map of the surface roughness is then produced from the cantilever deflection detected by the photodiode detector.

### 3.2.4 Raman spectroscopy

Raman spectra in this study were measured by an inVia Raman microscope (Reinshaw system Ltd.).

Raman spectroscopy is a technique based on the inelastic scattering of light by the studied sample. In a typical Raman experiment, a laser with monochromatic radiation is used to irradiate the sample. The studied sample absorbs photons from the radiation source, and emits photons whose frequency is shifted up or down compared to the original frequency. It is the shift in frequency (/wavelength) of radiation that provides the chemical and structural information of studied samples.

The Raman scattering processes are illustrated in Figure 3.7. The incident photon is absorbed by the sample and induces a transition from ground state to a "virtual state", and a new photon is emitted when a transition from this "virtual state" takes place. In Rayleigh scattering, the scattered photon results from the transition from the "virtual state" to the ground state, with no change in energy therefore the photon is elastically scattered. For Raman scattering, the excited states of sample vibration are also involved in the transition and the photons are inelastically scattered. There are two types of Raman scattering: Stokes and anti-Stokes, determined by the initial and final vibrational states in the process as is illustrated in Figure 3.7.

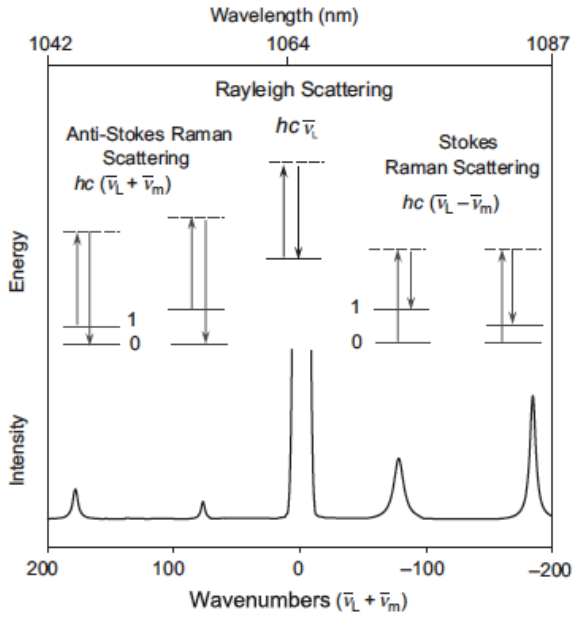


Figure 3.7: Schematic illustration of Rayleigh scattering as well as Stokes and anti-stokes Raman scattering. The laser excitation frequency (νL) is represented by the upward arrows and is much higher in energy than the molecular vibrations. The frequency of the scattered photons (downward arrows) is unchanged in Rayleigh scattering but is of either lower or higher frequency in Raman scattering. The dashed lines indicate the "virtual state". [89]

The Raman effect is based on the change of polarizability $\alpha$ of the sample in electric field $E$. The electromagnetic filed of the incident radiation induces an electric dipole moment $P$ in the sample, determined by the relation $P = \alpha E$. The oscillation of the induced dipole moment also produces electromagnetic radiation, including the dominant Rayleigh radiation and the very small amount of Raman scattered radiation. The intensity of the Raman scattered radiation $I_R$ is given by:

$$I_R \propto \nu^4 I_0 N \left(\frac{\partial \alpha}{\partial Q}\right) \tag{3.4}$$

where $I_0$ is the incident laser intensity, $N$ is the number of scattering molecules in a given state, $\nu$ is the frequency of the exciting laser, $\alpha$ is the polarizability of the molecules, and $Q$ is the vibrational amplitude. Therefore only vibrations that cause a change in polarizability

are Raman active.

## 3.3 Transport characterization

### 3.3.1 Temperature dependence of resistivity

Temperature dependence of film resistivity was measured on a current-in-plane device illustrated in Figure 3.8. Assuming that the measured resistance is due to the part of film between a pair of contacts, the resistivity can be calculated as

$$\rho = \frac{Rlt}{w} \tag{3.5}$$

in which $R$ is the measured resistance between contacts, $l$ is the length of contact edge, $t$ is the thickness of measured thin film, and $w$ is the width of gap between a pair of contacts.

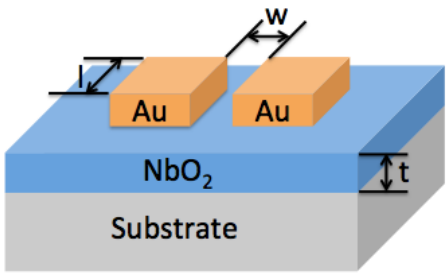


Figure 3.8: Schematic of a current-in-plane device for resistivity measurement.

The contacts were fabricated from 20 nm Ti and 100 nm Au layers, with size of 250 $\mu$m $\times$ 250 $\mu$m separated by 10 $\mu$m. A photolithography procedure to fabricated Ohmic contacts was employed, and the steps are listed below:

1. Spin clean the sample with methanol and isopropanol, then bake at 100 °C for 1 minute.

2. Spin on photoresist AZ nLof 2020 at spin rate of 4000 rpm for 30 s.

3. Bake the sample at 100 °C for 1 minute.

4. Expose the photoresist to UV at constant power of 275 W for 36 s.

5. Bake the sample at 110 °C for 1 minute.

6. Develop the photoresist in AZ 300 MIF developer for 1 minute.

7. Soak the sample in DI water for a few seconds, then dry the sample with UHP $N_2$. Check the patterns under optical microscope.

8. Use electron beam evaporator to deposit 200 Å Ti at a rate of 2 Å/s followed by 1000 Å at a rate of 3 Å/s.

9. Soak the sample in an acetone ultrasonic bath with lower power to lift of the remaining photoresist, leaving only the metal contacts.

Film resistance as a function of temperature was characterized by a Versalab system (Quantum Design Inc.) from 150 K (or 200 K) to 400 K, with a ramp rate of 2 K/min (or 5 K/min). The excitation current was 1 $\mu$A.

### 3.3.2 MIT under electric field

MIT of $NbO_2$ under electric field were characterized by applying electric field through the films. A vertical device was fabricated for the characterization, the schematic of which is shown in Figure 3.9 (a). In this vertical device, the bottom electrode is a $\sim$ 50 nm TiN layer coated on the Si(100) substrate, the connection to which was made by cold-pressing indium into the scratches made at the sample corners. After the deposition of a $NbO_2$ layer, another layer of Nb was then deposited before the sample was exposed to air. This capping layer served as the top electrode, and contacts were defined following standard lithography process. The step-by-step procedures are listed below.

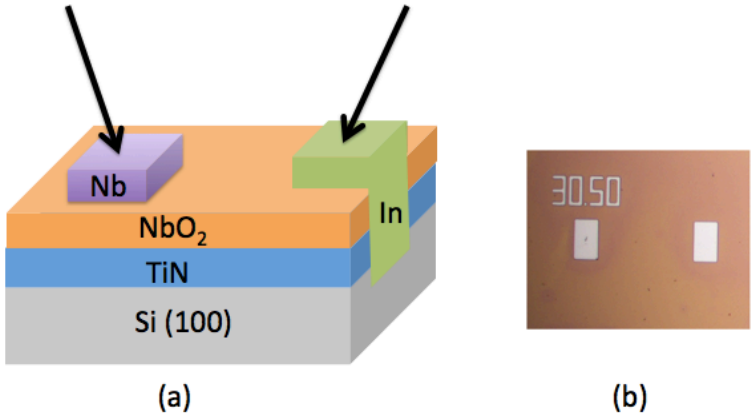


Figure 3.9: (a) Schematic of Nb/$NbO_2$/TiN vertical device structure; (b) the optical image of 30 $\mu$m $\times$ 50 $\mu$m (Nb) top contacts.

1. Spin clean the sample with methanol and isopropanol, then bake at 100 °C for 1 minute.

2. Spin on photoresist AZ4210 at spin rate of 4000 rpm for 30 s.

3. Bake the sample at 100 °C for 1 minute.

4. Expose the photoresist to UV at constant power of 275 W for 36 s.

5. Develop the photoresist in a 3:1 solution of DI water:AZ400K developer for 1 minute.

6. Soak the sample in DI water for a few seconds, then dry the sample with UHP $N_2$. Check the patterns under optical microscope.

7. Put the sample in the dry etching tool, and use the reactive ion etching (RIE) to remove the uncovered metal layer. The etching condition was: Pressure 100 mTorr, RIE power 120 W, $SF_6$ 40 SCCM. The etching rate was $\sim$ 10 nm/min.

8. Soak the sample in acetone ultrasonic bath with low power to remove the photoresist.

9. Soak the sample in DI water and dry it with UHP $N_2$.

Voltage and current sweeps were performed using a Keithley 2635 source meter with tungsten tips (diameter = 5 $\mu$m). To reduced the effects of Joule heating, pulsed mode was

employed, with pulse-on time of 1 ms and pulse-off time of 10 ms.

### 3.3.3 Temperature dependence of Seebeck coefficient

Temperature dependence of the Seebeck coefficients $S$ of some deposited films was characterized by the Thermal Transport Option (TTO) of a Physical Property Measurement System (PPMS) (Quantum Design Inc.).

The thermoelectric Seebeck effect is characterized by an electrical voltage drop accompanying a temperature drop across the sample after a heat pulse is applied at one end of the sample. As is illustrated by Figure 3.10, the sample is mounted to the thermal transport sample puck in a four-probe geometry. The copper leads are adhered to the sample by epoxy bond, and the heater and thermocouple shoes are screwed down onto the leads. During the measurement, a heat pulse is applied to one end of the sample by running a current through the heater. The temperature drop ($\Delta T = T_{hot} - T_{cold}$) and Seebeck voltage ($\Delta V = T_{+} - T_{-}$) between the two thermocouple shoes are measured and the Seebeck coefficient is determined as $S = \Delta V/\Delta T$.

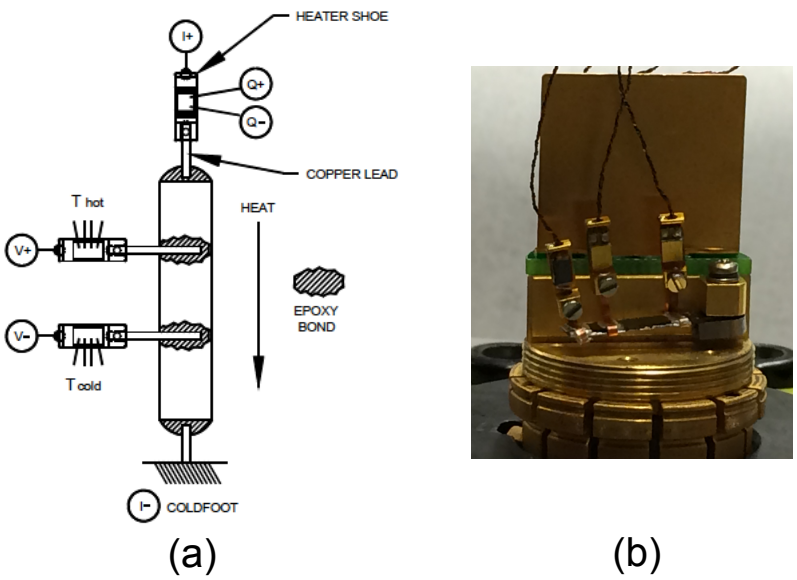


Figure 3.10: (a) Schematic thermal and electrical connection on a sample for thermal transport measurement [90]; (b) A representative photo of sample bonded to thermal transport sample puck.

In this study, measurement of Seebeck coefficient was conducted using the ”stability” mode. Data is first taken in the heater “off” state, then in the heater “on” state after the user-specified power is applied. For both states, measurement will not begin until the temperature stability at both hot and cold thermometers reach the specified stability criterion (dT/T $\leq$ 0.1% or dT $\leq$ 0.1 K).

# Chapter 4

# Epitaxial $NbO_2$ thin films

## 4.1 Introduction

Despite the attractive attributes of $NbO_2$, experimental studies on $NbO_2$ especially on thin films has remained limited, due to the difficulty in preparing $NbO_2$ films with highly pure phase. The uniqueness of RBTIBD technique has been introduced in Chapter 3, which has been employed to synthesize high quality epitaxial $VO_2$ films on various kinds of substrates. [91–93]

In this chapter, synthesis of epitaxial $NbO_2$ thin films on (0001) sapphire substrates using RBTIBD is introduced. Effect of growth conditions $Ar/O_2$ flow rate (i.e. the Nb/O ratio in chamber) and substrate temperature on film property are discussed. It is demonstrated that the film deposited under optimized conditions contains highly pure $NbO_2$ phase with good crystallinity and smooth surface. Film conductivity is characterized as a function of temperature and the conduction mechanism is discussed.

## 4.2 Effect of $Ar/O_2$ 80/20 mixture flow rate

Due to the complexity of the Nb-O system, it is crucial to obtain the right stoichiometry to avoid formation of secondary phases during deposition. For $NbO_2$ with right phase,

slight departures from stoichiometric composition can induce various type of intrinsic defects, resulting in modifications of structural and transport properties. Tuning the flow rate of $Ar/O_2$ 80/20 mixture is the most straightforward way to adjust the Nb/O ratio in chamber, and was employed as the primary method to optimize the stoichiometry of deposited films.

### 4.2.1 Phase composition

A set of niobium oxide thin film samples were deposited under conditions listed in Table 4.1. The $Ar/O_2$ 80/20 mixture flow rate was explored in a wide range between 2 SCCM and 8 SCCM, with all other deposition condition parameters remaining the same. Combining the Ar flow fed through the ion source, the corresponding $O_2$ partial pressure values were calculated and included in the table.

| Deposition conditions | S1 | S2 | S3 | S4 | S5 | S6 | S7 |
|---|---|---|---|---|---|---|---|
| $Ar/O_2$ Mix Flow Rate (SCCM) | 2 | 3 | 4 | 5 | 6 | 7 | 8 |
| $O_2$ Partial Pressure (%) | 0.49 | 0.72 | 0.95 | 1.18 | 1.40 | 1.61 | 1.82 |
| Process Pressure (mTorr) | 0.9 | 0.9 | 0.9 | 0.9 | 1.0 | 1.0 | 0.9 |
| Substrate Temperature (°C) | 550 | 550 | 550 | 550 | 550 | 550 | 550 |
| Positive Target Bias (V) | 20 | 20 | 20 | 20 | 20 | 20 | 20 |
| Negative Target Bias (V) | 900 | 900 | 900 | 900 | 900 | 900 | 900 |
| DC Pulse Frequency (kHz) | 71.43 | 71.43 | 71.43 | 71.43 | 71.43 | 71.43 | 71.43 |
| Positive Duty Cycle ($\mu$s) | 3 | 3 | 3 | 3 | 3 | 3 | 3 |
| Cathode Ar Flow Rate (SCCM) | 10 | 10 | 10 | 10 | 10 | 10 | 10 |
| Cathode Current (A) | 7 | 7 | 7 | 7 | 7 | 7 | 7 |
| Anode Ar Flow Rate (SCCM) | 70 | 70 | 70 | 70 | 70 | 70 | 70 |
| Anode Current (A) | 6.5 | 6.5 | 6.5 | 6.5 | 6.5 | 6.5 | 6.5 |

Table 4.1: Deposition condition parameters of niobium oxides thin films, with $Ar/O_2$ 80/20 mixture flow rate varying between 2 SCCM and 8 SCCM and other conditions remaining constant.

Phase composition in the deposited films were characterized by XRD combined with Raman spectroscopy. XRD 2θ-ω scans from 20° to 90° and Raman spectra between 100 $cm^{-1}$ and 1000 $cm^{-1}$ are shown in Figure 4.1.

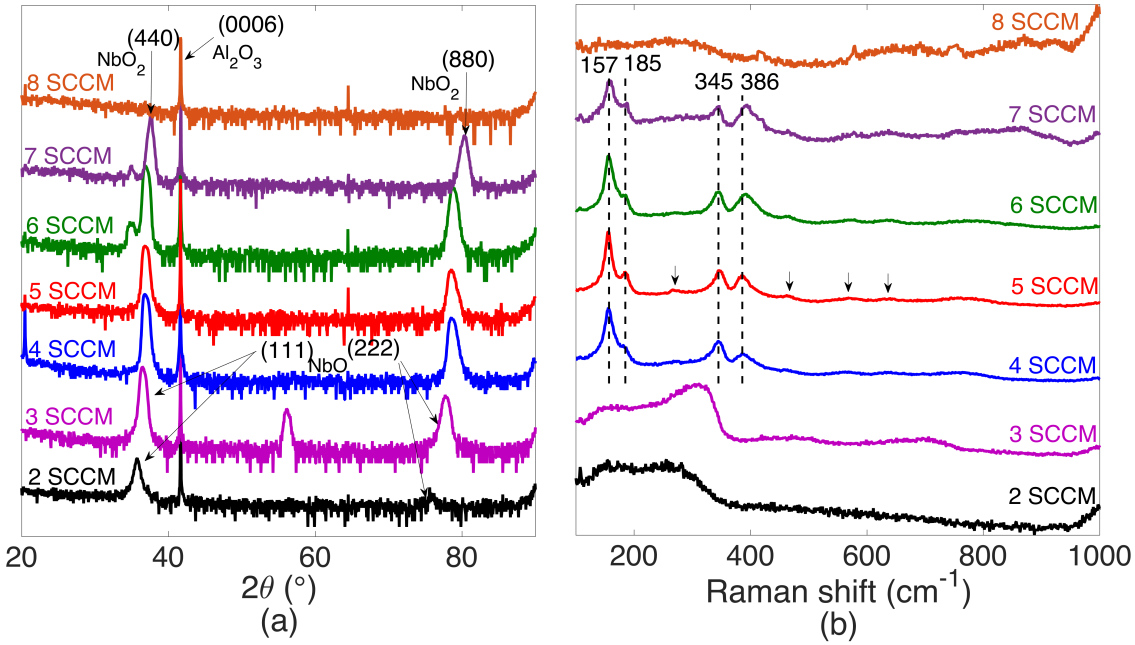


Figure 4.1: (a) XRD 2θ-ω scans and (b) Raman spectra of niobium oxide thin films deposited with $Ar/O_2$ 80/20 mixture flow rates from 2 SCCM to 8 SCCM.

As is shown in Figure 4.1 (b), for films deposited with $Ar/O_2$ mixture flow rate being from 4 SCCM to 7 SCCM, the essential Raman features match well with the reported Raman spectra of tetragonal $NbO_2$ films. [24, 26, 27] The X-ray diffraction peaks at 2θ $\sim 37^\circ$ and 2θ $\sim 79^\circ$ in the corresponding XRD 2θ-ω profiles are therefore identified as (440) and (880) of tetragonal $NbO_2$, respectively. No X-ray diffraction peaks or Raman bands of secondary phases are observed. The presence of only one out-of-plane diffraction orientation indicates that the films are highly-textured. For the sample deposited with higher $Ar/O_2$ 80/20 mixture flow rate (8 SCCM), no distinct features are observed in either XRD scan or Raman spectrum, suggesting an over-oxidized amorphous $NbO_{2+x}$ film.

For films deposited with $Ar/O_2$ mixture flow rate being 2 SCCM and 3 SCCM, the absence of $NbO_2$ features in Raman spectra suggests that some less oxidized phases are formed. The X-ray diffraction peaks at 2θ $\sim 36.5^\circ$ and 2θ $\sim 78^\circ$ are ascribed to NbO (111) and NbO (222), respectively. [94] X-ray ϕ scans were performed on (002) NbO

diffraction peaks at $2\theta = 44.5^\circ$ and $\chi = 52.5^\circ$ and $(01\bar{1}2)$ sapphire diffraction peaks at $2\theta = 25.5^\circ$ and $\chi = 12.8^\circ$, which are shown in Figure 4.2. As is suggested by the figure, the orientation relationship between the NbO film and sapphire substrate can be expressed as $\langle 110\rangle(111)\text{NbO}||\langle 10\bar{1}0\rangle(0001)\text{Al}_2\text{O}_3$. The optimized condition of $\phi$ scan on (002) NbO ($2\theta = 44.5^\circ$ and $\chi = 52.5^\circ$) is slightly off from the condition determined by the standard lattice parameter of NbO ($2\theta = 42.9^\circ$ and $\chi = 54.7^\circ$). [94] Natural NbO takes a defective rock salt structure, with 25% ordered vacancies in niobium and oxygen sub-lattices. [95] Since growth conditions especially the Nb/O ratio were not optimized for NbO growth, the discrepancy of diffraction peak positions from ideal values could be related to the variation in the existence of vacancies in deposited films.

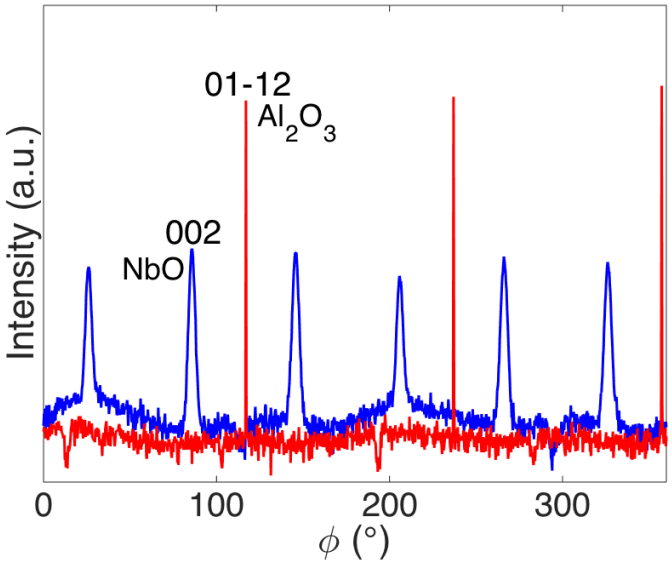


Figure 4.2: In-plane $\phi$ scan of (002) diffraction peak ($2\theta = 44.5^\circ$ and $\chi = 52.5^\circ$) of NbO (blue) and $(01\bar{1}2)$ diffraction peak ($2\theta = 25.5^\circ$ and $\chi = 12.8^\circ$) of sapphire substrate (red).

### 4.2.2 Microstructures

Another set of $NbO_2$ thin film samples were deposited with the $Ar/O_2$ mixture flow rate varying in a smaller range between 5 SCCM and 6.5 SCCM with smaller steps, while

all other condition parameters remaining the same. The growth conditions are listed in Table 4.2. Films were deposited for 30 min, with thicknesses of (105-115) nm.

| Deposition conditions | S1 | S2 | S3 | S4 | S5 | S6 | S7 | S8 | S9 |
|---|---|---|---|---|---|---|---|---|---|
| $Ar/O_2$ Mix Flow Rate (SCCM) | 5 | 5.3 | 5.5 | 5.7 | 5.9 | 6 | 6.1 | 6.3 | 6.5 |
| $O_2$ Partial Presssure (%) | 1.18 | 1.24 | 1.29 | 1.33 | 1.37 | 1.40 | 1.42 | 1.46 | 1.50 |
| Process Pressure (mTorr) | 1.1 | 1.1 | 1.1 | 1.1 | 1.1 | 1.1 | 1.1 | 1.1 | 1.15 |
| Substrate Temperature (°C) | 500 | 500 | 500 | 500 | 500 | 500 | 500 | 500 | 500 |
| Positive Target Bias (V) | 20 | 20 | 20 | 20 | 20 | 20 | 20 | 20 | 20 |
| Negative Target Bias (V) | 900 | 900 | 900 | 900 | 900 | 900 | 900 | 900 | 900 |
| DC Pulse Frequency (kHz) | 71.43 | 71.43 | 71.43 | 71.43 | 71.43 | 71.43 | 71.43 | 71.43 | 71.43 |
| Positive Duty Cycle ($\mu$s) | 3 | 3 | 3 | 3 | 3 | 3 | 3 | 3 | 3 |
| Cathode Ar Flow Rate (SCCM) | 10 | 10 | 10 | 10 | 10 | 10 | 10 | 10 | 10 |
| Cathode Current (A) | 7 | 7 | 7 | 7 | 7 | 7 | 7 | 7 | 7 |
| Anode Ar Flow Rate (SCCM) | 70 | 70 | 70 | 70 | 70 | 70 | 70 | 70 | 70 |
| Anode Current (A) | 6.5 | 6.5 | 6.5 | 6.5 | 6.5 | 6.5 | 6.5 | 6.5 | 6.5 |

Table 4.2: Deposition condition parameters of $NbO_2$ films, with $Ar/O_2$ 80/20 mixture flow rate varying between 5 SCCM and 6.5 SCCM and other conditions remaining constant.

All deposited samples consist of tetragonal $NbO_2$ phase, as suggested by the Raman spectra (Figure 4.3 (b)). Films are highly textured with the only out-of-plane orientation being (110) of tetragonal $NbO_2$, no other diffraction peaks from films are observed in wide range XRD 2θ-ω scans from 20° to 90° (not shown here).

To characterize the variation of microstructures more precisely, XRD 2θ-ω scans were performed in a narrower range near diffraction peak of tetragonal $NbO_2$ (440) (from 35° to 43°) with finer steps and slower scanning rate (shown by Figure 4.3 (a)). As the $Ar/O_2$ mixture flow rate increases, the diffraction peak of tetragonal $NbO_2$ (440) shifts to larger 2θ values, corresponding to smaller lattice parameters of tetragonal $NbO_2$ along $a$-axis ($a_T$). As a reference, the black dashed line labels the position of (440) diffraction corresponding to the bulk tetragonal $NbO_2$ ($a$ = 13.70 $\AA$). [16]

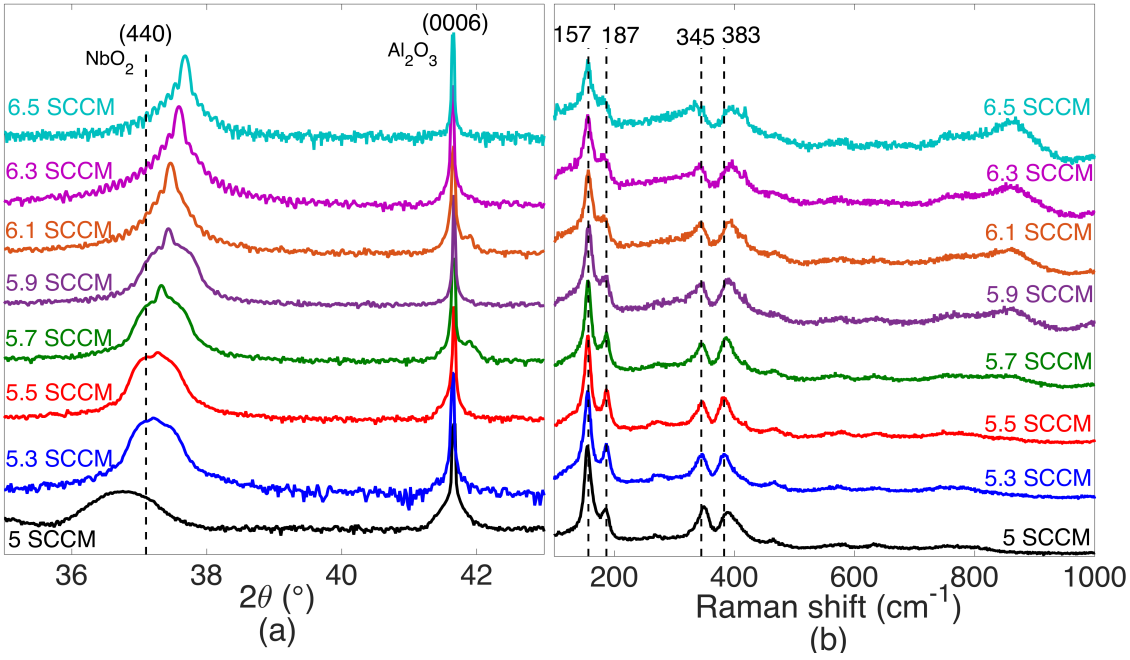


Figure 4.3: (a) XRD 2θ-ω scans and (b) Raman spectra of $NbO_2$ thin films deposited under $Ar/O_2$ 80/20 mixture flow rates from 5 SCCM to 6.5 SCCM.

Values of $a_T$ determined from the diffraction peak positions of (440) tetragonal $NbO_2$ as a function of $Ar/O_2$ mixture flow rate are shown in Figure 4.4 (a). The decrease of lattice parameter with the increase of oxygen content can be attributed to the decrease of Coulomb repulsion due to enhanced screening by oxygen ions.

For Raman spectra, it is found that for samples with lattice parameters being closest to the bulk value (deposited with 5.3 SCCM and 5.5 SCCM $Ar/O_2$ flow), the Raman bands around $\sim 385\ cm^{-1}$ exhibit the lowest frequency. The lowest frequency value ($383\ cm^{-1}$ for films deposited with 5.3 SCCM and 5.5 SCCM $Ar/O_2$ flow) is labeled by black dashed line in Figure 4.3 (b). To characterize the correlation between lattice parameter and frequency of this Raman band, a parameter $\Delta a_T$ is defined as

$$\Delta a_T = \left|\frac{a_{T,film} - a_{T,bulk}}{a_{T,bulk}}\right| \tag{4.1}$$

The value of $\Delta a_T$ and frequency of Raman band near 385 $cm^{-1}$ as functions of $Ar/O_2$ 80/20 flow rate are plotted in Figure 4.4 (b). It is demonstrated that the shift of this Raman band is monotonically related to the value of $\Delta a_T$.

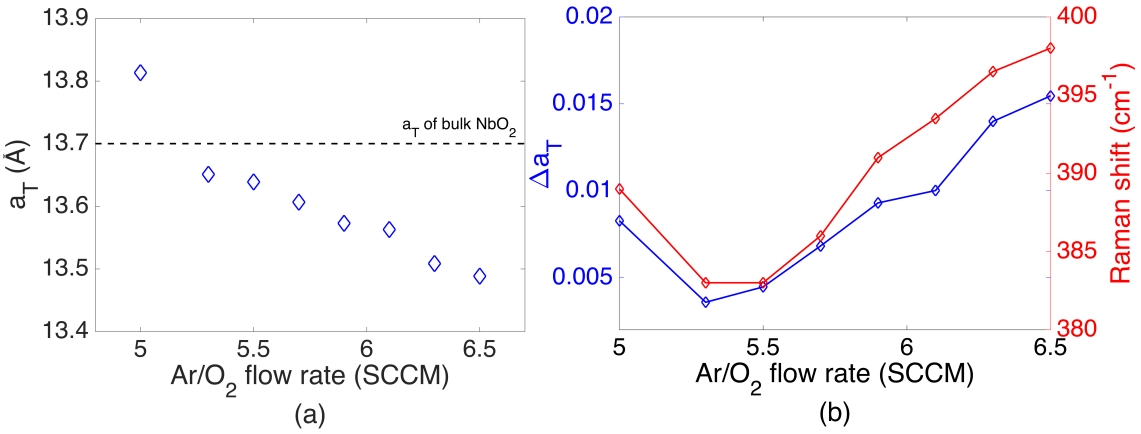


Figure 4.4: (a) Lattice parameter $a_T$ of tetragonal $NbO_2$; (b) $\Delta a_T$ and Raman shift as a function of $Ar/O_2$ 80/20 mixture flow rate.

Studies on Raman spectra of $NbO_2$ thin films remain limited. Referring to previous studies on Raman spectra of vanadium oxide and other oxides containing $MO_6$ octahedra of transitional metals, Raman bands in this intermediate frequency range can be related to different bending modes of Nb-O vibration within the $NbO_6$ octahedra. [96–98]

Blue shift of the Raman band near $\sim$ 385 $cm^{-1}$ with the increase of $Ar/O_2$ flow rate can be attributed to the decreased Nb-O distance corresponding to the lattice compression with the increase of oxygen content in films. The opposite trend with lower $Ar/O_2$ flow rate (5 SCCM) can be related to changes in interatomic force constants due to stronger Coulomb interaction or strain caused by point defects. [99] However this trend needs to be further confirmed by more samples (deposited with different $Ar/O_2$ flow rates smaller than optimal value), since there is only one relevant data point in this set of samples.

### 4.2.3 Transport properties

Temperature-dependent electrical transport was characterized for selected samples in Table 4.1 (sample S2, S4, S6 and S7, corresponding to samples deposited with $Ar/O_2$ flow rates being 3 SCCM, 5 SCCM, 7 SCCM and 8 SCCM respectively), and film conductivity as a function of temperature between 150 K and 400 K is shown in Figure 4.5 (a). Data of S7 near 150 K is not available due to the large sample resistance that exceeded the limit of VersaLab system. Among the four samples, S2 consists of NbO phase and S7 consists of over-oxidized $NbO_{2+x}$ phase, as is suggested by XRD and Raman results. Difference in phase composition results in variance in electrical transport properties. While film conductivity decreases monotonically with the increase of oxygen content, sample S2 demonstrates much higher conductivity and much weaker temperature dependence than other samples.

Arrhenius fitting was performed on conductivity data of the four samples. It turned out that the $\sigma$ vs. $1/T$ characteristics could be represented by the linear Arrhenius relation well under higher temperature (from 400 K down to $\sim$ 250 K), as is shown by the solid lines in Figure 4.5 (a). The activation energy of conduction obtained from fitting is plotted as a function of $Ar/O_2$ flow rate in Figure 4.5 (b). The deviation from the linear fitting at lower temperature corresponds to a reduction of activation energy with the decrease of temperature, which indicates variable range hopping (VRH) via defect states.

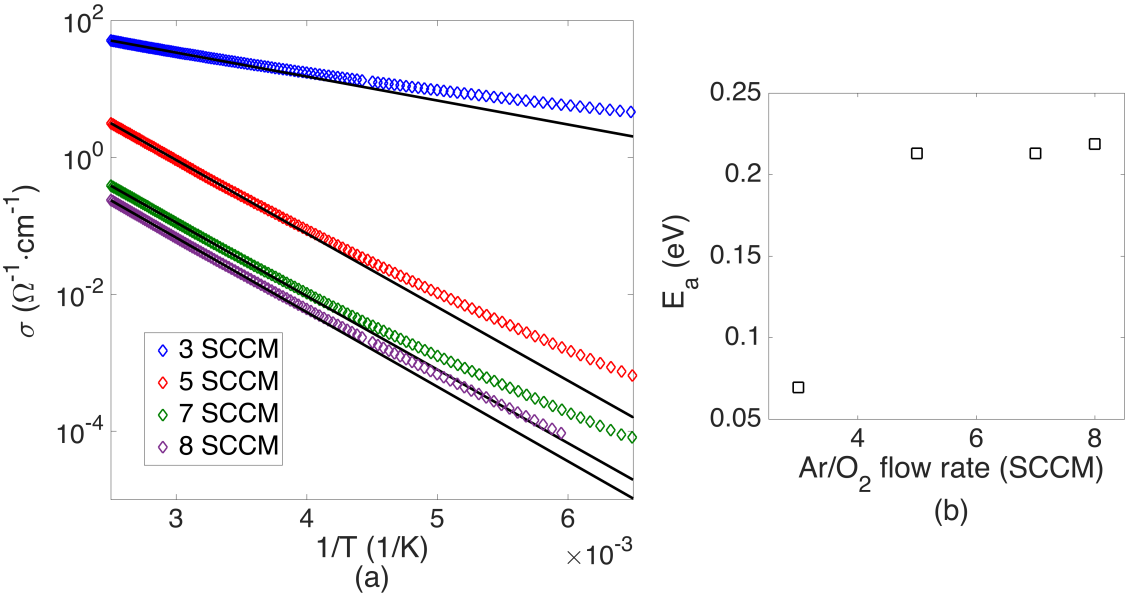


Figure 4.5: (a) Temperature dependence of film conductivity of selected $NbO_2$ samples in Table 4.1 (S2, S4, S6 and S7). Solid black lines represent corresponding Arrhenius fitting. (b) Fitted activation energy of conduction as a function of Ar/$O_2$ mixture flow rate during deposition.

Same characterization was performed on selected samples in Table 4.2 (sample S1, S3, S6 and S9, corresponding to samples deposited with Ar/$O_2$ flow rate being 5 SCCM, 5.5 SCCM, 6 SCCM and 6.5 SCCM respectively). The three samples except for S1 demonstrat slight increase in film resistivity and temperature dependence (as is shown by the activation energy of conduction in Figure 4.6 (b)) with the increase of Ar/$O_2$ flow rate during deposition. In contrast, sample S1 exhibits much higher conductivity and smaller activation energy.

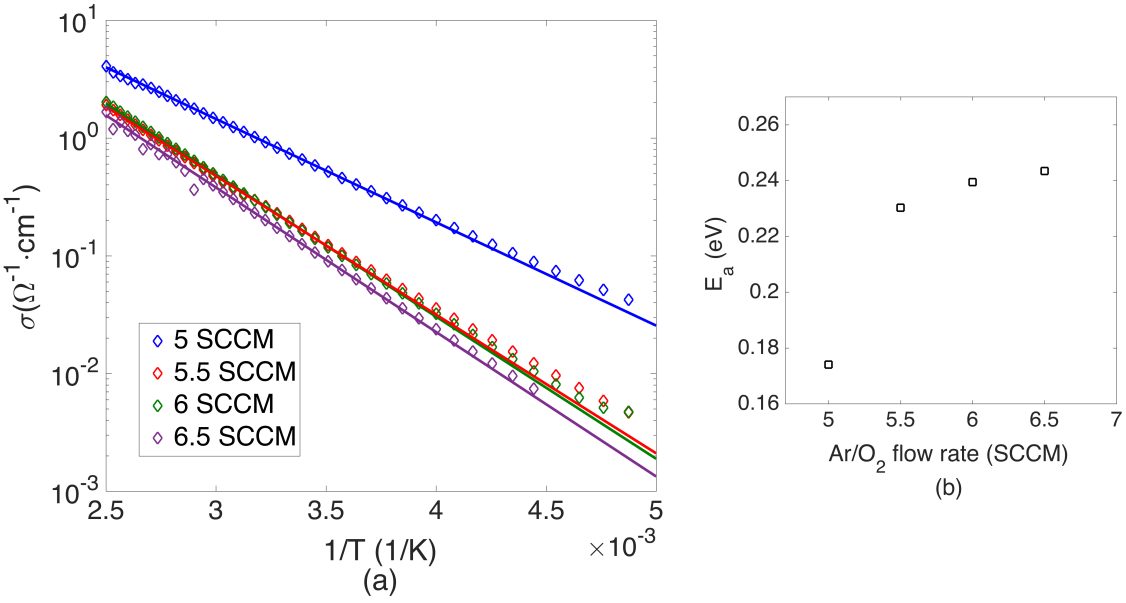


Figure 4.6: (a) Temperature dependence of film conductivity of selected $NbO_2$ samples in Table 4.2 (S1, S3, S6 and S9). Solid lines represent corresponding Arrhenius fitting. (b) Fitted activation energy of conduction as a function of $Ar/O_2$ mixture flow rate during deposition.

The exception of S1 on electrical transport is consistent with the structural characterization which demonstrates that only S1 has larger lattice parameter $a_T$ than bulk $NbO_2$. Moreover, as is indicated by the lattice parameter $a_T$ of S1 in Figure 4.4 (a), the dependence of lattice parameter $a_T$ on $Ar/O_2$ flow rate is larger below (5.3-5.5) SCCM. However, this trend needs to be further confirmed by more samples deposited with different $Ar/O_2$ flow rates around 5 SCCM, since it is only suggested by two data points ($a_T$ of S1 and S2) in this case.

It is therefore deduced that the $Ar/O_2$ flow rate required for stoichiometry is (5.3-5.5) SCCM under the studied growth conditions. Oxygen content is deficient in S1 while excessive in other samples. The predominant type of point defects and therefore dependence of physical properties on oxygen content are different, which is discussed briefly below referring to some early studies on bulk $NbO_2$ and on $VO_2$ thin films. [60, 100–102]

In deposited $NbO_2$ films, increased amount of point defects can be introduced by non-stoichiometry due to variation or dynamic fluctuation of deposition conditions. In principle, a predominance of either oxygen vacancies or niobium interstitials may account for oxygen-deficiency in $NbO_{2-x}$ films, while a predominance of either niobium vacancies or oxygen interstitials may account for oxygen-excess in $NbO_{2+x}$ films. [60, 100]

For oxygen deficient $NbO_{2-x}$ films, formation of either niobium interstitials or oxygen vacancies will result in doping of electrons. Defect reactions of niobium interstitials (with charge $z$ plus) and oxygen vacancies can be expressed by $2O_O^{\times} + Nb_{Nb}^{\times} \leftrightarrow O_2(g) + Nb_i^{z\bullet} + ze'$ and $2O_O^{\times} \leftrightarrow \frac{1}{2}O_2(g) + V_O^{2\bullet} + 2e'$ respectively using Kr*ö*ger-Vink notations. [60] The resultant electrons can be localized near niobium ions, resulting in $Nb^{(4-y)+}$ ions nearby and introducing multiple donor levels within the band gap. The increased conductivity and smaller activation energy of conduction can be attributed to the increased electron concentration and the presence of new donor levels. [101, 102]

For oxygen excessive $NbO_{2+x}$ films, niobium vacancies are more likely to form than oxygen interstitials due to the large size of $O^{2-}$ ions. [101, 103] Niobium vacancies exist as acceptors with localized holes ($O_2 \leftrightarrow Nb_V^{4'} + 4h^{\bullet} + 2O_O^{\times}$), inducing accepter levels in band gap. [100] However, it is noticed that for this set of samples the film conductivity decreases slightly with the increase of oxygen content above optimal value. Considering the much lower mobility of holes compared to electrons [104], it is expected that the film conductivity is less sensitive to increase in acceptor doping than to increase in donor doping. Moreover, the reduced Nb-O distance can also increase *p-d* overlap and further lift up the $e_g^{\pi}$, which could increase the size of the band gap and therefore the activation energy.

Summarizing briefly, properties of niobium oxide films are sensitive to the stoichiometry which can be effectively tuned by $Ar/O_2$ 80/20 mixture flow rate during deposition. It was determined that the $Ar/O_2$ mixture flow rate for the formation of tetragonal $NbO_2$ phase was between 4 SCCM and 7 SCCM, corresponding to oxygen partial pressure be-

tween 0.95% and 1.61%. The use of $Ar/O_2$ 80/20 mixture allowed for finer optimization of film stoichiometry. It was found that 0.2 SCCM difference in $Ar/O_2$ mixture flow rate, which corresponded to $\sim$ 0.15% difference in oxygen partial pressure, was able to result in visible variance in structural properties. Different dependence characteristics of structural and transport properties on oxygen content below and above optimal amount was observed, suggesting different predominant types of point defects in oxygen deficient and oxygen excessive growth. However, more samples (more data points below and above optimal oxygen stoichiometry) and characterization are needed to make any further conclusion on point defects in the deposited $NbO_2$ films.

## 4.3 Effect of substrate temperature

Substrates are heated by the heating lamp behind the Tantalum stage during deposition. A set of $NbO_2$ samples were grown on (0001) sapphire substrates under different temperatures with all other growth condition parameters remaining constant, as listed in Table 4.3.

| Deposition conditions | S1 | S2 | S3 | S4 | S5 |
|---|---|---|---|---|---|
| Substrate Temperature (°C) | 350 | 400 | 450 | 500 | 550 |
| Process Pressure (mTorr) | 1.1 | 1.1 | 1.1 | 1.1 | 1.1 |
| $Ar/O_2$ Mix Flow Rate (SCCM) | 5.5 | 5.5 | 5.5 | 5.5 | 5.5 |
| Positive Target Bias (V) | 20 | 20 | 20 | 20 | 20 |
| Negative Target Bias (V) | 900 | 900 | 900 | 900 | 900 |
| DC Pulse Frequency (kHz) | 71.43 | 71.43 | 71.43 | 71.43 | 71.43 |
| Positive Duty Cycle ($\mu$s) | 3 | 3 | 3 | 3 | 3 |
| Cathode Ar Flow Rate (SCCM) | 10 | 10 | 10 | 10 | 10 |
| Cathode Current (A) | 7 | 7 | 7 | 7 | 7 |
| Anode Ar Flow Rate (SCCM) | 70 | 70 | 70 | 70 | 70 |
| Anode Current (A) | 6.8 | 6.8 | 6.8 | 6.8 | 6.8 |

Table 4.3: Deposition condition parameters of $NbO_2$ films, with substrate temperature varying between 350 °C and 550 °C and other conditions remaining constant.

Raman spectra from 100 $cm^{-1}$ to 1000 $cm^{-1}$ and XRD 2θ-ω scans from 35 ° to 43 ° of

this set of samples are shown by Figure 4.7 (a) and (b), respectively. As is shown by the two figures, $NbO_2$ films demonstrat little variation in phase composition and microstructures within the investigated temperature range.

It is found that the measured XRD 2θ-ω profiles of $NbO_2$ films can be fitted by two peaks overlapping with each other. The fitting on profile of S1 (films deposited at 350 °C) is shown by Figure 4.7 (c) as an example. The tetragonal $NbO_2$ (440) peak can be fitted by a broad peak with lower intensity and a much sharp peak with higher intensity. Some samples in the set listed in Table 4.2 also demonstrated this type of XRD features (as is shown in Figure 4.3 (a)). Similar deconvolution characteristics has also been observed for epitaxial $VO_2$ films on sapphire (0001) substrates, and the broad and sharp peaks have been attributed to the strained and defective interface layer and relaxed top layer with less defects respectively. [100] Lattice parameters $a_T$ of tetragonal $NbO_2$ calculated based on the fitted peak positions, as well as extracted values of full width at half maximum (FWHM) of the broad and narrow peaks are plotted as function of heating temperature in Figure 4.7 (d) and (e) respectively (red for broad peak and green for narrow peak).

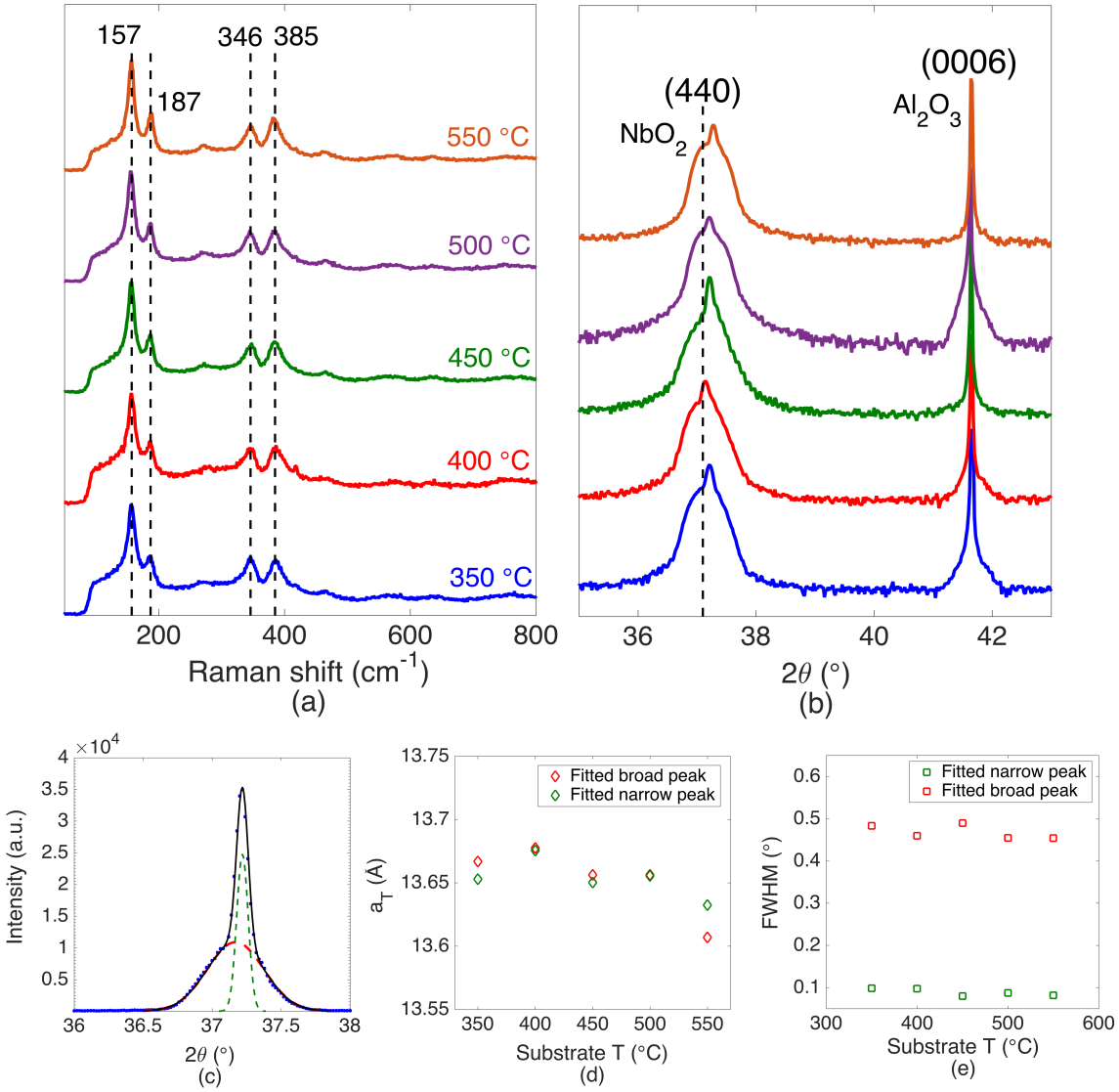


Figure 4.7: (a) Raman spectra and (b) XRD 2θ-ω scans of $NbO_2$ thin films deposited at different temperatures; (c) Deconvolution of $NbO_2$ (440) peak of sample S1, which can be fitted with two peaks; Deposition temperature dependence of (d) lattice parameter *a* of tetragonal $NbO_2$ and (e) $NbO_2$ (440) 2θ peak FWHM determined from two peak fitting on XRD 2θ-ω profiles (red for broad peak and green for narrow peak).

Temperature dependence of film conductivity is shown in Figure 4.8 (a) and the activation energy of conduction obtained from Arrhenius fitting (not shown in Figure 4.8 (a)) is plotted in Figure 4.8 (b) as a function of substrate heating temperature. Electrical transport

properties demonstrate little variance with the substrate heating temperature, which is in consistency with the characterization of microstructures. The observed consistency of film quality suggests that under this combination of deposition condition parameters, structural as well as transport properties of films are not dominated by substrate heating.

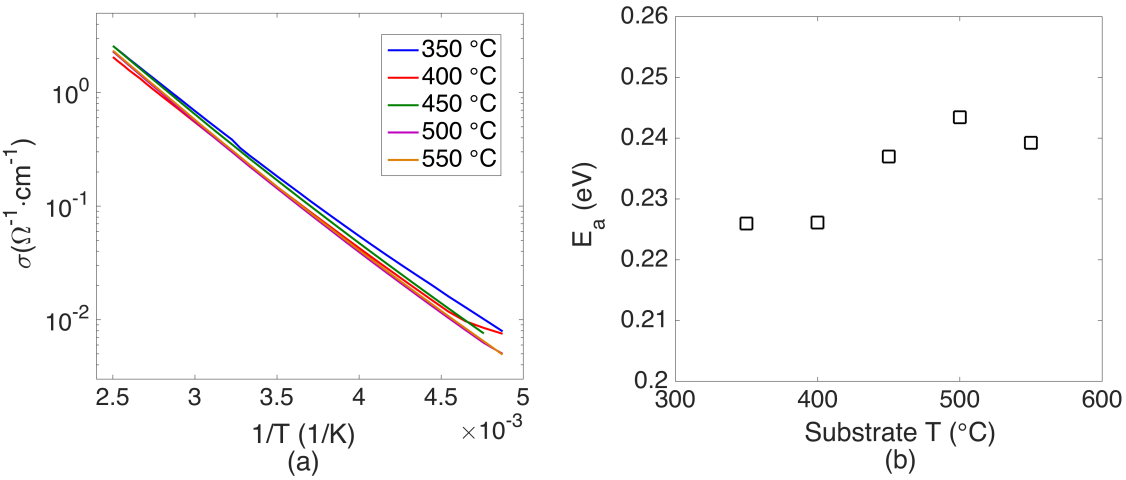


Figure 4.8: (a) Temperature dependence of film conductivity of $NbO_2$ thin films on (0001) deposited sapphire substrate at different temperatures; (b) Fitted activation energy as a function of substrate temperature during deposition.

## 4.4 Optimized $NbO_2$ films

With the effect of $Ar/O_2$ flow rate and substrate heating on film quality being investigated, more comprehensive structural and transport characterization was conducted on film deposited with these condition parameters being close to the optimal values (listed in Table 4.4). Film deposited under these conditions demonstrated a growth rate of $\sim$3.67 nm/min.

| Deposition conditions | Parameter values |
|---|---|
| Substrate temperature (°C) | 500 |
| Process pressure (mTorr) | 0.9 |
| $Ar/O_2$ mix flow rate (SCCM) | 5.5 |
| Target potential bias (V) | -900 and +20 |
| DC pulse frequency (kHz) | 71.43 |
| Positive duty cycle ($\mu$s) | 3 |
| Cathode Ar flow rate (SCCM) | 10 |
| Cathode current (A) | 7 |
| Anode Ar flow rate (SCCM) | 70 |
| Anode current (A) | 6 |

Table 4.4: Deposition condition parameters for $NbO_2$ on (0001) sapphire substrate.

### 4.4.1 Structural properties

Figure 4.9 (a) shows the X-ray 2θ-ω scan of the deposited $NbO_2$ thin film. The diffraction peaks from the film are observed at 2θ = 37.18° and 2θ = 79.21°. The peaks at 2θ = 41.63° and 2θ = 90.65° correspond to (0006) plane and (00012) plane of sapphire substrate, respectively. The thin film peaks correspond to (440) and (880) in tetragonal $NbO_2$, indicating the film is not only single phase but also highly textured. The lattice parameter $a_T$ is calculated to be $\sim$ 13.67 $\AA$ based on the 2θ value of diffraction peaks ((440) of tetragonal $NbO_2$). The lattice parameter is very close to that of single crystal $NbO_2$ (13.70 $\AA$) [16], implying that the film strain is fully relaxed. As is shown in the inset of Figure 4.9 (a), there are clear Kiessig fringes observed in the scan, which are indicative of the high quality epitaxy of the $NbO_2$ film with abrupt interfaces, uniform thickness, and low defect density.

To further characterize the crystallinity of the $NbO_2$ film, the rocking curves, i.e., ω scans were measured for the (440) diffraction peak of tetragonal $NbO_2$ and (0006) diffraction peak of sapphire substrate (Figure 4.9 (b)). Kiessig fringes can also be observed in the rocking curve. The peaks have been fitted to extract the FWHM value. The FWHM is 0.042° for (440) $NbO_2$ and 0.0093° for (0006) sapphire. The FWHM

for $NbO_2$ peak is smaller compared with previous reported values on $NbO_2$ thin films. FWHM of $\sim 0.07^\circ$ has been reported for (200) $NbO_2$ (15 nm) grown on (111) single crystal $(La,Sr)_2(Al,Ta)_2O_6$ substrate using molecular beam epitaxy [25], and FWHM of $\sim 0.18^\circ$ has been reported for (440) $NbO_2$ grown on (0001) sapphire substrate using DC magnetron reactive sputtering [18]. The smaller FWHM here indicates that the defect density is significantly reduced.

X-ray $\phi$ scans (Figure 4.9 (c)) were conducted on (400) $NbO_2$ diffraction peaks at $2\theta = 26^\circ$ and $\chi = 45^\circ$ and $(01\bar{1}2)$ sapphire diffraction peaks at $2\theta = 25.5^\circ$ and $\chi = 12.8^\circ$. The presence of six diffraction peaks from the (400) $NbO_2$ suggests that there are three equivalent orientations in the basal plane. While the $NbO_2$ film has only one out-of-plane orientation, three in-plane variants rotate $120^\circ$ from each other in the basal plane. Moreover, as is shown in Figure 4.9 (c), the off-axis $NbO_2$ (400) peaks and sapphire $(01\bar{1}2)$ peaks are offset by $30^\circ$. The *c*-plane of sapphire has three-fold symmetry and the structure of $NbO_2$ deposited on top is tetragonal. Therefore, the crystal of $NbO_2$ can have three preferred in-plane orientations in accordance to film and substrate structures. Combining the out-of-plane and in-plane XRD scans, the epitaxial relationship between the film and substrate can be summarized as $\langle 001\rangle(110)NbO_2||\langle 10\bar{1}0\rangle(0001)Al_2O_3$. The schematic of this orientational relation is illustrated in Figure 4.9 (d). In Figure 4.9 (d), the pseudo-rutile unit cell of tetragonal $NbO_2$ is used. Lattice parameter *a* of pseudo-rutile $NbO_2$ ($\sim 4.84$ *Å*) is close to *a* of sapphire ($\sim 4.76$ *Å*).

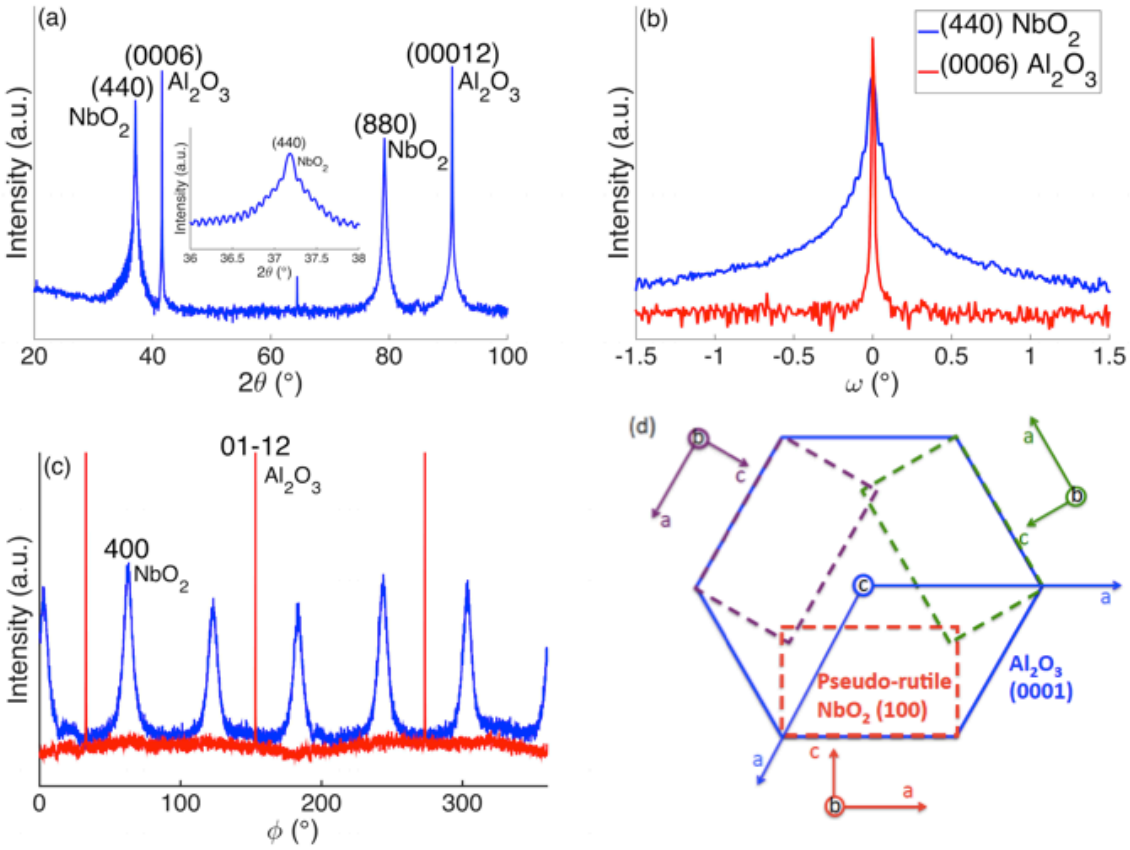


Figure 4.9: (a) 2θ-ω scan of $NbO_2$ thin film deposited on (0001) sapphire substrate, the inset shows 2θ-ω scan of (440) diffraction peak of tetragonal $NbO_2$; (b) ω scan of (440) diffraction peak of tetragonal $NbO_2$ and (0006) diffraction peak of sapphire substrate; (c) In-plane ϕ scan of (400) diffraction peak (2θ = 26° and χ = 45°) of tetragonal $NbO_2$ (blue) and (01$\bar{1}$2) diffraction peak (2θ = 25.5° and χ = 12.8°) of sapphire substrate (red); (d) Schematic representation of the epitaxial orientational relation between tetragonal $NbO_2$ and sapphire substrate.

A 1×1 $\mu m^2$ AFM image of the $NbO_2$ film is shown in Figure 4.10. The film appears to be very smooth, with a root mean square (RMS) of $\sim$ 0.12 nm. There are no cracks or pinholes observed in a 20×20 $\mu m^2$ area (not shown here). The smooth morphology of the film surface is due the fact that the substrate was directly exposed to the ion beam during the deposition. The ion beam could provide additional kinetic energies for the adatoms on the surface, which resulted in very smooth surface in crystallized oxide thin films. According to the applied voltage of ion source, this additional kinetic energy was $\sim$ 50 eV, which was

not enough to cause sputtering of $NbO_2$ film but could modify the surface morphology.

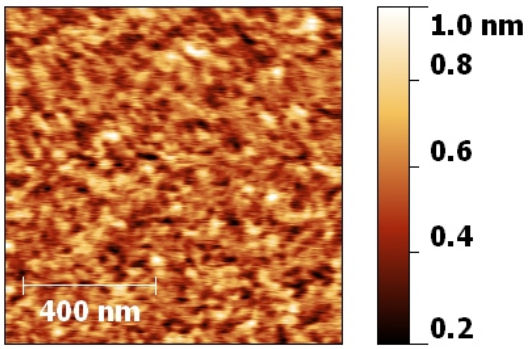


Figure 4.10: AFM image of $NbO_2$ thin film on (0001) sapphire substrate. The RMS surface roughness is $\sim 0.12$ nm.

Figure 4.11 shows the Raman spectra of the optimized $NbO_2$ film from 100 $cm^{-1}$ to 1000 $cm^{-1}$. The measured spectrum contains the background from the substrate (blue), and the spectrum with the contribution from substrate subtracted (red) is also shown in the figure. The Raman peaks agree well with the previous reports on the Raman spectra of $NbO_2$ films. [24, 26, 27] No Raman shifts corresponding to $Nb_2O_5$ [105, 106], which is the most stable niobium oxide, are observed. The Raman spectrum indicates that the film consist mainly the $NbO_2$ phase.

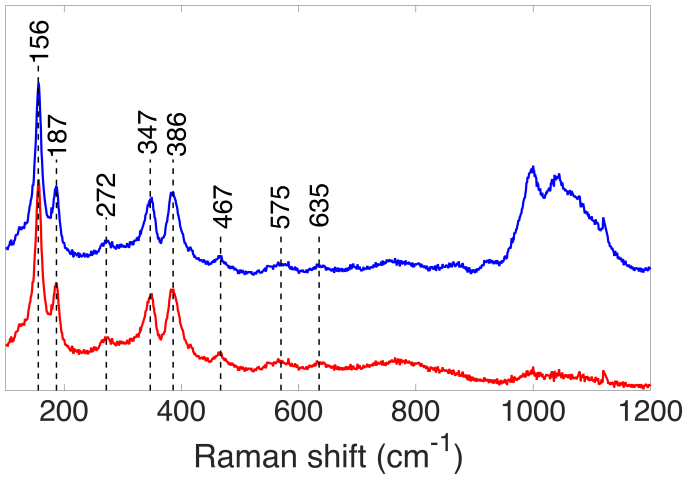


Figure 4.11: Raman spectrum (top) of $NbO_2$ on (0001) sapphire substrate excited by a 514 nm laser source. The spectrum at the bottom is after subtracting the background of the substrate.

Core level Nb 3*d* spectra and valence band density of states were measured using X-ray Photoemission Spectroscopy (XPS) to characterize the oxidation state of the film surface and near surface portions of the film by Ryan B. Come at Pacific Northwest National Laboratory. Both of them are shown in Figure 4.12. Figure 4.12 (a) shows Nd 3*d* spectra measured both before and after the sputter removal of surface carbon and oxide layers formed in the ambient conditions. The primary peak between 207 eV and 208 eV corresponds to $Nb^{5+}$, and the smaller peak between 205 eV and 206 eV corresponds to $Nb^{4+}$. The depth dependent signal intensity is given by

$$I(z) = I_0 e^{-z/\lambda} \tag{4.2}$$

where $\lambda$ is the electron inelastic mean free path, $z$ is the depth in the sample, and $I_0$ is the emission intensity at zero depth. By employing the angle-dependent measurement, it can be determined if the over-oxidation to $Nb^{5+}$ state is limited to the film surface. Based on published values of Nb and sapphire at the relevant binding energies, the value of $\lambda$ is

assumed to be 20 $\AA$. [107] By tilting the sample so that the photoelectron emission came from a glancing angle of 20°, the total integrated probe depth for 95% of the signal is $\sim$ 16 $\AA$. The $Nb^{4+}$ peaks are absent in spectrum measured at this glancing angle, indicating that the film is over-oxidized at the surface in ambient conditions. The bulk of the film therefore should have a significantly greater intensity of $Nb^{4+}$, and the surface is exclusively $Nb^{5+}$ phase.

To characterize the film below the surface, the surface layer was removed using *in-situ* ion beam sputtering with 500 eV $Ar^+$ ions and the XPS measurements were repeated. The peaks were fitted using a constrained model of the $3d^{5/2}$ and $3d^{3/2}$ peaks based on a 3:2 branching ratio between the spin-orbit split peaks. The $Nb^{4+}$ peak is found to be 48% of the overall signal, suggesting a significant amount of $Nb^{5+}$ remaining in the sample after sputter cleaning. Tilting to 20° glancing angle again showed a reduction in the $Nb^{4+}$ peak intensity to nearly zero intensity. These results suggest that even in ultrahigh vacuum conditions, the surface will readily oxidize to $Nb^{5+}$ by scavenging any available $O_2$ or $H_2O$. If we assume that the surface of the film is exclusively $Nb^{5+}$ for the first 13 $\AA$ of depth after sputtering and exclusively $Nb^{4+}$ for lower depth, then the integrated relative intensities of the $Nb^{4+}$ and $Nb^{5+}$ peaks should be 48% and 52%, respectively. This indicates that an $\sim$ 13 $\AA$ thick layer of disordered $Nb_2O_5$ is present on the surface even in extremely low oxygen pressures. From this, it can be concluded that the bulk of the film is $Nb^{4+}$, but the surface is highly unstable. Attempts to reduce the surface from $Nb^{5+}$ through *in-situ* vacuum annealing did not succeed presumably due to greater reaction kinetics at high temperatures with the scavenged $O_2$ and $H_2O$ molecules.

Valence band spectra shown in Figure 4.12 (b) confirm that there is significant intensity of Nb 4*d* electrons at lower binding energies above the edge of the O 2*p* band, in agreement with other works. [24]

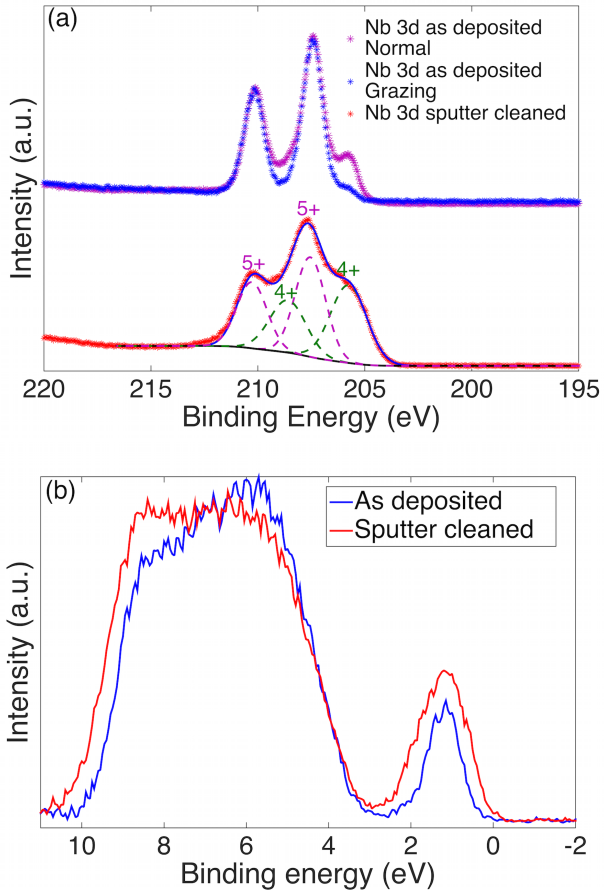


Figure 4.12: (a) (Top) Core level Nb 3*d* spectra obtained at incidence angle of 20° vs. 90° and (Bottom) normal emission after sputter cleaning, the grazing incidence (20°) probes exclusively the surface layer; (b) valence band XPS spectra of $NbO_2$ film on (0001) sapphire substrate. Courtesy of Ryan B. Comes from Pacific Northwest National Laboratory.

### 4.4.2 Transport properties

Temperature dependence of film resistivity between 180 K and 400 K is plotted in Figure 4.13. Sample resistance below 180 K exceeded the limit of VersaLab system, therefore the film resistivity below this temperature was not available. Resistivity of the thin film decreases from $\sim 10^3$ Ω·cm to $\sim 4 \times 10^{-1}$ Ω·cm in this temperature range, which is comparable to the reported values of thin film samples but much smaller than the reported values of bulk $NbO_2$ especially the single crystal samples ($\sim 10^4$ Ω·cm at room

temperature). [8, 57, 60]

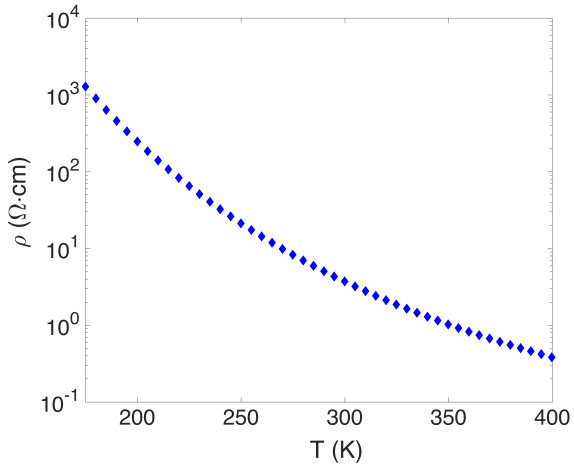


Figure 4.13: Resistivity of $NbO_2$ film as a function of temperature from 180 K to 400 K.

Figure 4.14 shows the Arrhenius plot of film conductivity, and the fitting to determine activation energy of conduction. The conductivity demonstrates Arrhenius dependence on temperature near 400 K, with the activation energy being $\sim$ 0.23 eV. As the temperature decreases, deviation from the Arrhenius fitting occurs below $\sim$ 270 K and increases as temperature decreases more. The decrease of activation energy with temperature suggests the contribution of VRH conduction via localized defect states.

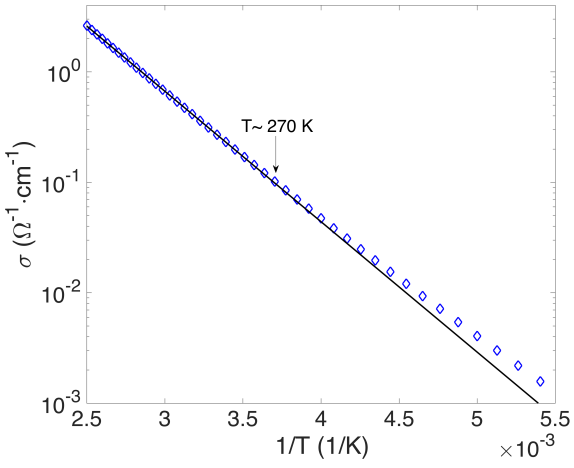


Figure 4.14: Arrhenius plot of film conductivity from 180 K to 400 K.

According to Zabrodskii and Zinov'eva method introduced in Chapter 2, the *ln[M(T)]* vs. *ln(T)* plot is shown in Figure 4.15. The slope near 400 K is close to 1, which agrees with the linear fitting in Figure 4.14. As temperature decreases, the slope decreases gradually and approaches 1/2 near 180 K, indicating that the contribution from VRH is close to the Efros-Shklovskii type.

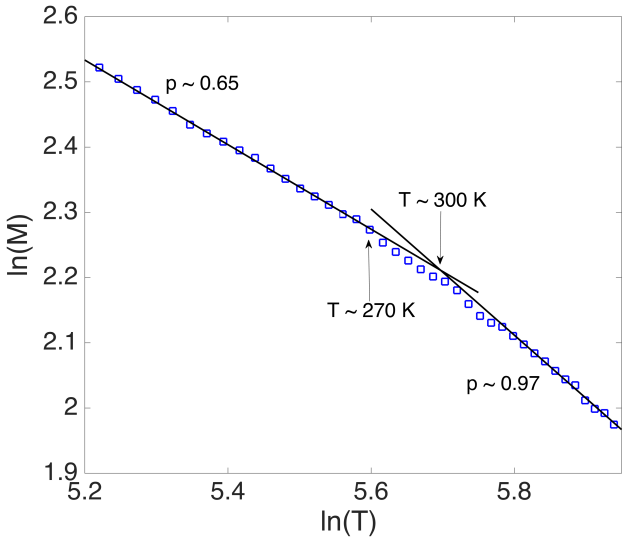


Figure 4.15: Plot of *ln[M(T)]* vs. *ln(T)* for $NbO_2$ thin film.

Small polarons tend to form when charge carriers move slowly enough to cause distortion of surrounding lattice. This criterion can be satisfied in non-crystalline solids, transitional metal or organic compounds, where slow carrier motion results from disorders or narrow energy bands. [41] Early studies on single crystal $NbO_2$ have reported thermally activated, adiabatic small polaron hopping (SPH) within temperature range $\sim$ (200 - 450) K, with activation energy values being $\sim$ (0.4 - 0.5) eV and differing along *a* and *c* axis. [57, 58] Here the measured $\sigma$ vs. $T$ data is fitted to the following equation describing the adiabatic SPH conduction.

$$\sigma = \frac{\sigma_0}{T} exp(-\frac{E_a}{k_B T}) \tag{4.3}$$

As is shown by Figure 4.16, the film conductivity data can be well reproduced by SPH model (given by Eq. 4.3) in a range larger than 100 K below 400 K, with fitted activation energy being $\sim$ 0.26 eV. T $\sim$ 270 K is labeled on the plot, and it is noticed that below this temperature the conductivity data starts to deviate from the the SPH model. It is known that a transition from SPH to VRH can be expected below approximately one-half of the Debye temperature ($\Theta_D/2$), therefore $\Theta_D$ of the deposited $NbO_2$ films can be estimated as $\sim$ 540 K. This estimated value is close to the reported value (598 K). [108]

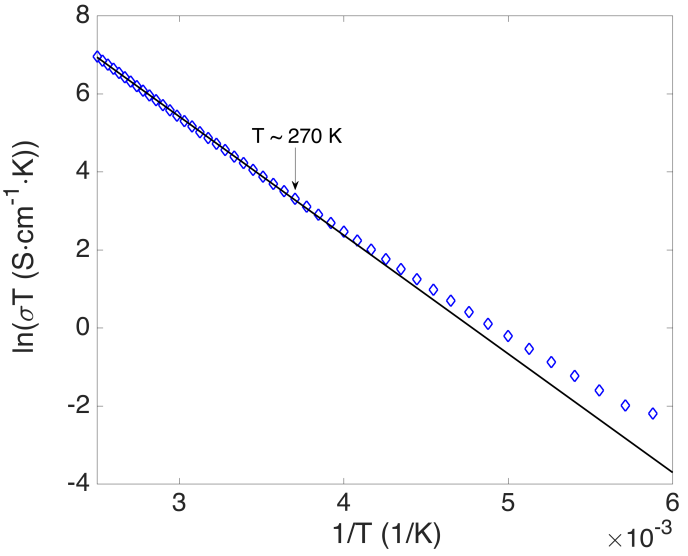


Figure 4.16: Temperature dependence of $NbO_2$ film conductivity fitted to Eq. 4.3.

However, the conductivity data alone is not sufficient to determine wether SPH conduction dominants within this temperature range. Other conduction mechanisms including band conduction, hopping among localized band tail states by thermally activated carriers can not be ruled out. Existence of hopping conduction can be supported by measurements on temperature dependence of Seebeck coefficient. It is known that temperature dependence of Seebeck coefficient $S$ provides method to decouple carrier mobility from the measured conductivity in terms of activation energy. [37, 42] For the case of SPH, the fitting of $S$ vs. $T$ data to Eq. 2.10 should give an activation energy which is for carrier

generation and therefore smaller than the activation energy obtained from the conductivity data. [38] However, such measurement on the $NbO_2$ film sample did not give reasonable result, which could be due to the large sample resistance.

Efros-Shklovskii VRH describes conduction by carriers' hopping between localized defect states within the band gap. In Mott's VRH model, the Coulomb interaction between hopping sites is neglected and density of defect states near Fermi level is treated as a constant. However for Efros-Shklovskii VRH model, a "Coulomb-gap" due to the interaction is taken into account which results in a power law dependence of density of defect states near Fermi level. Temperature dependence of conductivity for all dimensions is given by

$$\sigma(T) = \sigma_{0,ES} exp[-(\frac{T_{ES}}{T})^{1/2}], \quad T_{ES} = \frac{\beta_1 e^2}{\varepsilon_0 \xi k_B} \tag{4.4}$$

in which $\beta_1$ is a constant with a value of $\sim 2.8$, $\varepsilon_0$ is the static dielectric constant, $\xi$ is the localization length of the relevant electronic wave function. The most probable hopping distance and the average hopping energy are given by

$$\bar{R}_{hop,ES} = \frac{1}{4}\xi(\frac{T_{ES}}{T})^{1/2}, \quad \bar{W}_{hop,ES} = \frac{1}{2}k_B T(\frac{T_{ES}}{T})^{1/2} \tag{4.5}$$

As is shown in Figure 4.17, the $\sigma$ vs. $T$ data is well reproduced by Efros-Shklovskii VRH model from 180 K and the deviation occurs near $\sim$ 270 K. The occurrence of deviation agrees with the analysis using Zabrodskii and Zinov'eva method shown by Figure 4.14, in which the slope starts to increase near $\sim$ 275 K. The involved parameters are calculated and listed in Table 4.5.

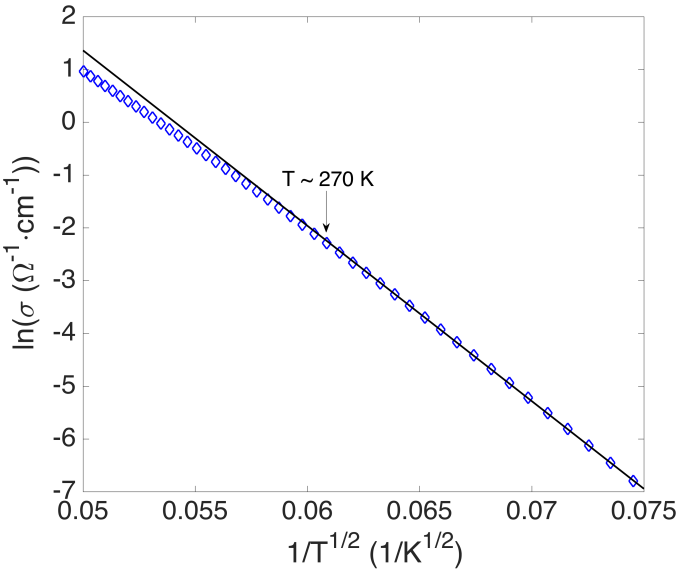


Figure 4.17: Efros-Shklovskii VRH plot of $NbO_2$ film conductivity and corresponding linear fitting.

| $\sigma_{0,ES}(\Omega^{-1}\cdot cm^{-1})$ | $T_{ES}^{1/2}(\mathrm{K}^{1/2})$ | $\xi(\AA)$ | $\bar{R}_{hop,ES}/\xi$ | $\bar{W}_{hop,ES}/k_BT$ |
|---|---|---|---|---|
| $6.4\times10^7$ | 332.2 | 6 | $83/\mathrm{T}^{1/2}$ | $166/\mathrm{T}^{1/2}$ |

Table 4.5: Values of relevant conduction parameters for $NbO_2$ film obtained by fitting $\sigma$ vs. $T$ data to Efros-Shklovskii VRH model.

For the Efros-Shklovskii VRH model to be applicable in the sample, the following criteria need to be satisfied. [48]

$$\bar{R}_{hop,ES}/\xi \geq 1,\ d \gg \bar{R}_{hop,ES},\ \bar{W}_{hop,ES} \geq k_BT, \tag{4.6}$$

$d$ is the thickness of the sample. Based the conduction parameters in Table 4.5, it can be seen that the above criteria are satisfied. Therefore, electrical transport within this temperature range (180 K to $\sim$ 270 K) is mainly mediated by the Efros-Shklovskii VRH.

VRH applies for insulating or amorphous materials where the amount of free carriers is smaller, and the conduction is mainly conducted by carriers hopping among states rising

from defects, impurities and other trapping centers. For the case of crystalline semiconductors, VRH can also dominate at low temperature when free carriers with high mobility are frozen out. [39] Similar conduction characteristics has been reported for $BiVO_4$ samples, where the dominating conduction process transited from SPH to ES-VRH below $\sim$ 250 K. The transition to ES-VRH process was assigned to the freezing out of higher temperature multi-phonon process and the onset of high energy tunneling transfer between cations. [38, 41, 109]

Moreover, since the fitting analysis is made with only one conducting process being taken into account while in reality more than one conduction processes can exist at certain temperature, the small localization length and the larger fitted exponential dependence $p$ (0.65 vs. 0.5) could be related to the contribution from other conduction processes.

## 4.5 Summary

To summarize, synthesis of epitaxial $NbO_2$ films on (0001) sapphire substrates has been studied by RBTIBD technique. Under investigated growth conditions, film property was found to be sensitive to the $Ar/O_2$ mixture flow rate, which had a direct effect on Nb/O stoichiometry. Meanwhile, substrate temperature played an much less important role in affecting film quality in the studied range (350 °C to 550 °C).

For the film deposited under optimized conditions, no secondary phase was detected by XRD scan or Raman spectrum. The film was highly textured with the only out-of-plane reflection being (110) of tetragonal $NbO_2$, and the epitaxial orientation relationship between the film and substrate was found to be $\langle 001\rangle(110)NbO_2||\langle 10\bar{1}0\rangle(0001)Al_2O_3$. The film also exhibited high crystallinity and smooth surface. The oxidation state of $Nb^{4+}$ was further confirmed by XPS, and the presence of a thin $Nb_2O_5$ layer at film surface was observed due to the exposure to ambient environment. Temperature dependence of con-

ductivity was studied between 180 K and 400 K. Analysis on the measured data suggested that the conduction was dominated by Efros-Shklovskii VRH at lower temperature, while the characteristics at higher temperature can be described by small polaron hopping but needs further confirmation.

# Chapter 5

# Substitutionally alloyed $V_xNb_{1-x}O_2$ films

## 5.1 Introduction

$NbO_2$ forms mixed oxides with a variety of transition metal dioxides, and cation substitution results in modification of structural as well as transport properties. [110–112] Among the transition metals that can be incorporated into $NbO_2$, vanadium is of particular interest due to the similarities between $NbO_2$ and $VO_2$. Being formed by transition metals in the same column of periodic table, $NbO_2$ and $VO_2$ share similarities in many aspects. Both of them have one *d* valence electron that is not engaged in metal-oxygen bonding, and undergo transitions in transport properties as well as crystal structures at certain temperatures. Compared with that of $NbO_2$, the transition of $VO_2$ is more abrupt with larger jump in resistivity (as high as $\sim 10^5$ times in single crystal $VO_2$ vs. $\sim 10^1$ times in $NbO_2$) and occurs at lower temperature (340 K vs. 1081 K). [62, 113] As for lattice structure, both of them adapt distorted rutile structures with metal-metal parings along *c*-axis below transition temperatures.

It has been shown that RBTIBD technique is able to prepare highly pure $NbO_2$ and $VO_2$ thin films. [91, 114] Moreover, the capacity of co-sputtering of this technique allows for exploration of the alloyed $V_xNb_{1-x}O_2$ system. This chapter demonstrates synthesis of (Nb-rich) $V_xNb_{1-x}O_2$ thin films on (0001) sapphire substrates. The approaches of composition

control using RBTIBD technique are explored. The modification effect of V substitution on microstructures and transport properties of $NbO_2$ is discussed.

## 5.2 Experimental

### 5.2.1 Concentration control and estimation

As is introduced in Chapter 3, pulsed DC bias mode of RBTIBD is used for depositions in this study, and sputtering of target material occurs when the target is negatively biased. When co-sputtering more than one targets (up to three), the frequency and positive/negative pulse width of the applied bias to each target are controlled individually. Sputtering rate of target material can be adjusted by tuning the pulse width and/or frequency of applied bias.

Nb and V films were deposited with negative bias current ($I_{Neg}$) being tuned by negative pulse width ($w_{Neg}$) and other conditions remaining constant (listed in Table 5.1). Pulse frequency was fixed at $f$ = 71.43 kHz, which is the frequency used for all depositions of this dissertation work. As is shown by Figure 5.1, growth rates of metal films demonstrated linear dependence on $w_{Neg}$.

| Deposition conditions | Parameter values |
|---|---|
| Substrate temperature (°C) | No heating |
| Process pressure (mTorr) | 0.9 |
| Target potential bias (V) | -900 and +20 |
| DC pulse frequency (kHz) | 71.43 |
| Cathode Ar flow rate (SCCM) | 10 |
| Cathode current (A) | 7 |
| Anode Ar flow rate (SCCM) | 70 |
| Anode current (A) | 6.5 |

Table 5.1: Deposition condition parameters for growth rate calibration of Nb and V films.

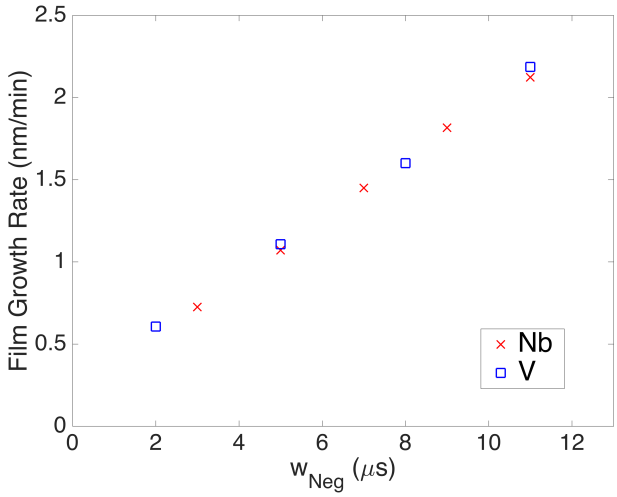


Figure 5.1: Dependence of Nb and V film growth rates on $w_{Neg}$ at pulse frequency $f$ = 71.43 kHz.

For the synthesis of alloyed films in this chapter, Nb and V target were both biased during deposition, with fixed pulse frequency and different $w_{Neg}$. Growth rates calibrated in Figure 5.1 were used as indicators of target sputtering rates, which were used to estimate the V content in chamber ($V\%_{ch}$).

$$V\%_{ch} = \frac{GR_V}{GR_V + GR_{Nb}} \tag{5.1}$$

where $GR$ is the growth rate of metal film (in nm/min) at certain target bias conditions (calibrated in Figure 5.1).

Growth of both $NbO_2$ and $VO_2$ films on (0001) sapphire substrates has been explored by RBTIBD. It is found that films with high purity of tetragonal $NbO_2$ phase and monoclinic $VO_2$ phase could be obtained under similar deposition conditions. As is shown by Figure 5.2, being deposited under growth conditions listed in Table 5.2, both $NbO_2$ and $VO_2$ films are highly textured, with the out-of-plane orientations being (440) of tetragonal $NbO_2$ and (020) of monoclinic $VO_2$, respectively. The growth rate of $NbO_2$ film ($\sim$ 3.3 nm/min) is about 4 times of the growth rate of $VO_2$ film ($\sim$ 0.8 nm/min).

| Deposition conditions | Parameter values |
|---|---|
| Substrate temperature (°C) | 450 |
| Process pressure (mTorr) | 0.9 |
| $Ar/O_2$ mix flow rate (SCCM) | 6 |
| Target potential bias (V) | -900 and +20 |
| DC pulse frequency (kHz) | 71.43 |
| Positive duty cycle ($\mu$s) | 3 |
| Cathode Ar flow rate (SCCM) | 10 |
| Cathode current (A) | 7 |
| Anode Ar flow rate (SCCM) | 70 |
| Anode current (A) | 6.5 |

Table 5.2: Deposition condition parameters for $NbO_2$ and $VO_2$ films on sapphire (0001) substrates.

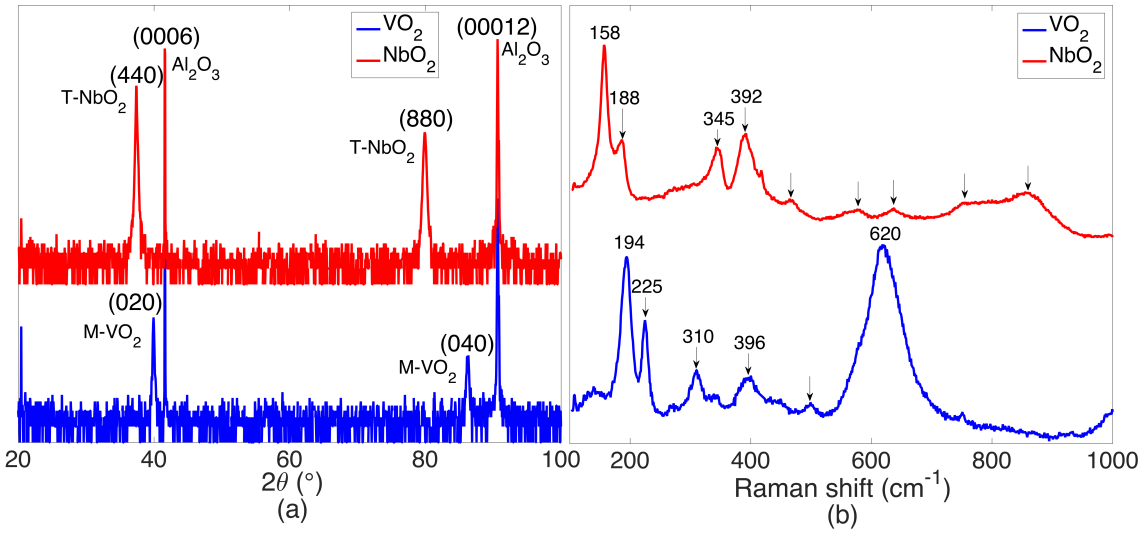


Figure 5.2: (a) 2θ-ω scans and (b) Raman spectra of $NbO_2$ and $VO_2$ films on (0001) sapphire substrates.

The growth rates of $NbO_2$ and $VO_2$ films are compared in another way by considering the rates of incorporating metal into the films

$$\frac{r_{NbO_2}}{r_{VO_2}} = \frac{GR_{NbO_2} \cdot N_{NbO_2} \cdot V_{UC,VO_2}}{GR_{VO_2} \cdot N_{VO_2} \cdot V_{UC,NbO2}} \tag{5.2}$$

where $GR$ is the film growth rate in nm/min, $N$ is the number of formulas in the unit cell

(32 for $NbO_2$ and 4 for $VO_2$), $V_{UC}$ is the volume of the unit cell (1122 $\AA^3$ for $NbO_2$ and 118 $\AA^3$ for $VO_2$). The ratio is calculated to be $\sim 3.4$.

To assist the understanding on synthesis process, two parameters characterizing the V content are defined. One is the V content in chamber ($V\%_{ch}$) defined by Eq. 5.1, the other is the estimated V content in deposited film ($V\%_{fe}$), defined by taking the ratio calculated by Eq. 5.2 as a correction factor.

$$V\%_{fe} = \frac{GR_V}{GR_V + GR_{Nb} \times 3.4} \tag{5.3}$$

### 5.2.2 Film growth

To obtain $V_xNb_{1-x}O_2$ films with variation in concentration of V, films were deposited with sputtering rate of Nb and V targets being tuned by pulse width while keeping pulse frequency fixed at 71.43 kHz. During the deposition, sputtering rate of Nb target was fixed, while sputtering rate of V target was varied by the pulse width. Deposition conditions are listed in Table 5.3. (Approach of keeping the total sputtering rate of two targets constant and varying the sputtering rates of both Nb and V targets was also tested, which resulted in films containing over-oxidized phases.)

| Deposition conditions | S1 | S2 | S3 | S4 | S5 |
|---|---|---|---|---|---|
| Ar/$O_2$ Mix Flow Rate (SCCM) | 6 | 6 | 6 | 6 | 6 |
| Process Pressure (mTorr) | 0.85 | 0.85 | 0.83 | 0.84 | 0.83 |
| Substrate Temperature (°C) | 450 | 450 | 450 | 450 | 450 |
| DC Pulse Frequency to Nb Target (kHz) | 71.43 | 71.43 | 71.43 | 71.43 | 71.43 |
| Positive Duty Cycle to Nb target ($\mu$s) | 3 | 3 | 3 | 3 | 3 |
| Negative Duty Cycle to Nb target ($\mu$s) | 11 | 11 | 11 | 11 | 11 |
| DC Pulse Frequency to V Target (kHz) | — | 71.43 | 71.43 | 71.43 | 71.43 |
| Positive Duty Cycle to V target ($\mu$s) | — | 12 | 9 | 6 | 3 |
| Negative Duty Cycle to V target ($\mu$s) | — | 2 | 5 | 8 | 11 |
| Positive Target Bias (V) | 20 | 20 | 20 | 20 | 20 |
| Negative Target Bias (V) | 900 | 900 | 900 | 900 | 900 |
| Cathode Ar Flow Rate (SCCM) | 10 | 10 | 10 | 10 | 10 |
| Cathode Current (A) | 7 | 7 | 7 | 7 | 7 |
| Anode Ar Flow Rate (SCCM) | 70 | 70 | 70 | 70 | 70 |
| Anode Current (A) | 6.7 | 6.7 | 6.7 | 6.7 | 6.7 |

Table 5.3: Deposition condition parameters of $V_xNb_{1-x}O_2$ films with variation in V concentration.

All films were deposited for 30 min. Film thickness was measured by XRR, and real V content ($V\%_{fr}$) was characterized using Rutherford backscattering (RBS) by collaborators Ryan. B. Comes and Tamara F Isaace-Smith from Auburn University. These two parameters are listed in Table 5.4, together with the V content in chamber $V\%_{ch}$ and estimated V content in film $V\%_{fe}$, calculated by Eq. 5.1 and Eq. 5.3, respectively.

| Sample | S1 | S2 | S3 | S4 | S5 |
|---|---|---|---|---|---|
| Film thickness (nm) | 106.5 | 107.3 | 113.9 | 141.5 | 197.2 |
| $V\%_{ch}$ | 0% | 21.4% | 34.0% | 43.0% | 49.7% |
| $V\%_{fe}$ | 0% | 7.2% | 13.3% | 18.2% | 22.5% |
| $V\%_{fr}$ | 0% | 5.6% | 8% | 27% | 45% |

Table 5.4: Film thickness and V concentration of $V_xNb_{1-x}O_2$ films. ($V\%_{fr}$: Courtesy of Ryan. B. Comes and Tamara F Isaace-Smith from Auburn University.)

## 5.3 Structural properties of $V_xNb_{1-x}O_2$ films

Due to the instability of $4d$ electrons of Nb compared to the $3d$ electron sof V, it is possible that the following reaction occurs when V is incorporated into $NbO_2$ film, which was proposed in some early studies on bulk $V_xNb_{1-x}O_2$ (polycrystalline samples). [115–117]

$$Nb^{4+} + V^{4+} = Nb^{5+} + V^{3+} \tag{5.4}$$

As is shown by Table 5.5, the sizes of $Nb^{5+}$ and $V^{3+}$ ions are closer to that of $Nb^{4+}$ ions. Therefore formation of $Nb^{5+}$ and $V^{3+}$ will results in smaller local lattice distortion than $V^{4+}$ and more favorable if only considering the size effect.

| | Charge | Coordination | Ionic radius (Å) |
|---|---|---|---|
| Nb | 4 | 6 | 0.68 |
| | 5 | 6 | 0.64 |
| V | 4 | 6 | 0.58 |
| | 3 | 6 | 0.64 |

Table 5.5: Ion sizes of Nb and V. [103]

### 5.3.1 Phase composition

Raman spectra of the $V_xNb_{1-x}O_2$ films were measured between 100 $cm^{-1}$ and 1000 $cm^{-1}$, which are plotted in Figure 5.3. Raman spectrum of pure $VO_2$ films is also included in the figure for reference. With the increase of V content, the observed variation of the Raman features includes continuous depression of peaks around 158 $cm^{-1}$ and 187 $cm^{-1}$, strengthening of the peak around 765 $cm^{-1}$, and shifts of bands near 345 $cm^{-1}$ and 392 $cm^{-1}$ (as shown in Figure 5.3 (b)).

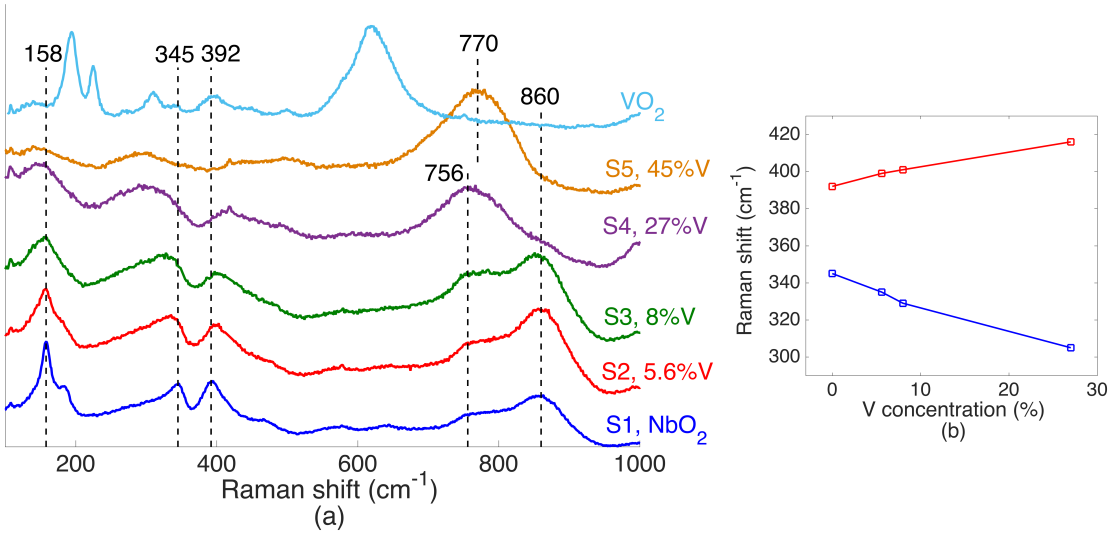


Figure 5.3: (a) Raman spectra of $V_xNb_{1-x}O_2$ films with different V concentration; (b) Raman shifts (of the bands near 345 $cm^{-1}$ and 392 $cm^{-1}$) as functions of V concentration (for samples S1-S4).

Since studies on Raman spectrum of $NbO_2$ films are still limited, lattice structure and Raman spectrum of $NbO_2$ are compared with those of $VO_2$ to understand the observed variation in Raman features. Both dioxides adapt distorted rutile structures with $MO_6$ octahedra linked together and metal ions paired along *c*-axis. The reported Raman spectra of $NbO_2$ and $VO_2$ films share many similar features. [27, 118]

For $VO_2$, there are two groups of Raman bands the assignment of which to the vibration modes are generally accepted. One is the Raman bands at low frequencies (refer to bands at 194 $cm^{-1}$ and 225 $cm^{-1}$ in Figure 5.2 (b)), which are assigned to the V ion motions in the dimerized chains. The other is the band at $\sim$ 620 $cm^{-1}$, which is ascribed to the symmetric stretching mode of the basal oxygen ions within the $VO_6$ octahedra. [119, 120]

Taking into account the larger size of Nb ions and longer Nb-Nb distances, it is deduced that the Raman bands at low frequency (158 $cm^{-1}$ and 187 $cm^{-1}$) are related to the Nb-Nb motions in Nb chains. Along this line of reasoning, the suppression of these two Raman bands corresponds to the dissociation of Nb-Nb bonds and symmetry breaking due to the V

substitution, indicating a transition from the distorted rutile lattice to the basic rutile lattice as V concentration increased.

Studies on Raman scattering of various niobium oxides demonstrates that the Raman bands at high frequencies can be assigned to the internal modes of the $NbO_6$ octahedra. [121, 122] Due to the large binding forces, the internal vibration modes within $NbO_6$ occur at much higher frequencies than the external modes, being close to the free-ion modes. Among the various Raman modes, the one corresponding to the symmetric Nb-O stretching is the most diagnostic one in oxide systems, which is found to be sensitive to the ordering and had low or no intensity in disordered systems. [121] This Nb-O stretching band has frequencies between 700 $cm^{-1}$ - 1000 $cm^{-1}$, and the variation in frequency is related to the different length of Nb-O bands in edge-sharing or corner-sharing $NbO_6$. However, study or analysis on the frequency of this mode in $NbO_2$ was not found. As a reference, B-$Nb_2O_5$ also consists of chains of $NbO_6$ octahedra and the Nb-O distances in B-$Nb_2O_5$ are close to those in $NbO_2$ (1.8 $\AA$ - 2.2 $\AA$ for B-$Nb_2O_5$ [121] vs. 1.91 $\AA$ - 2.25 $\AA$ for $NbO_2$ [16, 19]). The Nb-O stretching Raman band of B-$Nb_2O_5$ exhibits frequency of 760 $cm^{-1}$. Therefore the Raman bands between 750 $cm^{-1}$ - 900 $cm^{-1}$ in the measured Raman spectra are ascribed to the Nb-O vibration modes within the $NbO_6$ octahedra. Since it has been suggested by the bands at low frequency that the lattice distortion of tetragonal $NbO_2$ decreases with the increase of V content, the changes in Raman features within this frequency range could be attributed to more identical metal-oxygen bond lengths within the octahedra and changes in metal-oxygen interaction strength.

As has been discussed in Chapter 4, Raman bands near 345 $cm^{-1}$ and 392 $cm^{-1}$ are likely related to different bending modes of Nb-O vibration within $NbO_6$ octahedra. Therefore shifts of Raman bands could result from changes in metal-oxygen bond lengths or interatomic force constants caused by V substitution.

### 5.3.2 Microstructures

Figure 5.4 (a) shows X-ray 2θ-ω scans on $V_xNb_{1-x}O_2$ samples in a wide range from 20° to 100°. For all samples, 2θ-ω scans demonstrate two diffraction peaks from film, with the 2θ positions being close to (440) and (880) diffractions of tetragonal $NbO_2$ or (200) and (400) diffractions of rutile $NbO_2$. Examples of X-ray ϕ scans at 2θ = 26° and χ = 45°, which correspond to (440) of tetragonal $NbO_2$ or (110) of rutile $NbO_2$, are shown in Figure 5.4 (b) and (c) for samples S4 and S5, respectively. Combining with ϕ scans of $(01\bar{1}2)$ sapphire diffraction peaks, the orientation relation between film and substrate can be expressed as $\langle 001\rangle(110)V_xNb_{1-x}O_2(T)||\langle 10\bar{1}0\rangle(0001)Al_2O_3$ or $\langle 001\rangle(100)V_xNb_{1-x}O_2(R)||\langle 10\bar{1}0\rangle(0001)Al_2O_3$.

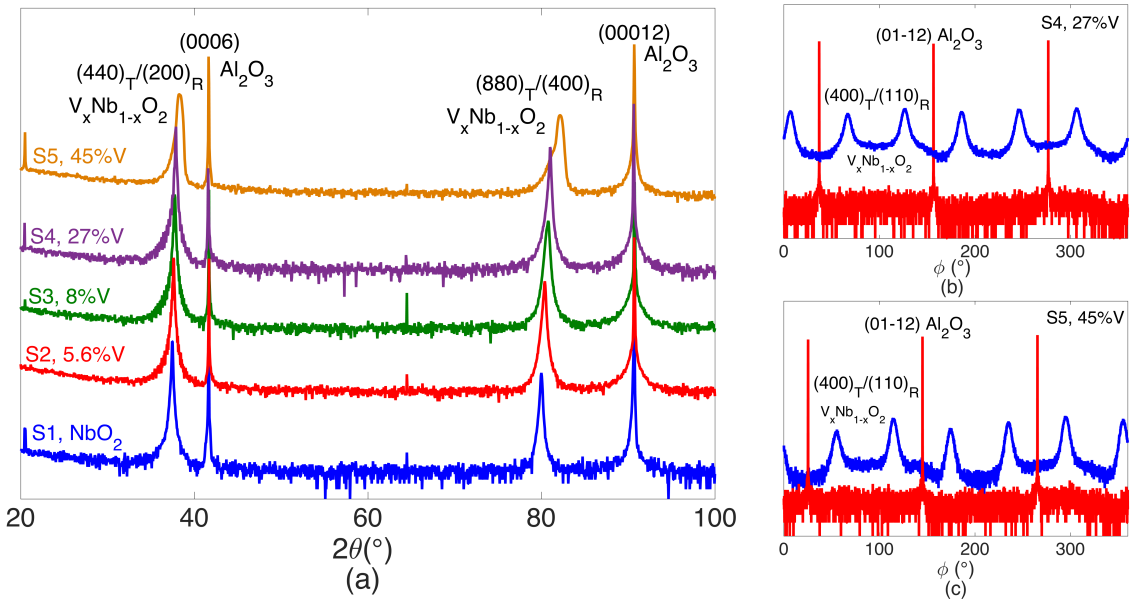


Figure 5.4: (a) 2θ-ω scans from 20° to 100° of $V_xNb_{1-x}O_2$ samples with different V concentration; In-plane ϕ scans of (b) sample S4 (27%V) and (c) sample S5 (45%V), including diffraction peaks (blue) obtained at 2θ = 26° and χ = 45° which correspond to (440) of tetragonal $NbO_2$ or (110) of rutile $NbO_2$, and diffraction peaks (red) obtained at 2θ = 25.5° and χ = 12.8° which correspond to $(01\bar{1}2)$ of sapphire substrate.

For more precise characterization, X-ray 2θ-ω scans were performed from 35° to 43°

with a finer step (0.01°). As is shown by Figure 5.5 (a), except for S5 with 45%V, scans on all other samples demonstrate clear Kiessig fringes, indicating high crystallinity and homogeneity of these four samples.

The shoulder of X-ray 2θ-ω profile of S5 was further investigated by conducting reciprocal space mapping (RMS) on the $(440)_T/(200)_R$ reflection, which is shown by Figure 5.5 (b). Since there is only one peak spreading along $Qx$ axis, it is not likely that there are two separated diffraction peaks. The shoulder of XRD profile could be an indicator of variation in lattice parameter due to uneven strain or variation in oxygen content.

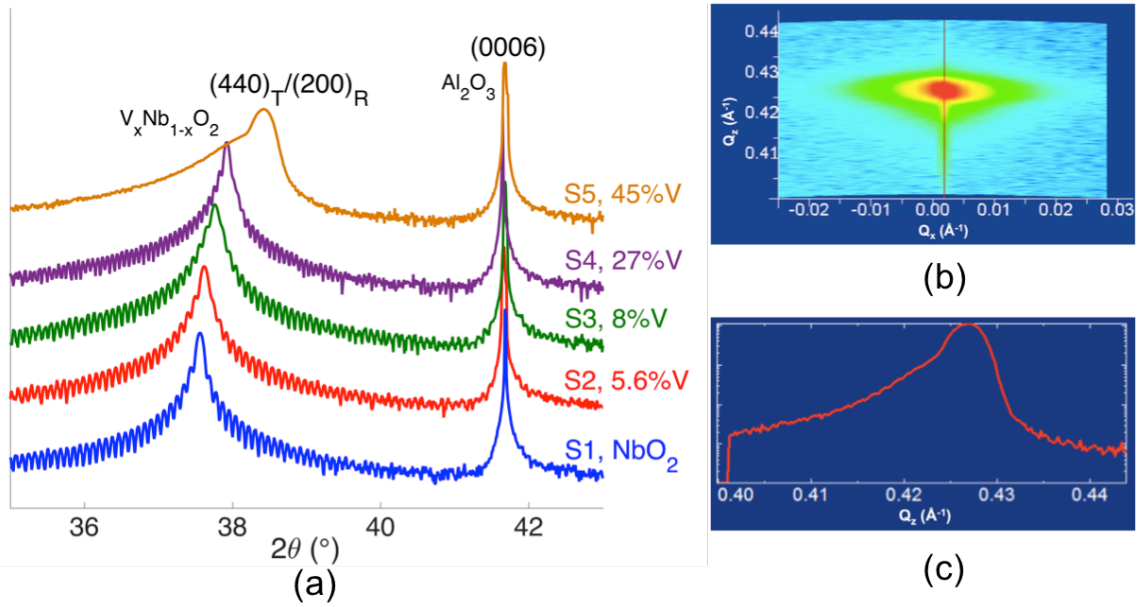


Figure 5.5: (a) 2θ-ω scans from 35° to 43° of $V_xNb_{1-x}O_2$ samples with different V concentration; (b) RMS on reflection peak at 2θ ∼ 38° of sample S5 (45%V); (c) Cut line profile corresponding to the line in (b).

With the increase of V content, diffraction peaks of films shift to larger 2θ values, corresponding to a decrease in lattice constant. Lattice constants are extracted from profiles in Figure 5.5 (a) and plotted as a function of V concentration in Figure 5.6. (440) diffraction of tetragonal $NbO_2$ lattice corresponds to the (200) diffraction of the basic rutile lattice. For pure $NbO_2$, the lattice constant of tetragonal phase ($a_T$ = 13.702 $\AA$) is very close

to the value calculated by the relations between the tetragonal unit cell and rutile unit cell ($a_T \cong 2\sqrt{2}a_R = 2\sqrt{2}\cdot 4.846\ \AA = 13.706\ \AA$). Therefore the lattice distortion at phase transition does not cause much change along $a$-axis. Lattice parameter $a$ of the rutile lattice ($a_R$) is calculated and compared for all samples. As is shown by Figure 5.6, $a_R$ of $V_xNb_{1-x}O_2$ films decreases monotonically with the increase of V concentration, which could be attributed to the smaller sizes of $V^{4+}$ ions (or $Nb^{5+}$ and $V^{3+}$ ions).

Moreover, $a_R$ of pure $VO_2$ is also included in Figure 5.6, which is estimated according to the structural transition relation $a_R \approx b_M$. [123] Considering the lattice distortion upon transition ($a_R = 4.555\ \AA$ and $b_M = 4.538\ \AA$ for bulk $VO_2$ [124]), the lattice parameter of deposited monoclinic $VO_2$ film is corrected by factor $r = a_R(\text{Bulk } VO_2)/b_M(\text{Bulk } VO_2)$. The black straight line represents fitting of $a_R$ values of pure $NbO_2$ and $VO_2$ to Vegard's law as a reference.

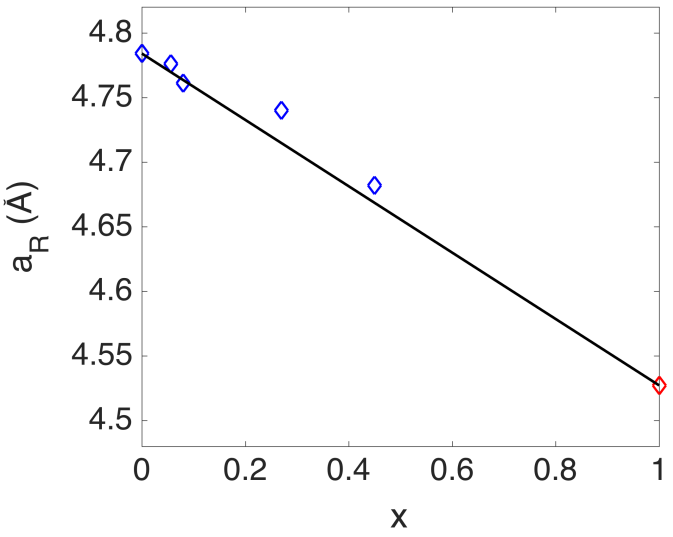


Figure 5.6: Variation of lattice constant $a_R$ with V concentration, the solid line of Vegard's law is determined by lattice parameters of pure $NbO_2$ and $VO_2$.

### 5.3.3 Surface morphology

Surface morphology of $V_xNb_{1-x}O_2$ films was characterized by AFM. Surface roughness RMS obtained from the 1 $\mu$m $\times$ 1 $\mu$m images are listed in Table 5.6.

| Sample | S1 | S2 | S3 | S4 | S5 |
|---|---|---|---|---|---|
| RSM (nm) | 0.34 | 0.19 | 0.30 | 0.24 | 1.41 |

Table 5.6: Surface roughness of $V_xNb_{1-x}O_2$ films with different V concentration.

For sample with low V content (S2 with 5.6% V and S3 with 8% V), film surface is smooth and the morphology is similar to that of pure $NbO_2$, as is shown by the comparison of 1 $\mu$m $\times$ 1 $\mu$m images in Figure 5.7. Combining with the observation of Nb-Nb vibration features in Raman spectra, it is deduced that for these two samples the film lattice still maintains the same distorted rutile structure as tetragonal $NbO_2$.

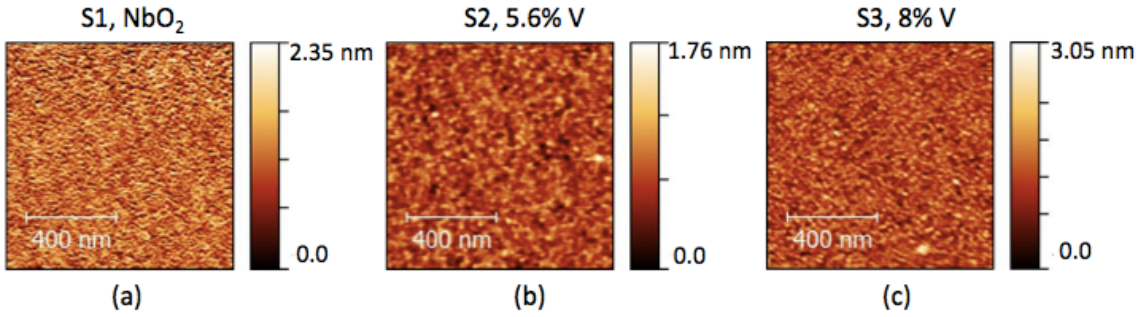


Figure 5.7: AFM images of selected $V_xNb_{1-x}O_2$ films with different V concentration (S1 to S3).

For S4, while the film surface still shows similar morphology, small islands with $\sim$ 2 nm heights start to show up as is shown by Figure 5.8 (a), indicating formation of a new phase. Taking into account the homogeneity indicated by the X-ray 2$\theta$-$\omega$ scan of S4, the amount of formed new phase should be small. With further increase of V concentration, for S5 the surface morphology is distinct from those of the other four samples. Comparing the surface profiles along the white lines labeled in the images of these two samples, it is found

that the grain sizes and heights are close. The variation from S4 to S5 can be explained by formation of a new phase with the increase of V content in the films. Combining with the measured Raman spectra, the new phase could be $V_xNb_{1-x}O_2$ with regular rutile lattice.

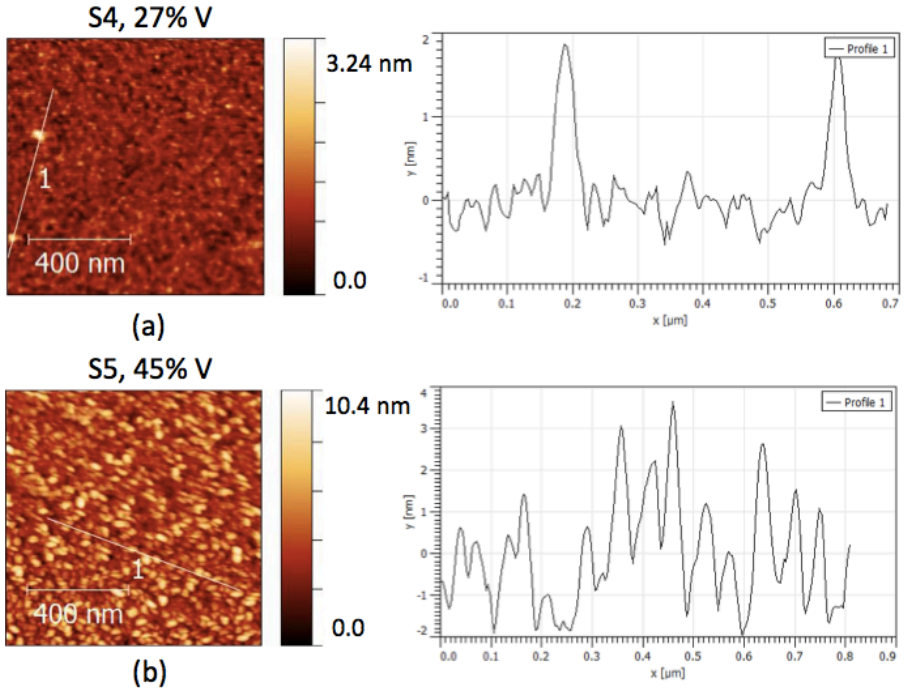


Figure 5.8: AFM images and line scans of $V_xNb_{1-x}O_2$ samples (a) S4 and (b) S5.

Summarizing briefly, characterization of structural properties of the $V_xNb_{1-x}O_2$ films suggests that the substitution of V ions break the Nb-Nb bonds along *c*-axis. With the increase of V content, the lattice distortion decreases and finally the superstructure of tetragonal $NbO_2$ collapses into the regular rutile structure.

The comparison of V content values obtained by different methods listed in Table 5.4 also provides some information on the growth mechanism and phase composition of the films. For S2 and S3 with relatively low V concentration, the film still adapts the distorted rutile structure of tetragonal $NbO_2$. The film growth rates are close to that of pure $NbO_2$ and real V concentration values ($V\%_{fr}$) are close to those estimated from the growth rates of distorted rutile phases ($V\%_{fe}$). The real V content in film is much lower than the

V concentration in chamber ($V\%_{ch}$), which indicates the difficulty of V substitution into tetragonal $NbO_2$ lattice due to repulsion from size effect and breaking of tetragonal symmetry. For S5 when the concentration of V ions in chamber is about 50%, the real V content in film is close to the V concentration in chamber, which is much higher than the value estimated based on growth rates of distorted rutile phases. This can be understood as an indicator of the formation of a different phase (regular rutile phase), for which Nb and V ions are incorporated at similar rates. As for S4, the real V content is between the V content in chamber and estimated V content in film. It is speculated that the distorted rutile lattice is not yet completely destroyed in the film, and the film still contains short-range ordering of the tetragonal $NbO_2$ lattice. This hypothesis agrees with the observed features of Raman spectrum and AFM image of S4.

## 5.4 Transport properties of $V_xNb_{1-x}O_2$ films

Film conductivity as a function of temperature has been measured between 150 K and 400 K, which is shown by the Arrhenius plots in Figure 5.9 (a). For S1 and S2, sample resistance exceeded compliance of VersaLab system near 150 K and film conductivity data was not available. With the increase of V content, film conductivity increased monotonically. Activation energy determined by Arrhenius fitting is plotted as a function of V concentration in Figure 5.9 (b).

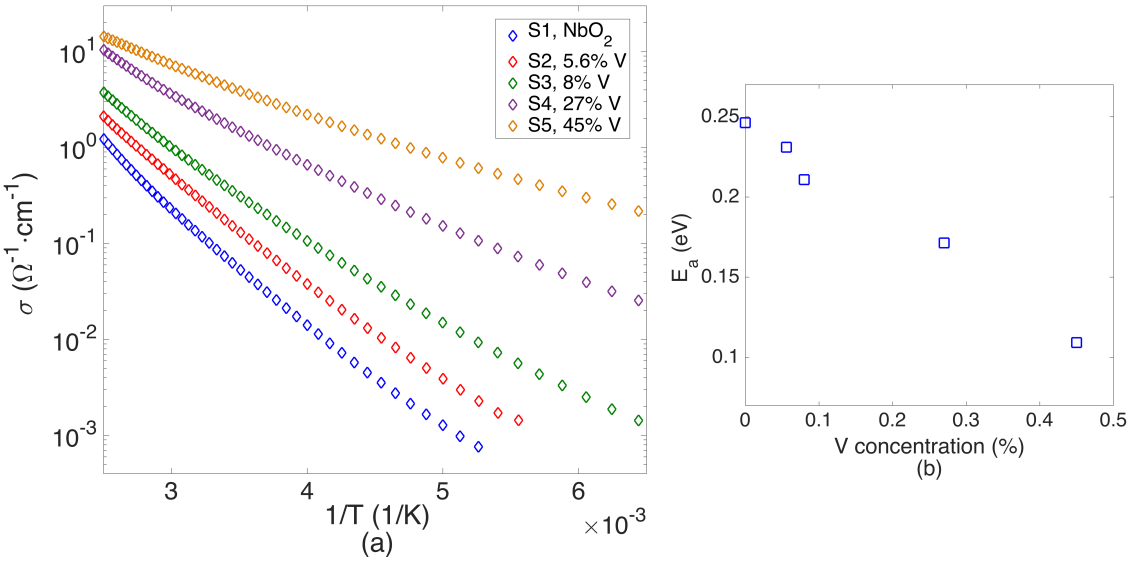


Figure 5.9: (a) Arrhenius plots of film conductivity of $V_xNb_{1-x}O_2$ samples; (b) Activation energy as a function of V concentration .

Based on the structural characterization, the tetragonal symmetry resulted from the Nb-Nb dimers is still maintained in sample S1, S2 and S3. With the increase of V content, film lattice of the three samples become increasingly (long-range) disordered due to the dissociation of Nb-Nb pairs. While the splitting feature of $d_{||}$ bands can still be maintained by the short-range ordering of Nb-Nb bonds, the amount of band tail states beyond the mobility edge might increase due to the disordering. Moreover, possible formation of $Nb^{5+}$ and $V^{3+}$ could result in donor (related to $V^{3+}$) and acceptor (related to $Nb^{5+}$) states within the band gap. Both effects could result in decrease of activation energy of conduction (with the increase of V concentration), which is demonstrated by the plots of these three samples.

For the other two samples (S4 and S5) with much higher V concentration, the tetragonal symmetry is depressed significantly, and lattice adapts regular rutile structure partially or completely. Thanks to the low resistance of these two samples, temperature dependence of Seebeck coefficient $S$ was able to be measured. (Data on other samples were not available due to the large sample resistance, which was beyond the capacity range of the thermal

transport option of PPMS.) As is shown by Figure 5.10 (a), Seebeck coefficients of these two samples demonstrated different temperature dependent characteristics. For S4, the magnitude of $S$ increases with the decrease of temperature above $\sim$ 300 K, and the fitting to Eq. 2.10 to determine the activation energy is shown in the inset. For S4 at lower temperature and S5 within the whole investigated temperature range, the magnitude of $S$ increases with temperature, which agrees with the characteristics of $S$ for variable range hopping among states near Fermi level.

Figure 5.10 (b) shows the temperature-dependent conductivity of the two samples plotted and fitted according to the Efros-Shklovskii VRH model. The conductivity data of S5 can be reproduced by the linear fitting very well within the whole temperature range while deviation from linear fitting is observed for S4 above $\sim$ 300 K, which agrees with what had been suggested by temperature dependence of $S$. The dominance of variable range hopping indicates that states in bands are localized. The localization can result from the randomness caused by cation substitution and increased electron-electron correlation due to stronger Coulomb interaction of V 3$d$ electrons. On the other hand, $Ar/O_2$ 80/20 mixture flow rate was kept constant for depositions of all samples, oxygen-deficient defects are also possible to result in conductivity increase, therefore the effect of non-stoichiometry needs to be investigated systematically.

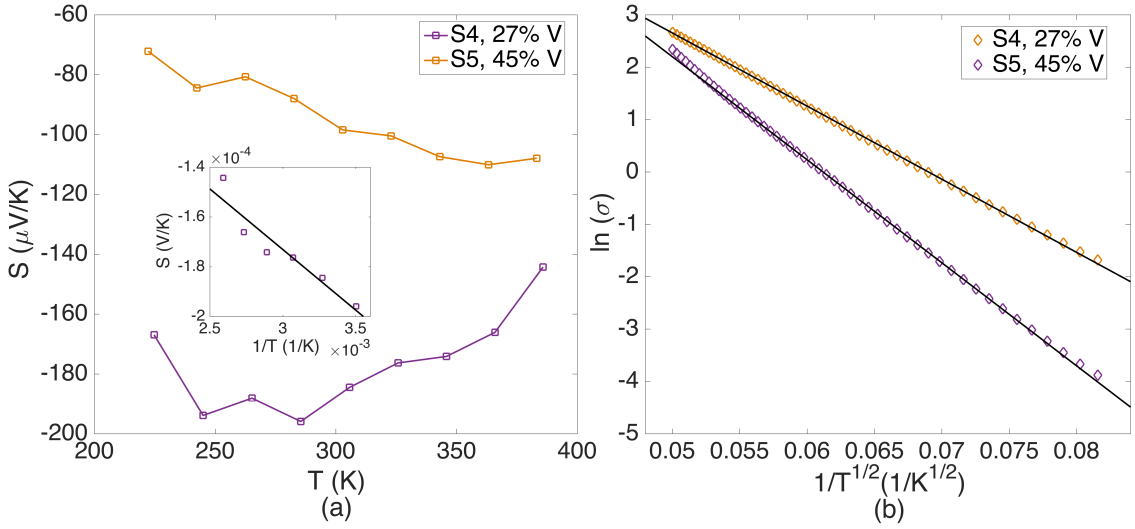


Figure 5.10: (a) Temperature dependence of Seebeck coefficient $S$ and (b) Plots of Efros-Shklovskii VRH and corresponding fitting of sample S4 and S5.

## 5.5 Summary

To summarize, substitutionally alloyed Nb-rich $V_xNb_{1-x}O_2$ films has been deposited on (0001) sapphire substrates, and modification effect of V substitution on structural and transport properties has been characterized. Nb and V targets were co-sputtered at same pulse frequency during the deposition, and the Nb/V ratio was varied by changing the sputtering rate of V target through pulse width while keeping the sputtering rate of Nb target constant. Structural characterization indicated that with the increase of V content, Nb-Nb bonds dissociated, leading to the gradual disappear of tetragonal symmetry (distortion of rutile lattice). V substitution also led to increase of film conductivity, which was possibly due to collapse of $d_{||}$ band splitting and formation of localized defect states within band gap. However, further study is needed to separate the effect of oxygen stoichiometry before more conclusion can be made.

From the samples investigated in this chapter, it can be concluded that with V concen-

tration below 8%, the distorted rutile lattice of tetragonal $NbO_2$ could still be maintained. With further increase of V content, the dominating phase in deposited films transited from tetragonal phase to rutile phase, resulting in change in the incorporation rate of V. There was a large concentration gap between S3 (8% V) and S4 (27% V), with detailed information on the properties variation missing. Therefore further study with finer steps of concentration variation is needed.

# Chapter 6

# MIT under electric field

## 6.1 Introduction

MIT of $NbO_2$ under electric field, which occurs as a rapid and reversible switching between a high resistance state and a low resistance state controlled by applied electric field, has received increasing attention in recent years. This property has potential application in selecting devices in resistive random access memories (ReRAM) to minimize the sneak leakage current, and the high transition temperature of thermally induced MIT (1081 K) makes $NbO_2$ more appealing in circuit application. [12–15] The capacity of synthesizing high quality $NbO_2$ films by RBTIBD has been demonstrated in Chapter 4. In this Chapter, MIT under electric field in devices based on the synthesized $NbO_2$ films, both at room temperature and elevated temperatures, has been studied. Being aware of the spontaneous formation of $Nb_2O_5$ at film surface, devices are designed to minimize the existence of $Nb_2O_5$, and possible effect of $Nb_2O_5$ are investigated.

## 6.2 $NbO_2$-based vertical devices

Characterization of MIT under electric field was performed by running voltage or current sweeps through the $NbO_2$ film vertically. Structures of the investigated vertical devices

and fabrication process are described in Chapter 3. The conducting TiN layer which was pre-coated on the (100) Si substrate served as the bottom. The Nb layer which was fabricated into the top electrodes was deposited on $NbO_2$ film prior to air exposure, to prevent the spontaneous formation of $Nb_2O_5$. To better understand the effect caused by the existence of $Nb_2O_5$, measurements were also conducted by probing the tungsten tip directly on the uncovered $NbO_2$ film. Comparison of these two structures is illustrated in Figure 6.1. In the investigated devices, the thickness of the pre-coated TiN film, deposited $NbO_2$ film and Nb film were $\sim$ 57 nm, $\sim$ 104 nm, and $\sim$ 100 nm, respectively.

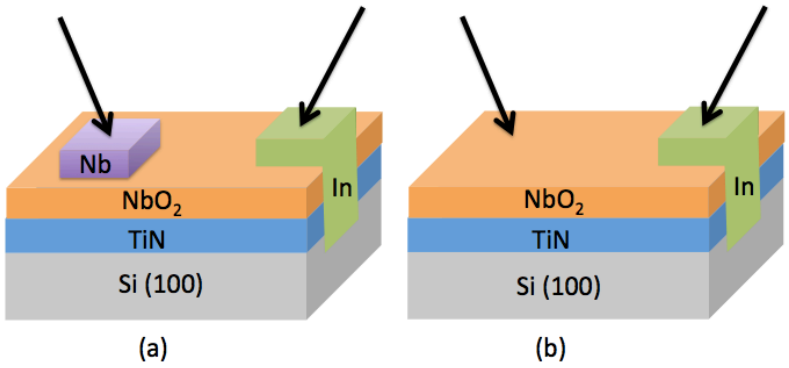


Figure 6.1: Schematic illustration of (a) Nb/$NbO_2$/TiN vertical device and (b) tip/$NbO_2$/TiN vertical device.

$NbO_2$ thin film in the vertical devices was deposited under conditions listed in Table 6.1. $NbO_2$ film deposited on TiN/Si(100) under this condition without Nb cap was characterized by XRD, Raman and XPS to check the quality of the film (Figure 6.2). As shown in Figure 6.2 (a) and (b), in XRD 2θ-ω scan only diffraction peaks from tetragonal $NbO_2$ are observed besides the peaks from substrate, and the Raman spectrum does not show any Raman shifts corresponding to other sub-oxides of Nb [24, 27], indicating predominant existence of $NbO_2$ phase. Core level Nb 3*d* spectra were measured (by Ryan B. Come at Pacific Northwest Laboratory) and analyzed in the same way as for the $NbO_2$ film on sapphire substrate described in Chapter 4. Figure 6.2 (c) shows the spectrum measured

with the photoelectron emission normal to the film surface. The primary peaks correspond to $Nb^{5+}$ and $Nb^{4+}$, and no $Nb^{2+}$ peaks are observed. Figure 6.2 (d) shows the comparison between the spectra obtained with photoelectron emission coming at normal angle (90°) and with a grazing angle (20°). The $Nb^{4+}$ peaks are considerably depressed in the spectrum measured with a grazing angle, indicating that the film surface was over oxidized to $Nb^{5+}$ state and therefore intensity of $Nb^{4+}$ state should be significantly higher in the bulk of the film.

| Deposition conditions | Parameter values |
|---|---|
| Substrate temperature | 500 °C |
| Process pressure | $1.3 \times 10^{-3}$ Torr |
| $Ar/O_2$ mix flow rate | 5.5 SCCM |
| Target potential bias | -900 V and +20 V |
| DC pulse frequency | 71.43 KHz |
| Positive duty cycle | 3 $\mu$s |
| Cathode Ar flow rate and current | 10 SCCM and 7A |
| Anode Ar flow rate and current | 70 SCCM and 6.5 A |

Table 6.1: Deposition conditions of $NbO_2$ on TiN/Si(100) substrate.

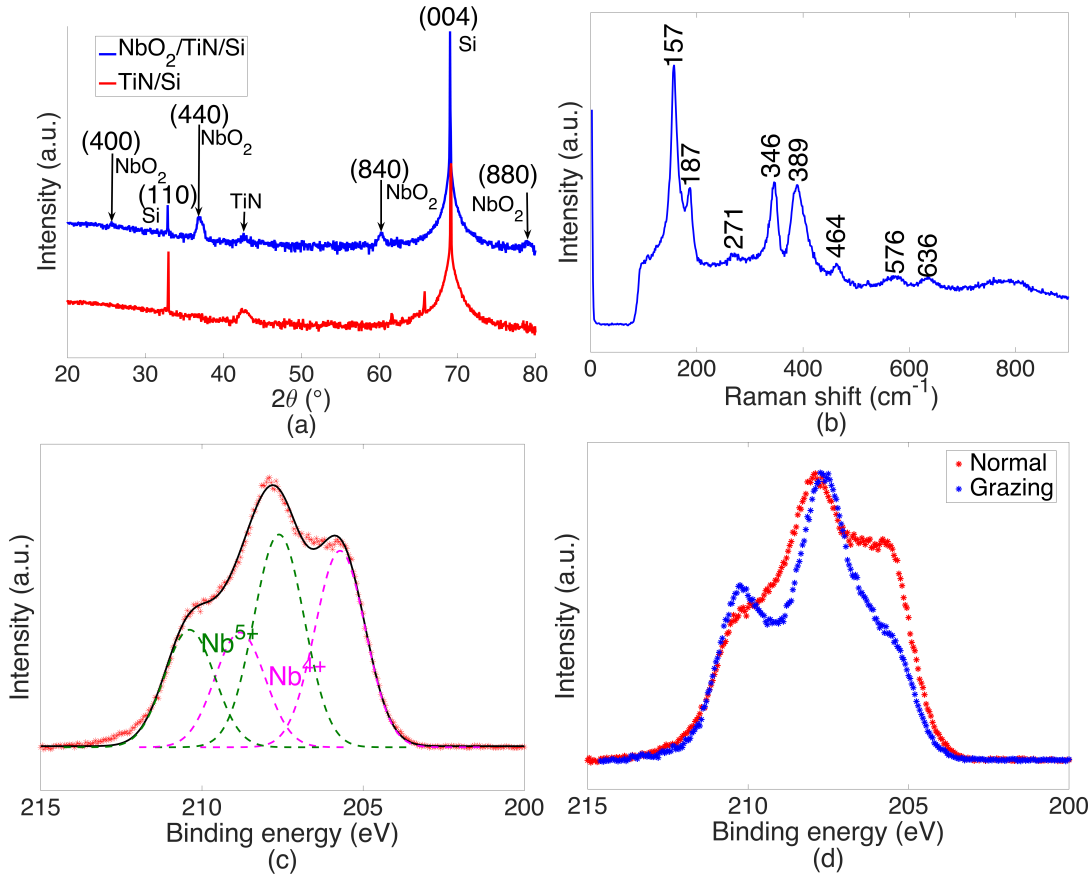


Figure 6.2: (a) XRD 2θ-ω scans of $NbO_2$ films deposited on TiN/Si(100) substrate (top) and TiN/Si(100) substrate (bottom); (b) Raman spectrum of $NbO_2$ film excited by a 514 nm light. (c) Core level Nb 3*d* spectrum of $NbO_2$ film with normal photoelectron incidence; (d) Normalized core level Nb 3*d* spectra of $NbO_2$ film obtained at incident angle 90° (Normal) Vs 20° (Grazing). ((c) and (d): Courtesy of Ryan B. Comes from Pacific Northwest National Laboratory.)

## 6.3 MIT characteristics under electric field

### 6.3.1 Unipolar threshold switching characteristics

At room temperature, pulsed voltage and current sweeps were conducted under both polarities of electric bias. It is defined that current flows from top electrode (Nb) to the bottom electrode (TiN) for positive bias and the opposite way for negative bias.

Figure 6.3 (a) shows typical current-voltage (I-V) characteristics of a Nb/$NbO_2$/TiN vertical device during voltage sweeps. The dimension of top electrode of the measured device is 30 $\mu$m $\times$ 50 $\mu$m.

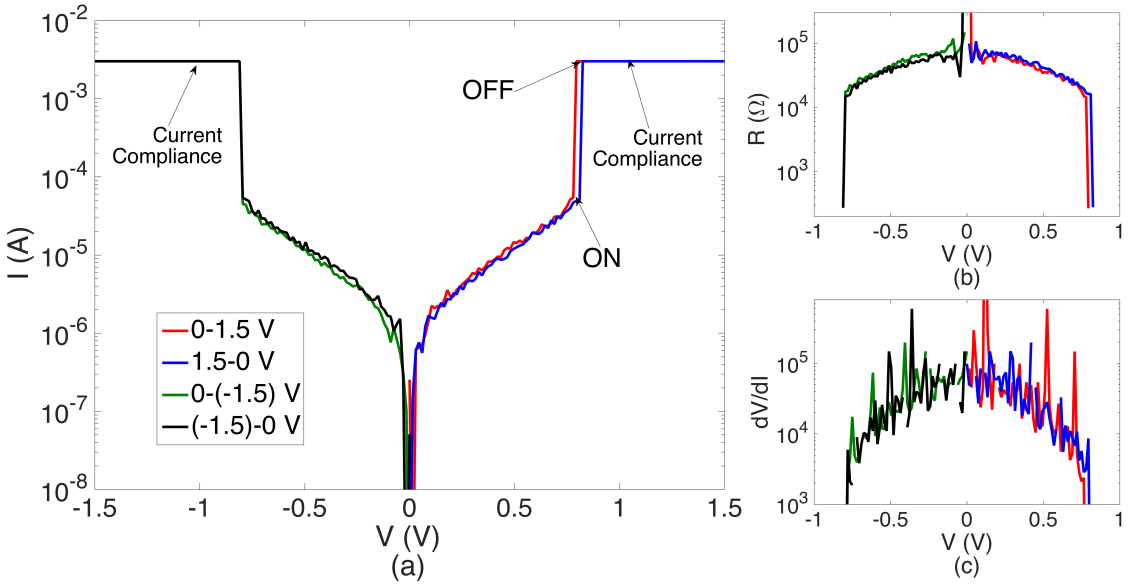


Figure 6.3: (a) Current-voltage (I-V) characteristics of a 30 $\mu$m $\times$ 50 $\mu$m Nb/$NbO_2$/TiN device; Corresponding (b) resistance-voltage (R-V) and (c) $d$V/$d$I-voltage ($d$V/$d$I-V) characteristics, data beyond $V_{Threshold}$ not available because current hit the compliance.

During the upward voltage sweep, current through the device underwent a sudden jump from $\sim$ 0.055 mA to the preset compliance value (3 mA) at a threshold voltage ($V_{Threshold}$) of $\sim$ 0.78 V, corresponding to a drop in resistance from 1.4 $\times$ $10^4$ $\Omega$ to 265 $\Omega$. The decrease of resistance is $\sim$ 50 times across the abrupt switch at $V_{Threshold}$, and $\sim$ 200 times across the entire voltage sweep. Assuming that the voltage was applied across the entire thickness of $NbO_2$ film and neglecting all series resistance, the value of threshold electric field ($E_{Threshold}$) was calculated to be $\sim$ 7.5 $\times$ $10^4$ V/cm.

When the applied voltage was swept downwards, the low resistance state relapsed to the initial high resistance state once the voltage was reduced below $V_{Threshold}$. Therefore, the MIT under electric field has threshold switching characteristics, for which only the

high resistance state is stable under zero electric bias and the low resistance state is only stable under electric bias above certain value. Switches between high resistance state and low resistance state occurred at similar voltages in upward and downward sweeps, giving rise to a minimal hysteresis. This phenomenon is different from some previous studies in which consistent hysteresis loops were observed between upward and downward voltage sweeps. [23, 125, 126] Moreover, symmetric switching behaviors were observed when the voltage sweeps were repeated under opposite polarity of bias, indicating unipolar nature of the MIT.

### 6.3.2 Repeatability

Multiple successive ramps of voltage and current were applied through the Nb/$NbO_2$/TiN devices to further characterize the repeatability and consistency of MIT. Examples of 100 consecutive cycles of voltage source and current source sweeps through a 30 $\mu$m $\times$ 50 $\mu$m device are shown in Figure 6.4 (a) and (b), respectively.

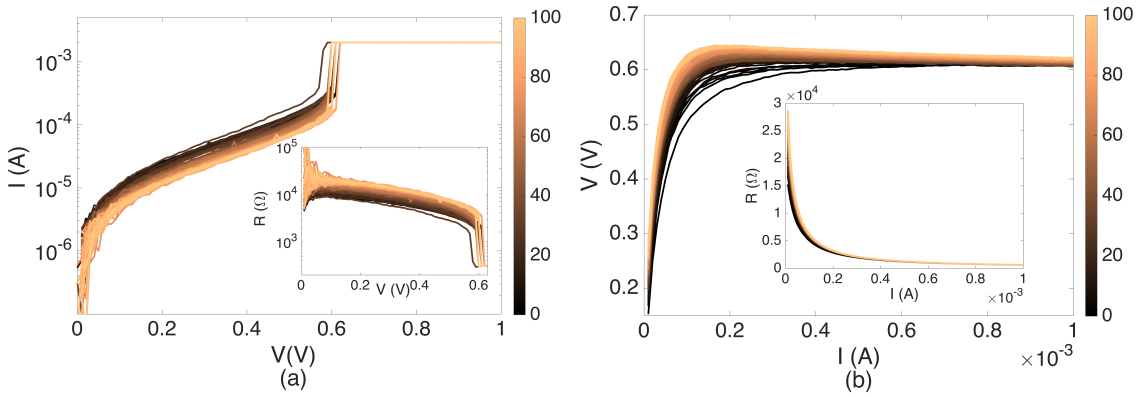


Figure 6.4: (a) Current-voltage (I-V) characteristics of of 100 consecutive voltage source sweeps through a 30 $\mu$m $\times$ 50 $\mu$m Nb/$NbO_2$/TiN device. The inset shows corresponding resistance-voltage (R-V) characteristics, resistance beyond $V_{Threshold}$ not available because current hit the compliance; (b)Voltage-current (V-I) characteristics of 100 consecutive current source sweeps through a 30 $\mu$m $\times$ 50 $\mu$m Nb/$NbO_2$/TiN device. The inset shows corresponding resistance-current (R-I) characteristics.

It is shown that the MIT characteristics was reliably reproducible through the 100 cycles. Meanwhile, some changes in the MIT characteristics are also noticed. In both voltage and current source sweeps, device resistance at high resistance state increased over the cycles of sweeps. For example, during the 100 times of current sweeps, device resistance at the beginning of sweeps increased from $1.7 \times 10^4$ Ω to $2.7 \times 10^4$ Ω. For voltage source sweeps the $V_{Threshold}$ increased slightly and the transitions became increasingly abrupt with the increase of sweep cycles. For current source sweeps, change in resistance was gradual as a function of applied current, and no abrupt drop was observed. Above current of $\sim 0.6$ mA (corresponding voltage is $\sim 0.6$ V), the measured voltage stopped increasing and decreased slightly with the increase of applied current, indicating a negative differential resistance (NDR). The NDR behavior under external electric field in bulk niobium oxide based devices was first reported in 1960s. [10, 63] With increase of cycles of current sweeps, the differential resistance under the high resistance state became increasingly negative.

### 6.3.3 Temperature dependence of MIT characteristics

To evaluate the thermal stability of the MIT and investigate the temperature dependence of MIT characteristics, voltage source sweeps were performed at elevated temperatures. The measured MIT characteristics is shown in Figure 6.5 (a). At each temperature, upward and downward sweeps under both polarities of bias were conducted in the same way as at room temperature. It is shown that effective unipolar threshold switches could be obtained up to 150 °C. With the increase of temperature, the transition became less sharp and the device resistance at high resistance state decreased gradually. From the Arrhenius plot of current values at $V = 0.3$ V in Figure 6.5 (b), an activation energy $E_A \sim 0.24$ eV can be extrapolated according to $I \propto exp(E_A/k_BT)$.

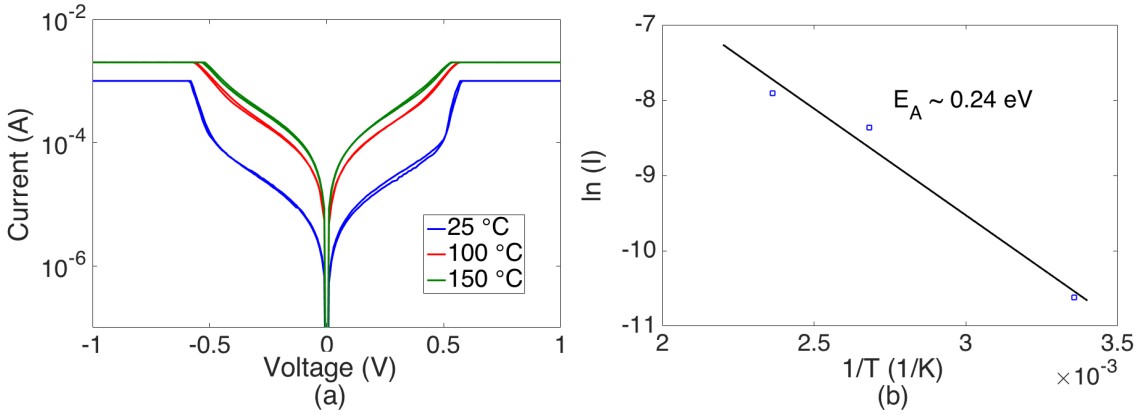


Figure 6.5: (a) Current-voltage (I-V) characteristics of voltage source sweeps through a 30 $\mu$m $\times$ 50 $\mu$m Nb/$NbO_2$/TiN device. Four cycles of sweeps (0-1 V, 1-0V, 0-(-1) V and (-1)-0 V) are shown for each temperature; (b)Arrhenius plot of the measured current $I$ extracted at a voltage of $V$ = 0.3 V, and corresponding fitting that gives a $\sim$ 0.24 eV activation energy.

## 6.4 Effects of $Nb_2O_5$ layer

It has been demonstrated that once $NbO_2$ film is exposed to air, a thin $Nb_2O_5$ layer forms on the surface spontaneously. To better understand the effect on MIT characteristics caused by this surface $Nb_2O_5$ layer, measurements were conducted by probing the tungsten tip directly on the uncovered $NbO_2$ area at both room temperature and elevated temperatures. Typical I-V characteristics is shown in Figure 6.6 (a).

While the I-V curves also demonstrate unipolar threshold switching characteristics with certain thermal stability which is similar to the case of Nb/$NbO_2$/TiN devices, some differences are also noticed. First, the transition took place at higher threshold voltages with more abrupt changes in device resistance. For example, at room temperature, the transition occurred at $\sim$ 2.5 V which corresponded to a threshold electric field of $\sim$ 2.5 $\times$ $10^5$ V/cm, while in Nb/$NbO_2$/TiN devices the transition happened at $\sim$ (0.5 - 0.8) V which corresponded to a threshold electric field of $\sim$ (5 - 8) $\times$ $10^4$ V/cm. Secondly, the I-V characteristics at high resistance state did not show obvious dependence on temperature.

An Arrhenius plot of the current values at $V$ = 1 V is shown in Figure 6.6 (b), which can not be fitted linearly. It is also worth noting that the hysteresis between upward and downward sweeps was more visible with the increase of temperature. Since the measurements on the two devices were performed under same conditions, it is thus speculated that these observed difference was related to the existence of $Nb_2O_5$ layer.

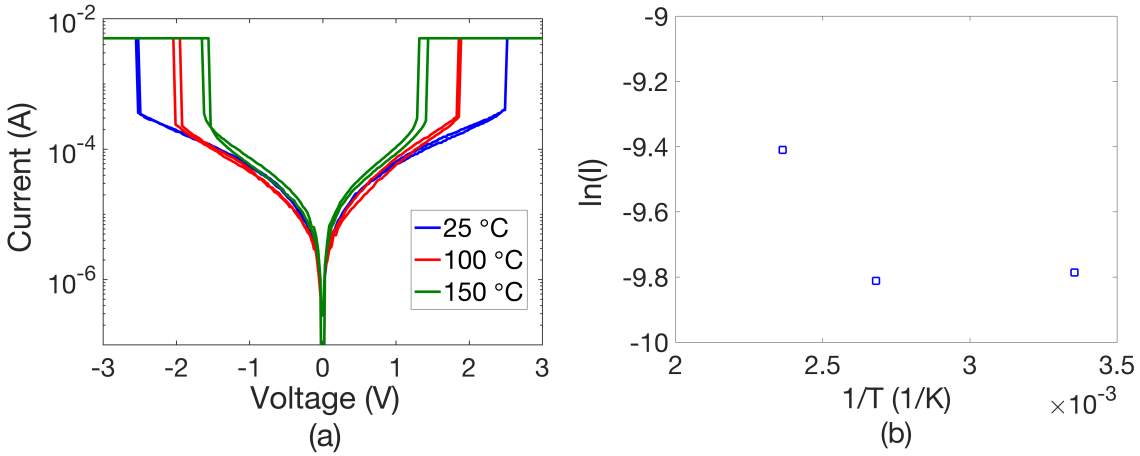


Figure 6.6: (a) Current-voltage (I-V) characteristics of voltage source sweeps through tip/$NbO_2$/TiN vertical device. Four cycles of sweeps (0-3 V, 3-0 V, 0-(-3) V and (-3)-0 V) are shown for each temperature; (b) Arrhenius plot of the current $I$ values extracted at a voltage of $V$ = 1 V.

## 6.5 Conduction mechanisms in $NbO_2$-based devices

Despite that the measurements were performed on the same piece of sample, the observed large difference in I-V characteristics of the two devices indicates that the underlying mechanisms are likely different, due to the $Nb_2O_5$ layer at the interface. To better understand the conduction processes (under high resistance state) in the two structures and the effect of interface $Nb_2O_5$ layer, measured I-V curves were analyzed by fitting them to different conduction models.

It is known that the conduction in a metal-insulator-metal (MIM) structure can be

grouped into two categories, that is, electrode-limited conduction and bulk-limited conduction. The electrode-limited conduction depends on the electrical properties at the interface between electrode and insulating layer, and the most important parameter is the barrier height at the interface. The bulk-limited conduction depends on the electrical properties of the insulating layer itself, such as energy level and density of trap sites. [127, 128] Expressions of common conduction models are summarized in Table 6.2.

| Composition mechanisms | Expressions | Voltage dependence |
|---|---|---|
| Schottky emission | $J = A^* T^2 exp(-\frac{\Phi_B}{k_B T}) exp(\frac{q\sqrt{qV/4\pi d\varepsilon_r\varepsilon_0}}{k_B T})$ | $J \propto exp(\sqrt{V})$ |
| Direct tunneling (Simmons' model) | $J = \frac{q}{4\pi^2\hbar d^2}\{(\Phi_B - \frac{qV}{2}) exp[-\frac{2d(2m)^{1/2}}{\hbar}(\Phi_B - \frac{qV}{2})^{1/2}]$ $-(\Phi_B + \frac{qV}{2}) exp[-\frac{2d(2m)^{1/2}}{\hbar}(\Phi_B + \frac{qV}{2})^{1/2}]\}$ | |
| Fowler-Norheim tunneling | $J = \frac{q^3 V^2}{16\pi^2\hbar d^2 \Phi_B} exp(-\frac{4(2m^* q)^{1/2} d\Phi_B^{3/2}}{3\hbar V q})$ | $J \propto V^2 exp(\frac{1}{V})$ |
| Poole-Frenkel emission | $J = \frac{R_0 V}{d} exp(-\frac{W_A}{k_B T}) exp(\frac{q\sqrt{qV/d\pi\varepsilon_r\varepsilon_0}}{k_B T})$ | $J \propto V exp(\sqrt{V})$ |
| Hopping conduction | $J = qaN\nu exp(\frac{qaV}{dk_B T}) exp(-\frac{W_A}{k_B T})$ | $J \propto exp(V)$ |
| Space-charge-limited emission | $J = \frac{9\mu\varepsilon V^2}{8d^3}$ | $J \propto V^2$ |
| Ohmic conduction | $J = \frac{qN_0\mu V}{d} exp(\frac{-W_A}{k_B T})$ | $J \propto V$ |

Table 6.2: Conduction mechanisms in MIM structures, including electrode-limited conduction (upper part) and the bulk-limited conduction (lower part). $J$ is the current density, $V$ is the applied voltage, $T$ is temperature, $\hbar$ is reduced Plank constant, $k_B$ is Boltzmann constant, $d$ is insulator thickness, $\varepsilon_0$ is the permittivity in vacuum, $\varepsilon_r$ is the optical dielectric constant, $m^*$ is effective mass, $A^*$ is the effective Richardson constant, $\Phi_B$ is barrier height, and $W_A$ is activation energy. [127, 129, 130]

### 6.5.1 Conduction in Nb/$NbO_2$/TiN device

For this part of discussion, I-V curves of upward voltage source sweeps under positive bias in Figure 6.5 (a) are analyzed. As is shown by Figure 6.5, the conduction in Nb/$NbO_2$/TiN device under high resistance state is likely to have an activation energy which is extrapolated to be $\sim$ 0.24 eV. For electrode-limited conduction, the conduction due to tunneling is nearly temperature independent, while the thermionic (Schottky) emission exhibits temperature dependence. [127] However, the symmetric behavior of I-V curves under opposite polarity of bias suggests the conduction is not likely to be dominated by Schottky emission.

For the bulk-limited conduction, conduction process with an activation energy is generally considered to be either Poole-Frenkel type or hopping type. The existence of these conduction mechanisms was identified by examining the respective linear relations (*ln(I/V)* vs. $\sqrt{V}$ for Poole-Frenkel emission and *ln(I)* vs. $V$ for hopping conduction) given by

$$Poole-Frenkel: ln(\frac{I}{V}) = \frac{q\sqrt{q/d\pi\varepsilon_r\varepsilon_0}}{k_BT}\sqrt{V} - \frac{W_A}{k_BT} + ln(\frac{R_0}{d}) + M \tag{6.1}$$

$$Hopping: ln(I) = \frac{qa}{dk_BT}V - \frac{W_A}{k_BT} + ln(qaN\nu) + M \tag{6.2}$$

in which $M$ is a constant, and all other parameters are the same as defined in Table 6.2.

By plotting the I-V characteristics in the formalism of these two models, it is clear that the conduction can be well reproduced by the hopping conduction model instead of Poole-Frenkel emission model (Figure 6.7). The fitting of I-V characteristics at different temperatures to hopping model is demonstrated in Figure 6.8. As is suggested by Eq. 6.2, the intercepts of the linear fitting between *ln(I)* and $V$ to $y$-axis (defined as $Y$) should demonstrate an linear dependence on *1/T*, and the value of activation energy $W_A$ can be extracted

from the slope of linear fitting. As is shown in Figure 6.8 (b), the relation between $Y$ and $1/T$ can be fitted linearly and an activation energy of $\sim 0.23$ eV can be extracted.

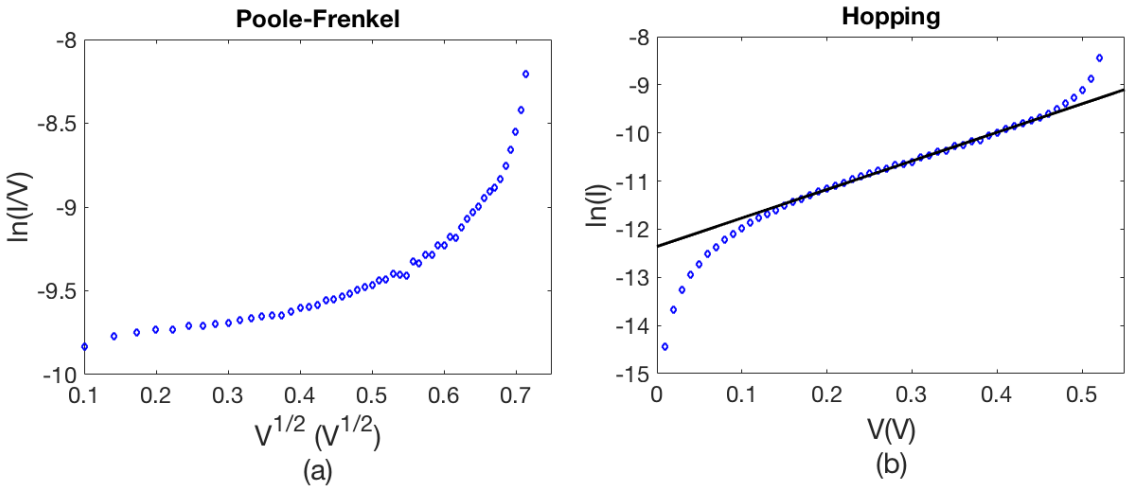


Figure 6.7: (a) Poole-Frenkel conduction plot ($ln(I/V)$ vs. $\sqrt{V}$) and (b) hopping conduction plot ($ln(I)$ vs. $V$) with corresponding linear fitting of $I$-$V$ characteristics in Nb/$NbO_2$/TiN device at room temperature.

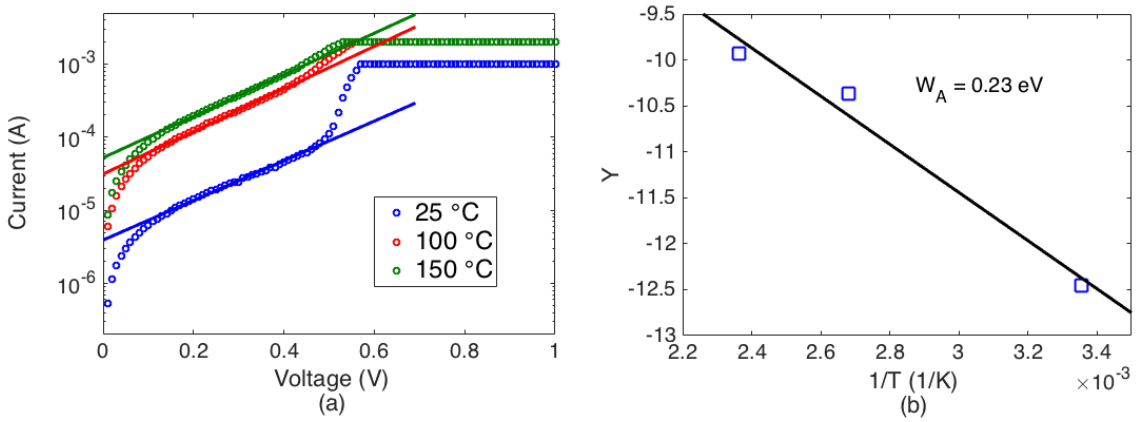


Figure 6.8: (a) Fitting to hopping conduction model of $I$-$V$ characteristics at different temperatures in Nb/$NbO_2$/TiN device; (b) Dependence of $Y$ value on $1/T$ and linear fitting.

It has been reported that the conduction at high resistance state of $NbO_2$-based devices was dominated by Poole-Frenkel effect. [12, 13, 131] Compared with those studies, $NbO_2$ layer in this Nb/$NbO_2$/TiN device is much thicker and electric field across $NbO_2$ layer is

much smaller. In the device discussed here, the voltage range under discussion is $\sim$ (0 - 0.5) V. Assuming the voltage is applied across the whole thickness of $NbO_2$, corresponding electric filed is $\sim$ (0 - $4.8\times10^4$) V/cm. In studies claimed Poole-Frenkel emission conduction, the electric field was $\sim$ (1-10) $\times$ $10^5$ V/cm. [12, 13]

Comparing the two conduction mechanisms, Poole-Frenkel emission corresponds to the thermionic effect while hopping conduction corresponds to the tunneling effect. For Poole-Frenkel emission, carriers overcome the energy barrier owing to the thermal activation under electric field, with the effective barrier height being lowered by the applied field, therefore this conduction is often observed at high temperature and relatively large electric field. In hopping conduction, the carriers' energy is not as high as that of the barrier so the carriers transit by tunneling. [127]

For polycrystalline $NbO_2$ films in the investigated devices, charge carriers can be localized due to disordering rising from grain boundaries, interaction with lattice (small polarons), or trap sites due to point defects in lattice, resulting in hopping type conduction. Under low voltage bias, carriers can transport with assistance of thermally driven phonons. With the increase of applied bias, the carrier hopping process is further facilitated in the direction of the electric field. It has been proposed that a field-assisted term $exp(F/k_BT)$ where $F$ is the electric field can be added to the conduction expression. [42, 132–134]

Variation of I-V characteristics with sweep cycles demonstrated in Figure 6.4 is analyzed by hopping conduction model. For both voltage source and current source sweeps, I-V curves of three sweep cycles (the 1st, 51st and 100th) are chosen as examples to compare and to be fitted to the hopping conduction model (Figure 6.9). It is found that slopes of linear fitting to hopping conduction remain almost unchanged, while the magnitude of intercepts to $y$-axis increases over cycles of sweeps monotonically. As is given by Eq. 6.2, the intercept is determined by $(-W_A/k_BT + ln(qaN\nu) + M)$. While further study is needed for more precise conclusion, the variation with sweep cycles could be related to the varia-

tion in defect states participating in conduction process.

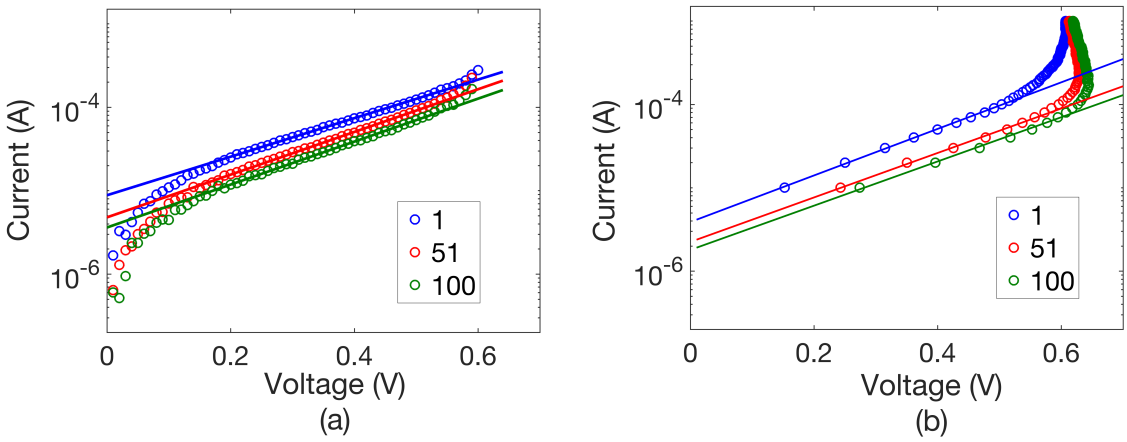


Figure 6.9: (a) Examples of fitting of I-V curves in Figure 6.4 (a) to hopping conduction model; (b) Examples of fitting of I-V curves in Figure 6.4 (b) to hopping conduction model.

### 6.5.2 Conduction in tip/$NbO_2$/TiN device

For this part of discussion, I-V curves of upward sweeps under positive bias in Figure 6.6 (a) are analyzed. Since the conduction at high resistance state does not exhibit obvious Arrhenius dependence on temperature, tunneling-type conduction mechanisms are analyzed with emphasis. Based on the comparison between applied bias and barrier height, tunneling conduction across the barrier can be divided into direct tunneling ($V < \Phi_B/q$) and Fowler-Norheim tunneling ($V > \Phi_B/q$) (illustrated by Figure 6.10). [127, 130, 135] For Fowler-Norheim tunneling conduction, a plot of $ln(I/V^2)$ vs. $(1/V)$ should be linear (given in Eq. 6.3 below), which cannot be satisfied by the measured I-V characteristics (Figure 6.11 (b)).

$$ln(I/V^2) = -\frac{4(2m^*)^{1/2}d\Phi_B^{3/2}}{3\hbar q}\cdot\frac{1}{V} + ln(\frac{Aq^3}{16\pi^2\hbar d^2\Phi_B}) + M \tag{6.3}$$

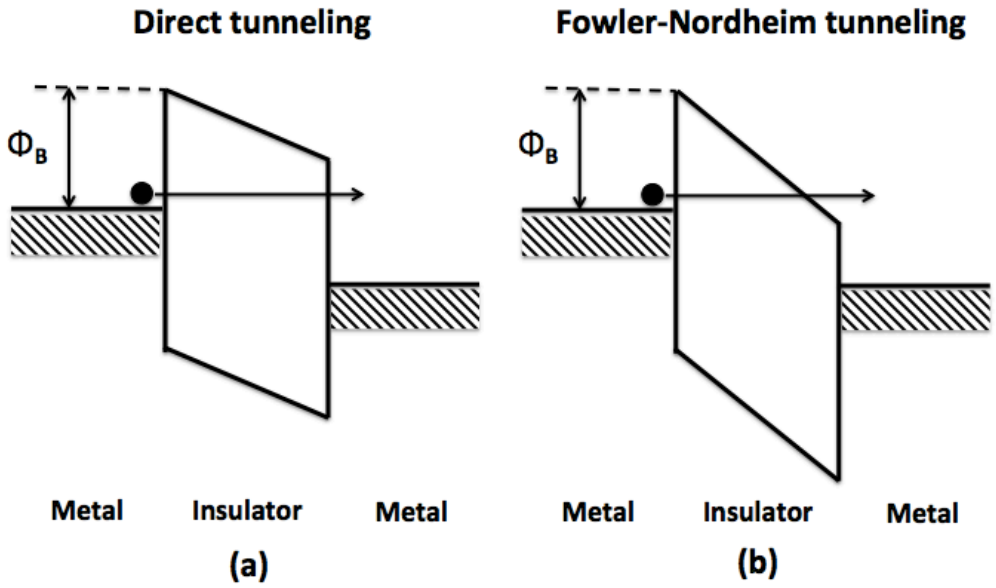


Figure 6.10: (a)Schematic energy band diagram of direct tunneling conduction; (b) Schematic energy diagram of Fowler-Norheim tunneling conduction. [127, 130, 135].

For the case of direct tunneling, Simmons' equation which describes the direct tunneling current through rectangular energy barrier between electrodes under intermediate bias (V$<\Phi_B$/q) is used (listed in Table 6.2). The The equation can be reformulated to

$$\begin{aligned} I \propto \frac{q^2}{8\pi^2\hbar d^2}\{(\frac{2\Phi_B}{q}-V)exp[-\frac{2d(mq)^{1/2}}{\hbar}(\frac{2\Phi_B}{q}-V)^{1/2}] \\ -(\frac{2\Phi_B}{q}+V)exp[-\frac{2d(mq)^{1/2}}{\hbar}(\frac{2\Phi_B}{q}+V)^{1/2}]\} \end{aligned} \tag{6.4}$$

The equation to which the measured I-V characteristics under high resistance state was fitted is given below. The energy barrier height $\Phi_B$ and thickness of energy barrier $d$ can also be extracted from the fitted parameters.

$$\begin{aligned} I = p_1\{(p_2-V)exp[-p_3(p_2-V)^{1/2}]-(p_2+V)exp[-p_3(p_2+V)^{1/2}]\} \\ p_2=\frac{2\Phi_B}{q}, \quad p_3=\frac{2d(mq)^{1/2}}{\hbar} \end{aligned} \tag{6.5}$$

Fitting result of *I-V* characteristics in the upward voltage sweep at room temperature in tip/$NbO_2$/TiN structure is shown in Figure 6.11 (a). The barrier height $\Phi_B$ is extracted to be $\sim$ 2.5 eV and thickness of energy barrier $d$ is calculated to be $\sim$ 1 nm. The conduction of the entire high resistance state can be well reproduced by the Simmons' equation, and height and thickness of the barrier are also reasonable assuming the barrier is due to the $Nb_2O_5$ layer formed upon exposure to air.

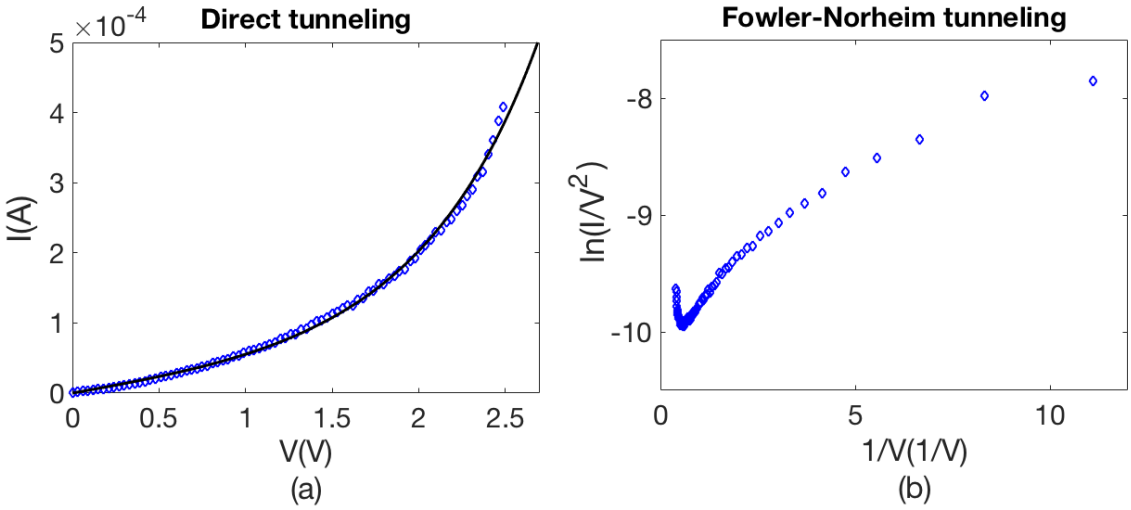


Figure 6.11: (a) Fitting of *I-V* characteristics of tip/$NbO_2$/TiN device to Simmons' equation; (b) Fowler-Norheim tunneling plot ($ln(I/V^2)$ vs. $1/V$) of measured *I-V* characteristics.

Figure 6.12 (a) shows results of fitting *I-V* curves of upward voltage sweeps under positive bias in Figure 6.6 (a) to Simmons' equation. The extracted energy barrier height as a function of temperature is plotted in Figure 6.12 (b). The decrease of energy barrier height with temperature can be attributed to the substantial diffusion of oxygen via the interstitial sites through $Nb_2O_5$, which has been observed in the native oxides on the surface of single crystal Nb (110). [136] While the direct tunneling conduction should not exhibit dependence on temperature according to the equation, the variation of energy barrier height can provide explanation on the decrease of $V_{Threshold}$ with temperature.

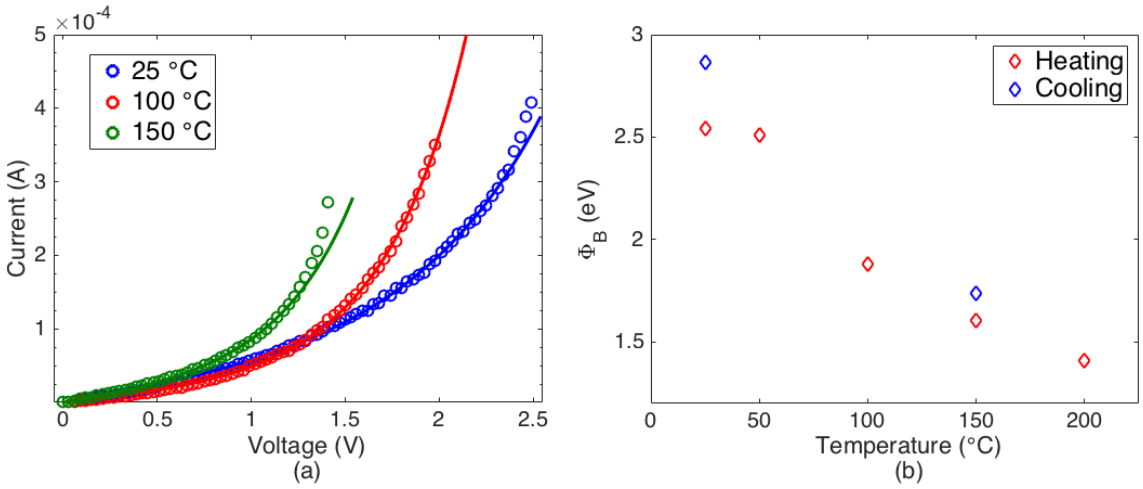


Figure 6.12: (a) Fitting of I-V characteristics of the positive upward sweeps in Figure 6.6 to Simmons' equation; (b) Temperature dependence of barrier height ($\Phi_B$) in tip/$NbO_2$/TiN devices.

It is noticed that the natural oxide layer at the surface of Nb top contact which contains $Nb_2O_5$ did not result in high energy barrier that could significantly affect conduction process in the Nb/$NbO_2$/TiN devices. That could be related to the composition of the oxide layer which consists with $Nb_2O_5$, $NbO_2$, and NbO from surface to the bulk Nb. [136] Further study to compare oxide layers on Nb surface and $NbO_2$ surface is needed to better understand this difference.

### 6.5.3 Proposed band diagrams

Based on the analysis on conduction processes above, schematics of the electronic structures for these two devices at room temperature are proposed in Figure 6.13. It appears that the *in-situ* Nb capping produces a clean contact interface between the electrode Nb and $NbO_2$ film, with minimal effect of $Nb_2O_5$. Electrical transport in the Nb/$NbO_2$/TiN structure is therefore dominated by the bulk of $NbO_2$ film, which can be described by an field-assisted hopping conduction with an activation energy of $\sim$ 0.23 eV. When probing

the tip directly on the uncovered area of $NbO_2$ film, a thin $Nb_2O_5$ layer exists between the tungsten tip and $NbO_2$ film. $Nb_2O_5$ is a well-known insulator with a band gap of $\sim$ 3.3 eV [137, 138], and the existence of the interface $Nb_2O_5$ results in a relatively high energy barrier which is $\sim$ 2.5 eV at room temperature. The electrical transport through the vertical structure is therefore limited by the $Nb_2O_5$ layer and the conduction takes place by direct tunneling which can be described by Simmons' equation.

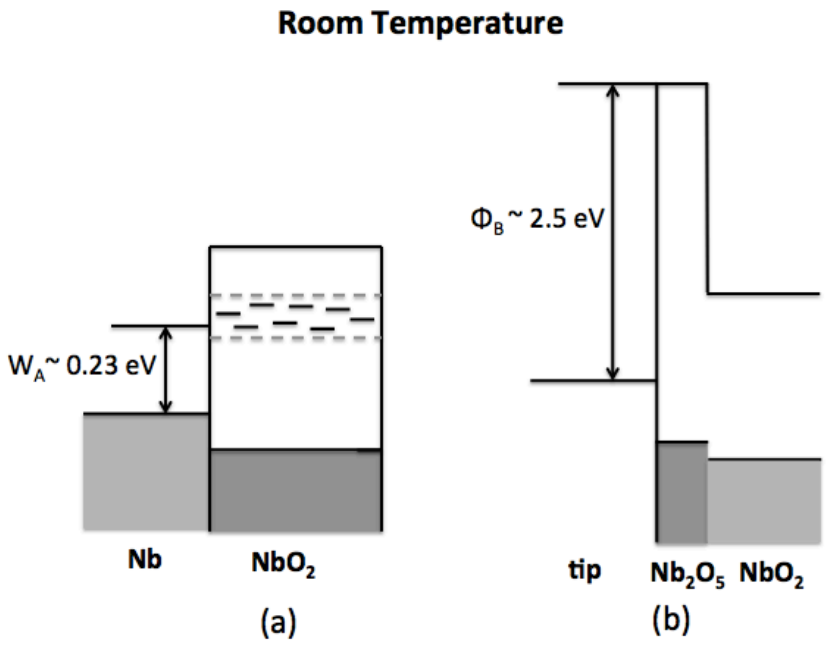


Figure 6.13: Proposed band diagrams for (a) Nb/$NbO_2$/TiN and (b) tip/$NbO_2$/TiN.

For the application in selecting devices in crosspoint arrays, it is essential that the material has highly non-linear I-V curves with low OFF leakage current and relatively high threshold voltage for switching. Therefore a highly resistive OFF state is desirable. [139] Besides improving the quality of deposited $NbO_2$ films to reduce the extrinsic conduction due to defects, another approach could be to introduce a thin layer of more insulating material to form a high energy barrier. Effort to integrate $Nb_2O_5$ or oxygen-rich niobium oxide with $NbO_2$ has been reported, with improved device performance. [140–142] $Nb_2O_5$

exhibits memory switching characteristics, which is the property employed by ReRAM. Therefore a good understanding on the role played by the $Nb_2O_5$ is important, especially on how it is affected by the thickness and composition.

## 6.6 Discussion on MIT mechanism

As is introduced in Chapter 2, the driving mechanism behind the MIT under electric field is still controversial. While more characterization (for example, time-resolved measurement on the transition process) is required to determine the mechanism, some discussion can be made based on the obtained results in this chapter.

First, temperature of $NbO_2$ film in Nb/$NbO_2$/TiN devices at MIT is estimated by calculating the film resistivity and comparing it to the ρ vs. $T$ characteristics of $NbO_2$ film on sapphire substrate in Chapter 4 (shown in Figure 4.13).

The I-V characteristics shown in Figure 6.3 is taken as an example. The measured resistance at the onset of transition is$\sim 1.4 \times 10^4\ \Omega$, and the corresponding resistivity is calculated under three different assumptions. The first one is to assume the current is uniformly distributed under the Nb electrode, and therefore the resistivity is estimated using the volume of $NbO_2$ film covered by the electrode (30 $\mu$m $\times$ 50 $\mu$m $\times$ 104 nm). Considering the possibility that the switching occurs by formation of a conducting filament, resistivity is also estimated using cylinder of $NbO_2$ with radius 2.5 $\mu$m (size of tungsten tip) and 30 nm [12]. The calculated resistivity values are listed in Table 6.3.

| Investigated $NbO_2$ volume | Film cover by 30 $\mu$m $\times$ 50 $\mu$m electrode | Filament with 2.5 $\mu$m radius | Filament with 30 nm radius |
|---|---|---|---|
| Estimated resistivity | $2 \times 10^4\ \Omega \cdot cm$ | $264\ \Omega \cdot cm$ | $0.04\ \Omega \cdot cm$ |

Table 6.3: Estimated resistivity of $NbO_2$ at the onset of MIT.

$NbO_2$ films in vertical devices of this chapter were deposited under same conditions as the optimized $NbO_2$ film on sapphire in Chapter 4, and the phase composition characterization demonstrates very similar results (Raman spectrum and XPS). Therefore its assumed that resistivity of $NbO_2$ film on TiN/Si(100) was close to that of $NbO_2$ film on sapphire. By comparing the calculated resistivity in Table 6.3 to the ρ vs. $T$ characteristics in Figure 4.13, it is found that values of film resistivity estimated under the first two assumptions are much larger than the measured resistivity of $NbO_2/Al_2O_3(0001)$ even at room temperature. Therefore it is likely that the MIT occurred within a tiny filament which conducted most of the current. Using the dimension in other simulation studies on the switching in $NbO_2$-based devices [12], the film resistivity is estimated to be $\sim 0.04\ \Omega \cdot cm$. Assuming that the fitted Arrhenius dependence near 400 K of $NbO_2/Al_2O_3(0001)$ still holds when temperature is not much higher than 400 K, the temperature corresponding to the film resistivity is estimated to be $\sim$ 510 K, which is still far from the MIT transition temperature of $NbO_2$ (1081 K).

Moreover, it is noticed that MIT of Nb/$NbO_2$/TiN device demonstrated minimal hysteresis between upward and downward sweeps of electric field. The transition from high resistance state to low resistance state and the opposite one took place at $V_{Threshold}$s close to each other, therefore the power at the transition points of the two opposite transition processes (illustrated as "ON" and "OFF" points in Figure 6.3) mainly depended on the current values and exhibited large difference (43 $\mu$W and 2.43 mW). The large power discrepancy indicates that the transition could not be purely thermally induced.

Therefore, the nature of MIT under electric field is likely to be electronic. The increased carrier concentration due to field-induced generation and thermal generation could result in changes in electronic structure and eventually the transition takes place.

## 6.7 Summary

In this chapter, vertical devices based on $NbO_2$ films deposited on TiN/Si(100) substrates were fabricated and MIT under electric field in the devices was investigated. The MIT demonstrated unipolar threshold switching characteristics, with minimal hysteresis. Reliable MIT were retained over hundreds of sweep cycles and up to 150°C. *In-situ* Nb capping was employed to prevent spontaneous formation of $Nb_2O_5$ at $NbO_2$ film surface due to air exposure, the effect of which on MIT characteristics was also investigated by comparing I-V characteristics in Nb/$NbO_2$/TiN structures and tip/$NbO_2$/TiN structures. It was found that conduction in the structures with minimal $Nb_2O_5$ (Nb/$NbO_2$/TiN) was dominated by hopping conduction in the bulk of $NbO_2$ film, while conduction in the structure with interface $Nb_2O_5$ (tip/$NbO_2$/TiN) was dominated by the tunneling conduction through the more insulating $Nb_2O_5$ layer, leading to larger threshold voltages and more visible hysteresis. The insight on modification effect of $Nb_2O_5$ promises better control on the MIT characteristics in $NbO_2$-based devices.

# Chapter 7

# Summary and future work

## 7.1 Summary of scientific observations

In summary, this dissertation is an experimental study on MIT of $NbO_2$ thin films synthesized by RBTIBD technique. Deposition of phase pure $NbO_2$ films, effect of deposition variables ($Ar/O_2$ flow rate, substrate heating and vanadium substitution) on film property, as well as MIT in $NbO_2$ films under electric field have been investigated.

Growth of high quality $NbO_2$ films has been developed on (0001) sapphire substrates using RBTIBD technique. Deposited films contained highly pure tetragonal $NbO_2$ phase, which was confirmed by Raman spectrum and XPS results. Films were epitaxial with $\langle 001\rangle(110)NbO_2||\langle 10\bar{1}0\rangle(0001)Al_2O_3$ orientation relation with substrates. Characterization on temperature dependence of electrical transport between 180 K and 400 K suggested that the conduction was dominated by Efros-Shklovskii VRH at lower temperature and some other processes involving thermally activation of carriers at higher temperature. An important observation was the spontaneous formation of a thin layer of $Nb_2O_5$ ($\sim$ 1-2 nm) at film surface due to oxidation in ambient environment, which needs to be aware of in film characterization or device fabrication. Within the investigated ranges of growth condition parameters, film quality (phase composition, microstructures, electrical transports, etc.) was found to be highly dependent on $Ar/O_2$ mixture flow rate, but much less

sensitive to substate temperature. Characterization on deposited films suggested that point defects related to oxygen stoichiometry played an important role in affecting film properties. The progress in $NbO_2$ film synthesis promises further advance on understanding the intriguing properties of this materials especially the MIT phenomenon. With phase purity of $NbO_2$ films being more effectively controlled, the effect of other oxide phases can be better eliminated and the intrinsic physical properties of $NbO_2$ films can be characterized more accurately. It was also indicated that the existence of defect states in the band gap as well as the size of band gap could be modified by variance in the presence of defects, therefore the MIT properties could be modified by tuning growth conditions.

V substitution has also been studied as an approach to modify physical properties of deposited films. Doping methods using RBTIBD technique were explored, and control on composition was realized by tuning pulse width applied to individual targets. It was demonstrated that the V substitution broke the Nb-Nb bonds and led to collapse of distorted rutile symmetry. With the increase of V concentration, film lattice gradually transited from tetragonal lattice of semiconducting $NbO_2$ to regular rutile lattice. The V substitution seemed to provide an approach to tuning the relative contribution from electron-lattice interaction (Peierls transition) and electron-electron interaction (Mott transition). As the V concentration increased, the distortion due to Nb-Nb paring reduced which corresponded to decrease in the electron-lattice interaction, while stronger electron-electron interaction was increased due to the stronger Coulomb interaction of V $3d$ electrons. Therefore more insights on MIT mechanisms can be obtained by comparing characteristics of MIT processes under different excitations in samples with different V concentration.

MIT in $NbO_2$ under electric field was obtained on structures based on $NbO_2$ films grown on TiN/Si(001) substrates, which contained highly pure polycrystalline $NbO_2$ phase. The obtained MIT demonstrated unipolar threshold switching characteristics, with repeatability up to hundreds of cycles and thermal stability up to 150°C. Analysis on I-V charac-

teristics suggested that the conduction processes under high resistance state was dominated by hopping conduction in $NbO_2$ films and the MIT was likely to be driven by changes in electronic structures instead of being thermally driven by Joule heating. *In-situ* Nb capping was employed to prevent the formation of $Nb_2O_5$ surface layer due to air exposure, which was found to result in more abrupt switches, larger threshold electric fields, and more visible hysteresis. The conduction in structures with $Nb_2O_5$ layer was found to be dominated by tunneling conduction through the $Nb_2O_5$ layer. The effective control on phase purity of $NbO_2$ film and presence of $Nb_2O_5$ layer enabled separation of effect from the two oxide layers ($NbO_2$ and $Nb_2O_5$) on MIT characteristics, which is of great importance on understanding mechanisms of MIT under electric field in related devices. The insights on effect of interfacial $Nb_2O_5$ layer also provided guidance on utilizing the $Nb_2O_5$ layer to improve the non-linearity of $NbO_2$-based switching devices.

## 7.2 Future work

Exploration on $NbO_2$ thin film growth and MIT in $NbO_2$ under electric field were the objectives of this work. Discussed below are my recommendations and suggestions for future research work on this topic.

• *Further exploration on V substitution*

V substitution of $NbO_2$ films and resulting modification effect on structural and transport properties were described in Chapter 5, the exploration on which can be further conducted.

First, oxygen stoichiometry of samples with different V concentration needs to be further optimized before more characterization can be performed. For the studied set of samples in Chapter 5, flow rate of $Ar/O_2$ was fixed while the total amount of metal sputtering increased. Therefore, possible effect of oxygen deficiency could not be eliminated when

discussing the modification effect of V substitution, especially on transport properties. For each value of V concentration (corresponding to certain combination of target bias conditions), the $Ar/O_2$ flow rate needs to be optimized to provide a set of samples with different V concentration and metal-oxygen stoichiometry close to optimal values. With such samples, modification effect of V substitution can be evaluated more accurately. Structural properties including lattice types and lattice parameters, transport properties including electrical conductivity, carrier density and mobility, Seebeck coefficient and thermal conductivity as functions of V concentration can be characterized. Characterization on valence states of V and Nb ions (by X-ray absorption) will be helpful.

Moreover, the question of greater interest is the modification effect on MIT characteristics (under electric field or optical excitations). For MIT under electric field, the same vertical structures as in Chapter 6 can be employed, and MIT characteristics at room temperature as well as its variation with temperature can be compared among samples with different V concentration. Time-resolved measurements can also be included to compare the transition speeds and evolution processes. Optically, same time-resolved pump-probe measurements as in Ref. [11] can be performed on $V_xNb_{1-x}O_2$ film samples with different V concentration. Time-resolved transition processes, and important parameters including response and recover times, threshold fluence of optical excitation should be compared as functions of V concentration.

As was revealed by the results in Chapter 5, the distortion due to Nb-Nb pairing decreased and finally vanished with the increase of V concentration. Meanwhile, it was also anticipated that the increased randomness introduced by V substitution and stronger electron-electron interaction due to stronger Coulomb interaction of V $3d$ electrons would have effect on transport and MIT properties. Therefore, the exploration on $V_xNb_{1-x}O_2$ film samples can provide some hints on the respective roles played by different transition mechanisms. For samples with low V concentration so the distorted rutile lattice is still

maintained, it is likely that the MIT under electric field or optical excitation is able to be obtained, with variance in transition characteristics. For samples with higher V concentration and regular rutile lattice, the possible occurrence of MIT would suggest dominance of mechanisms other than Peierls transition process(such as Mott transition).

• *Further exploration on epitaxial $NbO_2$ thin films*

Study on epitaxial $NbO_2$ thin films can be further conducted for better understanding and more effective utilization of the intriguing properties of this material, especially the MIT properties.

Growth of epitaxial $NbO_2$ films provides one more approach to modify film properties, which is the strain in film. Film strain can produce variance in lattice structures and therefore band structures, and provide approaches to separate effect of Peierls and Mott MIT mechanisms. It has been reported that in $VO_2$ films clamped on $TiO_2$ substrates, the $VO_2$ films took the regular rutile structure, but still exhibited MIT, with $T_{MIT}$ modified by the strain. [143] Strain in film can be tuned by film thickness and film lattice parameters (by tuning growth conditions), and introduction of buffer layers between films and substrates can also be explored. For each investigated type of substrate, structural properties of deposited films, including orientation relations with substrates and lattice parameters, need to be characterized in combination with transport properties. Measurements on carrier density and mobility will be helpful.

In particular, growth of epitaxial $NbO_2$ films on $TiO_2$ substrates, which have similar crystal structure and lattice parameters, can be explored. The deposited films may experience biaxial or uniaxial strain, depending on the lattice mismatch values along different directions and film thickness. For films with single orientation, anisotropy in physical properties can also be characterized and compared, especially between directions parallel and perpendicular to Nb-Nb dimers. It can be anticipated that the lattice mismatch can lead to variance in growth conditions for single phase and epitaxial films, and result in difficulty

in optimizing growth conditions. For example, some preliminary work has been done on the growth of $NbO_2$ films on (100) $TiO_2$ substrates, and the microstructure characterization is summarized in Figure 7.1. In the case of (100) $TiO_2$ substrates, it was indicated that the substrate heating temperature had a more significant effect on the microstructure of $NbO_2$ films than in the case of sapphire substrates. In this case, variance in orientation relations between $NbO_2$ films and substrates may be induced by changes in substrate heating temperatures, and it is possible to obtain different orientation relations and therefore different strain modification effect by tuning growth conditions.

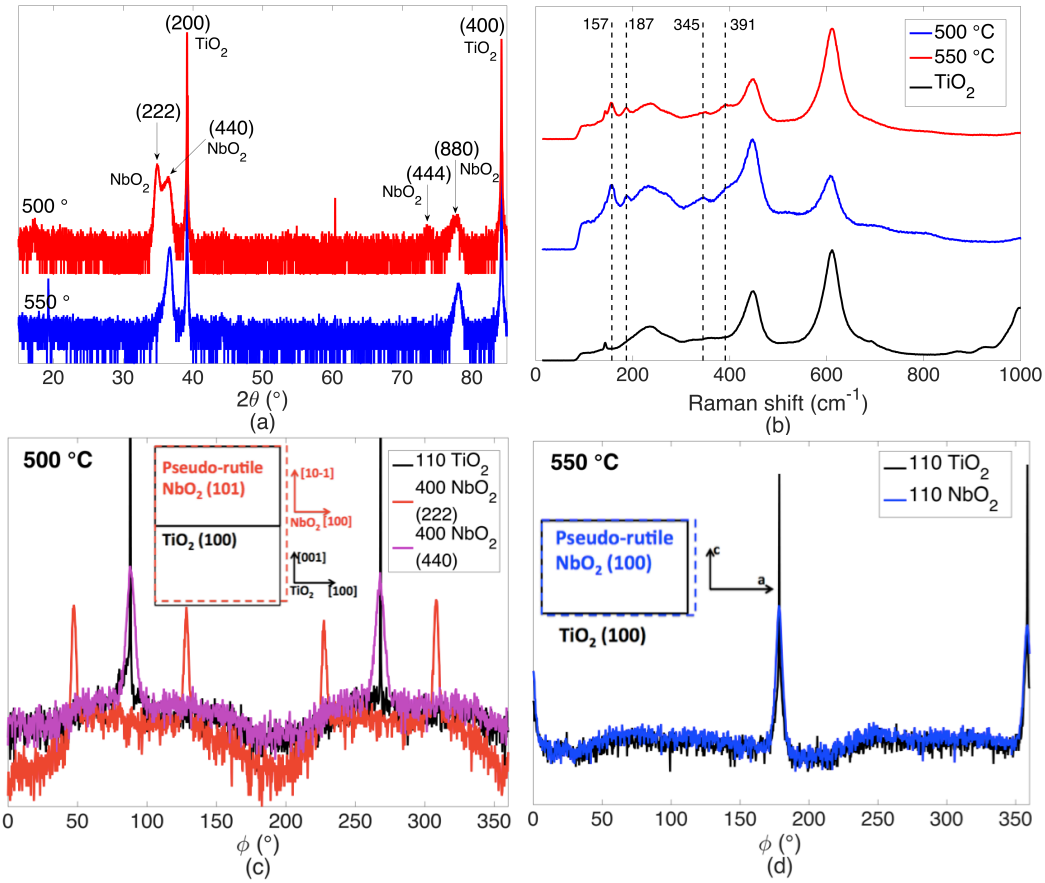


Figure 7.1: (a) XRD 2θ-ω scans and (b) Raman spectra of $NbO_2$ film deposited on (100) $TiO_2$ substrates at 500 °C and 550 °C; (c) In-plane ϕ scan of (400) diffraction peaks based on out-of-plane $NbO_2$ diffraction (222) (red), ϕ scan of (400) diffraction peaks based on out-of-plane $NbO_2$ diffraction (440) (purple) and ϕ scan of (110) diffraction peaks of (100) $TiO_2$ (black) for the sample deposited at 500 °C, the inset illustrates the orientation relation between (222) $NbO_2$ and substrate; (d) In-plane ϕ scan of (400) diffraction peaks based on out-of-plane $NbO_2$ diffraction (440) (blue) and ϕ scan of (110) diffraction peaks of (100) $TiO_2$ (black) for the sample deposited at 550 °C, the inset illustrates the orientation relation between (440) $NbO_2$ and substrate.

# Appendix A

## Substitutional alloyed (V-rich) $V_xNb_{1-x}O_2$ films

Besides the Nb-rich $V_xNb_{1-x}O_2$ samples described in Chapter 5, V-rich $V_xNb_{1-x}O_2$ samples were also synthesized and investigated. Some representative results are included here for comparison. For deposition of this set of samples, sputtering rate of V target was fixed while sputtering rate of Nb target was varied by tuning pulse width. Deposition conditions are listed in Table A.1, and all samples were deposited for 60 min. Film thickness and Nb concentration (measured by Rutherford backscattering (RBS) by collaborators Nate Newman and Matthew Edwards from Arizona State University) are listed in Table A.2.

| Deposition conditions | S1 | S2 | S3 | S4 | S5 |
|---|---|---|---|---|---|
| Ar/$O_2$ Mix Flow Rate (SCCM) | 6 | 6 | 6 | 6 | 6 |
| Process Pressure (mTorr) | 0.92 | 0.92 | 0.83 | 0.9 | 0.86 |
| Substrate Temperature (°C) | 400 | 400 | 400 | 400 | 400 |
| DC Pulse Frequency to Nb Target (kHz) | — | 10.10 | 10.10 | 10.10 | 10.10 |
| Positive Duty Cycle to Nb Target ($\mu$s) | — | 58 | 60 | 63 | 71 |
| Negative Duty Cycle to Nb Target ($\mu$s) | — | 41 | 39 | 36 | 28 |
| DC Pulse Frequency to V Target (kHz) | 71.43 | 71.43 | 71.43 | 71.43 | 71.43 |
| Positive Duty Cycle to V Target ($\mu$s) | 3 | 3 | 3 | 3 | 3 |
| Negative Duty Cycle to V Target ($\mu$s) | 11 | 11 | 11 | 11 | 11 |
| Positive target bias (V) | 20 | 20 | 20 | 20 | |
| Negative target bias (V) | 900 | 900 | 900 | 900 | 900 |
| Recorded Negative Target Bias Current (A) | 109.5 | 125 | 129 | 135 | 151 |
| Cathode Ar Flow Rate (SCCM) | 10 | 10 | 10 | 10 | 10 |
| Cathode Current (A) | 7 | 7 | 7 | 7 | 7 |
| Anode Ar Flow Rate (SCCM) | 70 | 70 | 70 | 70 | 70 |
| Anode Current (A) | 6.5 | 6.5 | 6.5 | 6.7 | 6.5 |

Table A.1: Deposition condition parameters of V-rich $V_xNb_{1-x}O_2$ films with variation in V concentration.

| Sample | S1 | S2 | S3 | S4 | S5 |
|---|---|---|---|---|---|
| Film thickness | 48.8 | 47.9 | 53.2 | 58.8 | 88.5 |
| $Nb\%_{fr}$ | 0% | 2.4% | 4.6% | 8.9% | 27% |

Table A.2: Film thickness and concentration of V-rich $V_xNb_{1-x}O_2$ films. ($V\%_{fr}$: Courtesy of Nate Newman and Matthew Edwards from Arizona State University.)

Raman spectra of the V-rich $V_xNb_{1-x}O_2$ films are shown in Figure A.1. Raman bands near 195 $cm^{-1}$ and 225 $cm^{-1}$, which are related to the vibration modes of V-V paring, depressed fast with the increase of Nb content. These two bands exhibited little intensity for S4 (with 8.9% Nb), indicating that point symmetry of the monoclinic $VO_2$ lattice was almost destroyed and the lattice took the regular rutile type. Compared with the Nb-rich $V_xNb_{1-x}O_2$ films, it indicated that the detrimental effect of Nb substitution to $VO_2$ lattice was larger than that of V substitution to $NbO_2$ lattice.

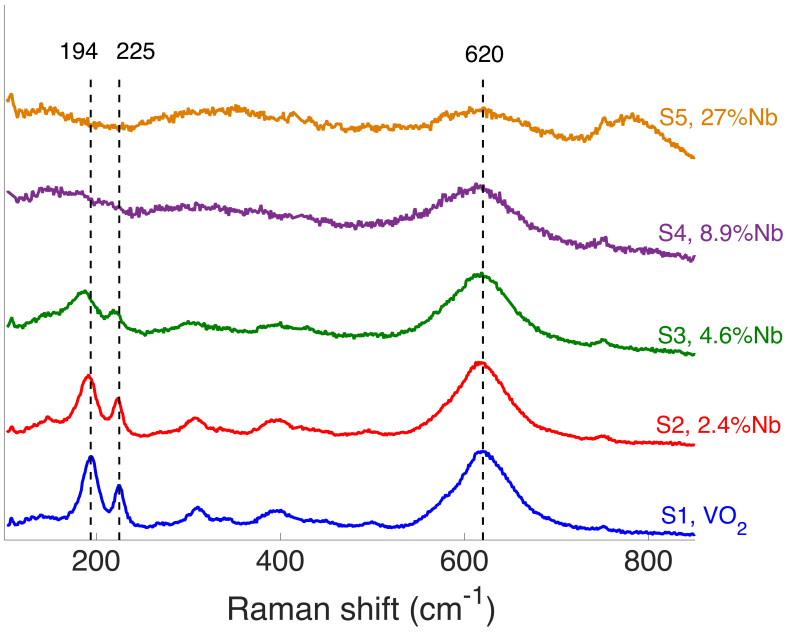


Figure A.1: Raman spectra of V-rich $V_xNb_{1-x}O_2$ films with different Nb concentration.

As is shown by the X-ray 2θ-ω scans in Figure A.2 (a), all films demonstrated peaks corresponding to (020) and (040) diffraction of monoclinic $VO_2$, which shifted to lower 2θ values with the increase of Nb concentration. Lattice parameters $b$ of monoclinic $VO_2$ ($b_M$), which correspond to $a$ of the rutile $VO_2$ ($a_R$), were extracted from the (020) peak positions and plotted as a function of Nb concentration in Figure A.2 (b). The increase of lattice parameter could be attributed to the larger size of Nb ions.

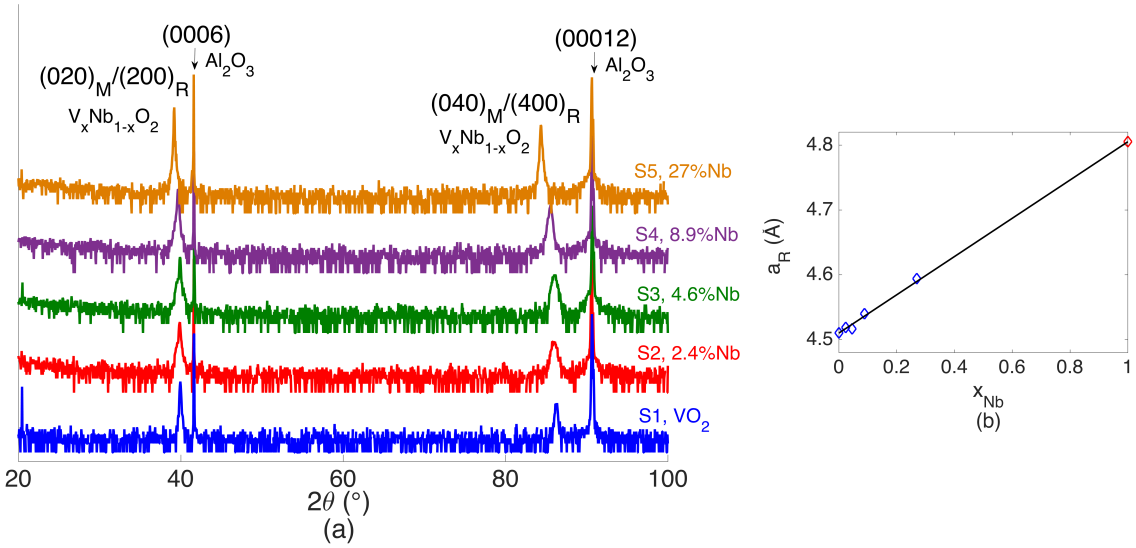


Figure A.2: (a) X-ray 2θ-ω scans from 20° to 100° of V-rich $V_xNb_{1-x}O_2$ films; (b) Depedence of lattice constant $a_R$ on Nb concentration, the solid line of Vegard's law is determined by lattice parameters of pure $NbO_2$ and $VO_2$.

Films resistivity as a function of temperature was characterized from 200 K to 400 K (Figure A.3 (a)). MIT with sizable discontinuity in film resistivity could be observed from curves of S1 (0% Nb), S2 (2.4% Nb) and S3 (4.6% Nb). For S4 with 8.9% Nb, the transition was significantly depressed but still visible. With the increase of Nb content in the film, the transition occurred at lower and wider temperature range, with a smaller resistivity discontinuity. Moreover, the width of hysteresis loop decreased with the increase of Nb concentration. For S5 with much higher Nb content (27%), the film exhibited semiconducting behaviors across the investigated temperature range, despite its regular rutile lattice. It could be explained by the disorder caused by impurity combining with the electron-electron correlation, which resulted in complete localization of carriers.

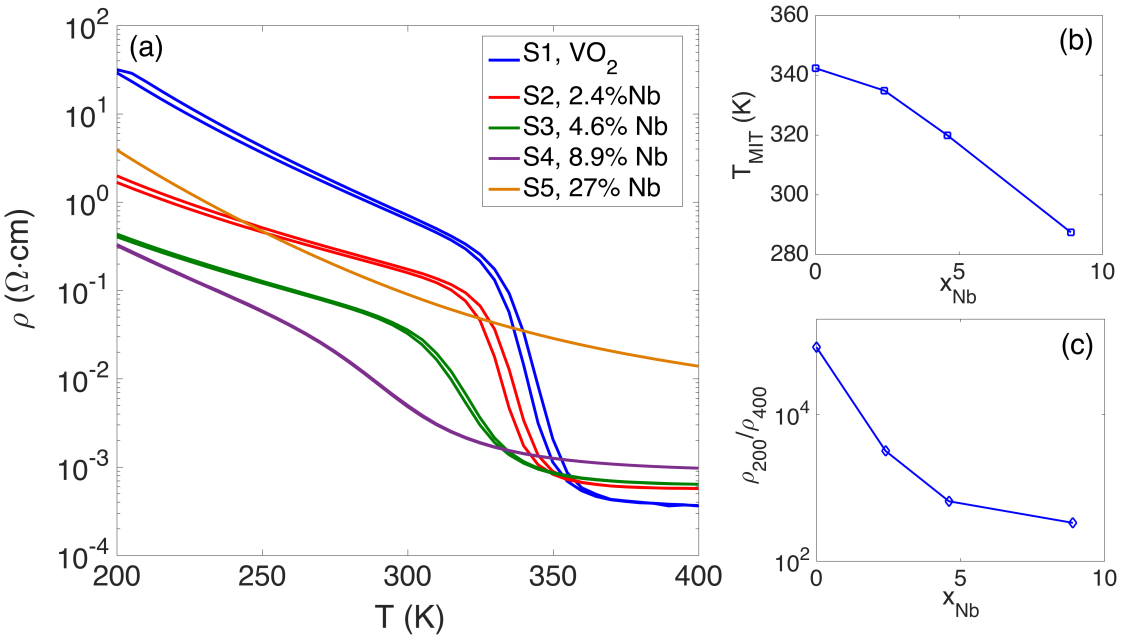


Figure A.3: (a) Temperature dependence of film resistivity of V-rich $V_xNb_{1-x}O_2$ films; (b) Variation of transition temperature $T_{MIT}$ and (c) the contrast between film resistivity at 200 K and 400 K $\rho_{200}/\rho_{400}$ with Nb concentration (for Samples S1 to S4).

# Bibliography


[1] You Zhou and Shriram Ramanathan. Correlated electron materials and field effect transistors for logic: a review. *Critical Reviews in Solid State and Materials Sciences*, 38(4):286–317, 2013.

[2] Zheng Yang, Changhyun Ko, and Shriram Ramanathan. Oxide electronics utilizing ultrafast metal-insulator transitions. *Annual Review of Materials Research*, 41:337–367, 2011.

[3] G Stefanovich, A Pergament, and D Stefanovich. Electrical switching and mott transition in $VO_2$. *Journal of Physics: Condensed Matter*, 12(41):8837, 2000.

[4] Tom Driscoll, H-T Kim, B-G Chae, Massimiliano Di Ventra, and DN Basov. Phase-transition driven memristive system. *Applied physics letters*, 95(4):043503, 2009.

[5] Federico Cilento, Claudio Giannetti, Gabriele Ferrini, Stefano Dal Conte, Tommaso Sala, Giacomo Coslovich, Matteo Rini, Andrea Cavalleri, and Fulvio Parmigiani. Ultrafast insulator-to-metal phase transition as a switch to measure the spectrogram of a supercontinuum light pulse. *Applied Physics Letters*, 96(2):021102, 2010.

[6] Zheng Yang, Changhyun Ko, Viswanath Balakrishnan, Gokul Gopalakrishnan, and Shriram Ramanathan. Dielectric and carrier transport properties of vanadium dioxide thin films across the phase transition utilizing gated capacitor devices. *Phys. Rev. B*, 82:205101, Nov 2010.

[7] F. J. Morin. Oxides which show a metal-to-insulator transition at the neel temperature. *Phys. Rev. Lett.*, 3:34–36, Jul 1959.

[8] Kimiko Sakata. Electrical and magnetic properties of $NbO_2$. *Journal of the Physical Society of Japan*, 26(3):867–867, 1969.

[9] R. F. Janninck and D. H. Whitmore. Electrical conductivity and thermoelectric power of niobium dioxide. *Journal of Physics and Chemistry of Solids*, 27(6-7):1183–1187, 1966.

[10] K. L. Chopra. Current-controlled negative resistance in thin niobium oxide films. *Proceedings of the IEEE*, 51(6):941–942, June 1963.

[11] Melissa R Beebe, J Michael Klopf, Yuhan Wang, Salinporn Kittiwatanakul, Jiwei Lu, Stuart A Wolf, and R Alejandra Lukaszew. Time-resolved light-induced insulator-metal transition in niobium dioxide and vanadium dioxide thin films. *Optical Materials Express*, 7(1):213–223, 2017.

[12] Carsten Funck, Stephan Menzel, Nabeel Aslam, Hehe Zhang, Alexander Hardtdegen, Rainer Waser, and Susanne Hoffmann-Eifert. Multidimensional simulation of threshold switching in nbo2 based on an electric field triggered thermal runaway model. *Advanced Electronic Materials*, 2(7):1600169–n/a, 2016. 1600169.

[13] S. Slesazeck, H. Mahne, H. Wylezich, A. Wachowiak, J. Radhakrishnan, A. Ascoli, R. Tetzlaff, and T. Mikolajick. Physical model of threshold switching in $NbO_2$ based memristors. *RSC Adv.*, 5:102318–102322, 2015.

[14] J. H. Lee, EJ Cha, YT Kim, BK Chae, JJ Kim, SY Lee, HS Hwang, and CG Park. A study of threshold switching of $NbO_2$ using atom probe tomography and transmission electron microscopy. *Micron*, 79:101–109, 2015.

[15] Nanoscale (∼10nm) 3D vertical reram and uppercase$NbO_2$ threshold selector with tin electrode. In *2013 IEEE International Electron Devices Meeting*, pages 10.5.1–10.5.4, Dec 2013.

[16] Brendan J. Kennedy Adrian A. Bolzan, Celesta Fong and Christopher J. Howard. A powder neutron diffraction study of semiconducting and metallic niobium dioxide. *Journal of Solid State Chemistry*, 113(1):9 – 14, 1994.

[17] Tobias Hadamek, Agham B. Posadas, Ajit Dhamdhere, David J. Smith, and Alexander A. Demkov. Spectral identification scheme for epitaxially grown single-phase niobium dioxide. *Journal of Applied Physics*, 119(9), 2016.

[18] Franklin J. Wong and Shriram Ramanathan. Heteroepitaxy of distorted rutile-structure $WO_2$ and $NbO_2$ thin films. *Journal of Materials Research*, 28:2555–2563, 9 2013.

[19] A. K. Cheetham and C. N. R. Rao. A neutron diffraction study of niobium dioxide. *Acta Crystallographica Section B*, 32(5):1579–1580, May 1976.

[20] V. Eyert. The metal-insulator transitions of $VO_2$: A band theoretical approach. *Annalen der Physik*, 11(9):650–704, 2002.

[21] RP Elliott. Columbium-oxygen system. *Trans. Am. Soc. Metals*, 52, 1960.

[22] M. P. F. Graca C. NIco, T. Monteiro. Niobium oxides and niobates physical properties: review and prospects. *Progress in Materials Science*, 80:1 – 37, 2016.

[23] Seonghyun Kim, Jubong Park, Jiyong Woo, Chunhum Cho, Wootae Lee, Jungho Shin, Godeuni Choi, Sangsu Park, Daeseok Lee, Byoung Hun Lee, and Hyunsang Hwang. Threshold-switching characteristics of a nanothin-$NbO_2$-layer-based

Pt/$NbO_2$/Pt stack for use in cross-point-type resistive memories. *Microelectronic Engineering*, 107:33 – 36, 2013.

[24] Franklin J Wong, Nina Hong, and Shriram Ramanathan. Orbital splitting and optical conductivity of the insulating state of $NbO_2$. *Physical Review B*, 90(11):115135, 2014.

[25] Agham B. Posadas, Andrew O'Hara, Sylvie Rangan, Robert A. Bartynski, and Alexander A. Demkov. Band gap of epitaxial in-plane-dimerized single-phase $NbO_2$ films. *Applied Physics Letters*, 104(9), 2014.

[26] Sung-Hun Lee, Ha-Na Yoon, Il-Sun Yoon, and Bong-Soo Kim. Single crystalline $NbO_2$ nanowire synthesis by chemical vapor transport method. *Bulletin of the Korean Chemical Society*, 33(3):839–842, 2012.

[27] Ye Zhao, Zhengjun Zhang, and Yuanhua Lin. Optical and dielectric properties of a nanostructured $NbO_2$ thin film prepared by thermal oxidation. *Journal of Physics D: Applied Physics*, 37(24):3392, 2004.

[28] John B Goodenough. The two components of the crystallographic transition in $VO_2$. *Journal of Solid State Chemistry*, 3(4):490–500, 1971.

[29] Shriram Ramanathan. *Thin Film Metal-Oxides: Fundamentals and Applications in Electronics and Energy*. Springer Science & Business Media, 2009.

[30] N. Beatham and A. F. Orchard. X-ray and UV photoelectron spectra of the oxides $NbO_2$, $MoO_2$ and $RuO_2$. *Journal of Electron Spectroscopy and Related Phenomena*, 16(1):77–86, 1979.

[31] Nan Jiang and John C. H. Spence. Electron energy-loss spectroscopy of the O-K edge of $NbO_2$, $MoO_2$, and $WO_2$. *Physical Review B*, 70(24):245117, 2004.

[32] David Adler. Mechanisms for metal-nonmental transitions in transition-metal oxides and sulfides. *Rev. Mod. Phys.*, 40:714–736, Oct 1968.

[33] Zhang Weibin, Wu Weidong, Wang Xueming, Cheng Xinlu, Yan Dawei, Shen Changle, Peng Liping, Wang Yuying, and Bai Li. The investigation of $NbO_2$ and $Nb_2O_5$ electronic structure by XPS, UPS and first principles methods. *Surface and Interface Analysis*, 45(8):1206–1210, 2013.

[34] J. C. Lee and W. W. Durand. Electrically stimulated optical switching of $NbO_2$ thin films. *Journal of Applied Physics*, 56(11):3350–3352, 1984.

[35] Yoshio Sakai, Nobuo Tsuda, and Tamio Sakata. Electrical properties of semiconducting $NbO_2$. *Journal of the Physical Society of Japan*, 54(4):1514–1518, 1985.

[36] Andrew O'Hara, Timothy N Nunley, Agham B Posadas, Stefan Zollner, and Alexander A Demkov. Electronic and optical properties of $NbO_2$. *Journal of Applied Physics*, 116(21):213705, 2014.

[37] Franklin J Wong and Shriram Ramanathan. Electrical transport in transition metal oxides. *Resistive Switching: From Fundamentals of Nanoionic Redox Processes to Memristive Device Applications*, pages 165–196, 2016.

[38] Alexander JE Rettie, William D Chemelewski, David Emin, and C Buddie Mullins. Unravelling small-polaron transport in metal oxide photoelectrodes. *The journal of physical chemistry letters*, 7(3):471–479, 2016.

[39] Issai Shlimak. *Is hopping a science?: selected topics of hopping conductivity*. World Scientific, 2015.

[40] David Emin. Small polarons. *Phys. Today;(United States)*, 35(6), 1982.

[41] Alexander J. E. Rettie, William D. Chemelewski, Jeffrey Lindemuth, John S. McCloy, Luke G. Marshall, Jianshi Zhou, David Emin, and C. Buddie Mullins. Anisotropic small-polaron hopping in W $BiVO_4$ single crystals. *Applied Physics Letters*, 106(2), 2015.

[42] Nevill Francis Mott and Edward A Davis. *Electronic processes in non-crystalline materials*. OUP Oxford, 2012.

[43] Allen Miller and Elihu Abrahams. Impurity conduction at low concentrations. *Phys. Rev.*, 120:745–755, Nov 1960.

[44] P. W. Anderson. Absence of diffusion in certain random lattices. *Phys. Rev.*, 109:1492–1505, Mar 1958.

[45] N Mott. The mobility edge since 1967. *Journal of Physics C: Solid State Physics*, 20(21):3075, 1987.

[46] M. Pollak. A percolation treatment of dc hopping conduction. *Journal of Non-Crystalline Solids*, 11(1):1 – 24, 1972.

[47] E. M. Hamilton. Variable range hopping in a non-uniform density of states. *Philosophical Magazine*, 26(4):1043–1045, 1972.

[48] Boris Isaakovich Shklovskii and Alex L Efros. *Electronic properties of doped semiconductors*, volume 45. Springer Science & Business Media, 2013.

[49] A Zabrodskii and K Zinov'eva. Low-temperature conductivity and metal-insulator transition in compensate n-Ge. *Zh. Eksp. Teor. Fiz*, 86:742, 1984.

[50] H Fritzsche. A general expression for the thermoelectric power. *Solid State Communications*, 9(21):1813–1815, 1971.

[51] Harald Böttger and Valerij V Bryksin. *Hopping conduction in solids*. VCH Weinheim, 1985.

[52] M. Pollak and B. Shklovskii. *Hopping Transport in Solids*. Modern Problems in Condensed Matter Sciences. Elsevier Science, 1991.

[53] J. M. Gallego and C. B. Thomas. Preparation and characterization of thin films of $NbO_2$. *Thin Solid Films*, 98(1):11–22, 1982.

[54] Z. K. Kun, W. E. Kramer, and G. W. Roland. The growth of homogeneous $NbO_2$ single crystals by the float zone method. *Journal of Crystal Growth*, 58(1):122–126, 1982.

[55] S. H. Shin, T. H. Halpern, and P. M. Raccah. Crystal growth and study of the stoichiometry of $NbO_2$. *Materials Research Bulletin*, 10(10):1061–1065, 1975.

[56] S. Nakao, H. Kamisaka, Y. Hirose, and T. Hasegawa. Electrical and optical properties of polycrystalline $NbO_2$ thin films grown by solid phase crystallization. In *2016 Compound Semiconductor Week (CSW)*, pages 1–1, June 2016.

[57] G. Belanger, J. Destry, G. Perluzzo, and P. M. Raccah. Electron transport in single crystals of niobium dioxide. *Canadian Journal of Physics*, 52(22):2272–2280, 1974.

[58] C Guerra-Vela and RJ Sladek. Electrical conduction in semiconducting $NbO_2$ at hydrostatic pressures up to 6000 atm. *Solid state communications*, 53(3):231–234, 1985.

[59] François Gervais. Temperature dependence of polar phonons, plasma excitations, and effective charges below the semiconducting-metal phase transition of $NbO_2$. *Physical Review B*, 23(12):6580, 1981.

[60] James A. Roberson and Robert A. Rapp. Electrical properties of NbO and $NbO_2$. *Journal of Physics and Chemistry of Solids*, 30(5):1119 – 1124, 1969.

[61] C. N. R. Rao, G. Rama Rao, and G. V. Subba Rao. Semiconductor-metal transitions in $NbO_2$ and $Nb_{1x}V_xO_2$. *Journal of Solid State Chemistry*, 6(3):340–343, 1973.

[62] T Sakata, K Sakata, and I Nishida. Study of phase transition in $NbO_2$. *physica status solidi (b)*, 20(2):K155–K157, 1967.

[63] D. V. Geppert. A new negative-resistance device. *Proceedings of the IEEE*, 51(1):223–223, Jan 1963.

[64] S. H. Chang, J. S. Lee, S. C. Chae, S. B. Lee, C. Liu, B. Kahng, D-W Kim, and T. W. Noh. Occurrence of both unipolar memory and threshold resistance switching in a NiO film. *Physical review letters*, 102(2):026801, 2009.

[65] Li He, Zhi-Min Liao, Han-Chun Wu, Xiao-Xue Tian, Dong-Sheng Xu, Graham LW Cross, Georg S Duesberg, IV Shvets, and Da-Peng Yu. Memory and threshold resistance switching in Ni/NiO core–shell nanowires. *Nano letters*, 11(11):4601–4606, 2011.

[66] Matthew D Pickett and R Stanley Williams. Sub-100 fj and sub-nanosecond thermally driven threshold switching in niobium oxide crosspoint nanodevices. *Nanotechnology*, 23(21):215202, 2012.

[67] A.L. Pergament, P.P. Boriskov, A.A. Velichko, and N.A. Kuldin. Switching effect and the metal–insulator transition in electric field. *Journal of Physics and Chemistry of Solids*, 71(6):874 – 879, 2010.

[68] You Zhou and Shriram Ramanathan. Correlated electron materials and field effect transistors for logic: a review. *Critical Reviews in Solid State and Materials Sciences*, 38(4):286–317, 2013.

[69] R.E. Peierls. *More Surprises in Theoretical Physics*. Princeton series in physics. Princeton University Press, 1991.

[70] http://phyx.readthedocs.io/en/latest/TI/Lecture

[71] N. F. Mott. *Metal-insulator transitions*. Taylor & Francis, London, 1990.

[72] Masatoshi Imada, Atsushi Fujimori, and Yoshinori Tokura. Metal-insulator transitions. *Reviews of Modern Physics*, 70(4):1039, 1998.

[73] N. F. Mott. Metal-insulator transition. *Reviews of Modern Physics*, 40(4):677, 1968.

[74] https://www.psi.ch/swissfel/the-origin-of-the-metal-insulator-transition-in-tas2.

[75] A. Zylbersztejn and N. F. Mott. Metal-insulator transition in vanadium dioxide. *Phys. Rev. B*, 11:4383–4395, Jun 1975.

[76] Volker Eyert. The metal-insulator transitions of $VO_2$: A band theoretical approach. *arXiv preprint cond-mat/0210558*, 2002.

[77] Andrew O'Hara and Alexander A. Demkov. Nature of the metal-insulator transition in $NbO_2$. *Phys. Rev. B*, 91:094305, Mar 2015.

[78] J. J. Quan, S. A. Wolf, and H. N. G. Wadley. Low energy ion beam assisted deposition of a spin valve. *Journal of Applied Physics*, 101(7), 2007.

[79] J. J. Quan, X. W. Zhou, L. He, R. Hull, and H. N. G. Wadley. Low energy ion assisted deposition of TaCu films. *Journal of Applied Physics*, 101(2), 2007.

[80] Kevin G. West, Jiwei Lu, Jiani Yu, David Kirkwood, Wei Chen, Yonghang Pei, John Claassen, and Stuart A. Wolf. Growth and characterization of vanadium dioxide thin films prepared by reactive-biased target ion beam deposition. *Journal of Vacuum Science & Technology A*, 26(1):133–139, 2008.

[81] Harold R. Kaufman. Technology of electron-bombardment ion thrusters. volume 36 of *Advances in Electronics and Electron Physics*, pages 265 – 373. Academic Press, 1975.

[82] Harold R. Kaufman, Raymond S. Robinson, and Richard Ian Seddon. Endhall ion source. *Journal of Vacuum Science & Technology A*, 5(4):2081–2084, 1987.

[83] V. V. Zhurin, H. R. Kaufman, J. R. Kahn, and T. L. Hylton. Biased target deposition. *Journal of Vacuum Science & Technology A*, 18(1):37–41, 2000.

[84] Gregory S Rohrer. *Structure and bonding in crystalline materials*. Cambridge University Press, 2001.

[85] Brian K . Tanner and D . Keith Bowen. *Thickness Metrology*, pages 31–46. CRC Press, 2016/08/02 2006.

[86] Brower D. T. Revay R. E. Huang T. C. A study of x-ray reflectivity data analysis methods for thin film thickness determination. *Powder Diffraction*, 11:114–116, 6 1996.

[87] A Gibaud and S Hazra. X-ray reflectivity and diffuse scattering. *CURRENT SCIENCE-BANGALORE-*, 78(12):1467–1477, 2000.

[88] Nicholas A. Geisse. AFM and combined optical techniques. *Materials Today*, 12(7-8):40 – 45, 2009.

[89] Peter Larkin. Chapter 2 - basic principles. In *Infrared and Raman Spectroscopy*, pages 7 – 25. Elsevier, Oxford, 2011.

[90] Quantum Design, 6325 Lusk Blvd. San Diego, CA 92121. *Physical Property Measurement System Thermal Transport Option User's Manual*, October 2002.

[91] Kevin G West, Jiwei Lu, Jiani Yu, David Kirkwood, Wei Chen, Yonghang Pei, John Claassen, and Stuart A Wolf. Growth and characterization of vanadium dioxide thin films prepared by reactive-biased target ion beam deposition. *Journal of Vacuum Science and Technology A: Vacuum, Surfaces and Films*, 26(1):133–139, 2008.

[92] Jiwei Lu, Kevin G. West, and Stuart A. Wolf. Very large anisotropy in the dc conductivity of epitaxial $VO_2$ thin films grown on (011) rutile $TiO_2$ substrates. *Applied Physics Letters*, 93(26), 2008.

[93] Salinporn Kittiwatanakul, Jiwei Lu, and Stuart A. Wolf. Transport anisotropy of epitaxial $VO_2$ films near the metal-semiconductor transition. *Applied Physics Express*, 4(9):091104, 2011.

[94] A. L. Bowman, T. C. Wallace, J. L. Yarnell, and R. G. Wenzel. The crystal structure of niobium monoxide. *Acta Crystallographica*, 21(5):843, Nov 1966.

[95] E Wimmer, K Schwarz, R Podloucky, P Herzig, and A Neckel. The effect of vacancies on the electronic structure of nbo. *Journal of Physics and Chemistry of Solids*, 43(5):439–447, 1982.

[96] Se-Hee Lee, Hyeonsik M. Cheong, Maeng Je Seong, Ping Liu, C. Edwin Tracy, Angelo Mascarenhas, J. Roland Pitts, and Satyen K. Deb. Microstructure study of amorphous vanadium oxide thin films using raman spectroscopy. *Journal of Applied Physics*, 92(4):1893–1897, 2002.

[97] SD Ross. The vibrational spectra of lithium niobate, barium sodium niobate and barium sodium tantalate. *Journal of Physics C: Solid State Physics*, 3(8):1785–1790, 1970.

[98] Philippe Colomban, François Romain, Arkady Neiman, and Irina Animitsa. Double perovskites with oxygen structural vacancies: Raman spectra, conductivity and water uptake. *Solid State Ionics*, 145(1–4):339 – 347, 2001. Proceedings of the 10th International Conference on Solid State Protonic Conductors.

[99] Yuan Hong-Tao, Feng Ke-Cheng, Wang Xue-Jin, Li Chao, He Chen-Juan, and Nie Yu-Xin. Effect of nonstoichiometry on raman scattering of $VO_2$ films. *Chinese Physics*, 13(1):82, 2004.

[100] Changhong Chen, Yong Zhao, Xuan Pan, V. Kuryatkov, A. Bernussi, M. Holtz, and Zhaoyang Fan. Influence of defects on structural and electrical properties of $VO_2$ thin films. *Journal of Applied Physics*, 110(2):023707, 2011.

[101] C. H. Griffiths and H. K. Eastwood. Influence of stoichiometry on the metalsemiconductor transition in vanadium dioxide. *Journal of Applied Physics*, 45(5):2201–2206, 1974.

[102] Changhong Chen and Zhaoyang Fan. Changes in $VO_2$ band structure induced by charge localization and surface segregation. *Applied Physics Letters*, 95(26):262106, 2009.

[103] RD Shannon. Revised effective ionic radii and systematic studies of interatomic distances in halides and chalcogenides. *Acta Crystallographica Section A: Crystal Physics, Diffraction, Theoretical and General Crystallography*, 32(5):751–767, 1976.

[104] Evgheni Strelcov, Alexander Tselev, Ilia Ivanov, John D Budai, Jie Zhang, Jonathan Z Tischler, Ivan Kravchenko, Sergei V Kalinin, and Andrei Kolmakov. Doping-based stabilization of the m2 phase in free-standing $VO_2$ nanostructures at room temperature. *Nano letters*, 12(12):6198–6205, 2012.

[105] A.Ann McConnell, J.S. Aderson, and C.N.R. Rao. Raman spectra of niobium oxides. *Spectrochimica Acta Part A: Molecular Spectroscopy*, 32(5):1067 – 1076, 1976.

[106] Bill X. Huang, Kang Wang, Jeffrey S. Church, and Ying-Sing Li. Characterization of oxides on niobium by raman and infrared spectroscopy. *Electrochimica Acta*, 44(15):2571 – 2577, 1999.

[107] S. Tanuma, C. J. Powell, and D. R. Penn. Calculations of electron inelastic mean free paths for 31 materials. *Surface and Interface Analysis*, 11(11):577–589, 1988.

[108] J.G. Bennett and R.J. Sladek. Low temperature elastic constants and debye temperature of $NbO_2$. *Solid State Communications*, 25(12):1035 – 1037, 1978.

[109] Alexander JE Rettie, Heung Chan Lee, Luke G Marshall, Jung-Fu Lin, Cigdem Capan, Jeffrey Lindemuth, John S McCloy, Jianshi Zhou, Allen J Bard, and C Buddie Mullins. Combined charge carrier transport and photoelectrochemical characterization of $BiVO_4$ single crystals: intrinsic behavior of a complex metal oxide. *Journal of the American Chemical Society*, 135(30):11389–11396, 2013.

[110] Lina Ben-dor and Y. Shimony. Crystal growth and phase transitions in the $Nb_xCr_{1-x}O_2$(x 0.5) system. *Journal of Crystal Growth*, 43(1):1 – 4, 1978.

[111] L. Ben-Dor and Y. Shimony. Structure and physical properties of the system $Nb_xCr_{1-x}O_2$. *Journal of Magnetism and Magnetic Materials*, 7(1):60 – 62, 1978.

[112] Kimiko Sakata. Study of the phase transition in $Nb_xTi_{1-x}O_2$. *Journal of the Physical Society of Japan*, 26(4):1067–1067, 1969.

[113] Larry A. Ladd and William Paul. Optical and transport properties of high quality crystals of $V_2O_4$ near the metallic transition temperature. *Solid State Communications*, 7(4):425 – 428, 1969.

[114] Yuhan Wang, Ryan B. Comes, Salinporn Kittiwatanakul, Stuart A. Wolf, and Jiwei Lu. Epitaxial niobium dioxide thin films by reactive-biased target ion beam deposition. *Journal of Vacuum Science & Technology A: Vacuum, Surfaces, and Films*, 33(2):021516, 2015.

[115] C.N.R. Rao, G.Rama Rao, and G.V.Subba Rao. Semiconductor-metal transitions in $NbO_2$ and $Nb_{1x}V_xO_2$. *Journal of Solid State Chemistry*, 6(3):340 – 343, 1973.

[116] I. K. Kristensen. Electrical transport properties in the pseudobinary system $NbO_2$-$VO_2$. *Journal of Applied Physics*, 40(12):4992–4994, 1969.

[117] G. Villeneuve, A. Bordet, A. Casalot, J.P. Pouget, H. Launois, and P. Lederer. Contribution to the study of the metal-insulator transition in the $V_{1x}Nb_xO_2$ system: I — crystallographic and transport properties. *Journal of Physics and Chemistry of Solids*, 33(10):1953 – 1959, 1972.

[118] Mei Pan, Jie Liu, Hongmei Zhong, Shaowei Wang, Zhi feng Li, Xiaoshuang Chen, and Wei Lu. Raman study of the phase transition in $VO_2$ thin films. *Journal of Crystal Growth*, 268(1–2):178 – 183, 2004.

[119] E Arcangeletti, L Baldassarre, D Di Castro, S Lupi, L Malavasi, C Marini, A Perucchi, and P Postorino. Evidence of a pressure-induced metallization process in monoclinic $VO_2$. *Physical review letters*, 98(19):196406, 2007.

[120] C. Marini, E. Arcangeletti, D. Di Castro, L. Baldassare, A. Perucchi, S. Lupi, L. Malavasi, L. Boeri, E. Pomjakushina, K. Conder, and P. Postorino. Optical properties of $V_{1-x}Cr_xO_2$ compounds under high pressure. *Physical review. B, Condensed matter and materials physics*, 77(23):235111, 2008.

[121] A.Ann McConnell, J.S. Aderson, and C.N.R. Rao. Raman spectra of niobium oxides. *Spectrochimica Acta Part A: Molecular Spectroscopy*, 32(5):1067 – 1076, 1976.

[122] Franklin D Hardcastle and Israel E Wachs. Determination of niobium-oxygen bond distances and bond orders by raman spectroscopy. *Solid State Ionics*, 45(3-4):201–213, 1991.

[123] Michael E. A. Warwick and Russell Binions. Advances in thermochromic vanadium dioxide films. *Journal of Materials Chemistry A*, 2(10):3275–3292, 2014.

[124] A. Zylbersztejn and N. F. Mott. Metal-insulator transition in vanadium dioxide. *Phys. Rev. B*, 11:4383–4395, Jun 1975.

[125] Shuai Li, Xinjun Liu, Sanjoy Kumar Nandi, Dinesh Kumar Venkatachalam, and Robert Glen Elliman. Temperature dependence of threshold switching in $NbO_x$ thin films. In *2014 Conference on Optoelectronic and Microelectronic Materials & Devices*, pages 138–140. IEEE, 2014.

[126] Matthew D Pickett and R Stanley Williams. Sub-100 fJ and sub-nanosecond thermally driven threshold switching in niobium oxide crosspoint nanodevices. *Nanotechnology*, 23(21):215202, 2012.

[127] Fu-Chien Chiu. A review on conduction mechanisms in dielectric films. *Advances in Materials Science and Engineering*, 2014(Article ID 578168), 2014.

[128] John G. Simmons. Transition from electrode-limited to bulk-limited conduction processes in metal-insulator-metal systems. *Phys. Rev.*, 166:912–920, Feb 1968.

[129] S.M. Sze. *Semiconductor devices, physics and technology*. Wiley, 1985.

[130] John G. Simmons. Generalized formula for the electric tunnel effect between similar electrodes separated by a thin insulating film. *Journal of Applied Physics*, 34:1793–1803, 1963.

[131] S. H. Shin, T. Halpern, and P. M. Raccah. High-speed high-current field switching of $NbO_2$. *Journal of Applied Physics*, 48(7):3150–3153, 1977.

[132] M Pollak and I Riess. A percolation treatment of high-field hopping transport. *Journal of Physics C: Solid State Physics*, 9(12):2339, 1976.

[133] Dong Yu, Congjun Wang, Brian L Wehrenberg, and Philippe Guyot-Sionnest. Variable range hopping conduction in semiconductor nanocrystal solids. *Physical review letters*, 92(21):216802, 2004.

[134] Chun Y Cheah and Alan B Kaiser. Variable-range hopping transport: crossovers from temperature dependence to electric field dependence in disordered carbon materials. *International Journal of Nanotechnology*, 11(5-678):412–418, 2014.

[135] Ee Wah Lim and Razali Ismail. Conduction mechanism of valence change resistive switching memory: A survey. *Electronics*, 4(3):586–613, 2015.

[136] M. Delheusy, A. Stierle, N. Kasper, R. P. Kurta, A. Vlad, H. Dosch, C. Antoine, A. Resta, E. Lundgren, and J. Andersen. X-ray investigation of subsurface interstitial oxygen at Nb/oxide interfaces. *Applied Physics Letters*, 92(10), 2008.

[137] S. Venkataraj, R. Drese, O. Kappertz, R. Jayavel, and M. Wuttig. Characterization of niobium oxide films prepared by reactive dc magnetron sputtering. *physica status solidi (a)*, 188(3):1047–1058, 2001.

[138] M.Ghanashyam Krishna and A.K. Bhattacharya. Processing and size effects on the optical properties of sputtered oxide thin films. *Materials Science and Engineering: B*, 86(1):41 – 47, 2001.

[139] Geoffrey W. Burr Rohit S. Shenoy Kumar Virwani Pritish Narayanan Alvaro Padilla and Bülent Kurdi. Access devices for 3D crosspoint memory. *Journal of Vacuum Science & Technology B*, 32(4), 2014.

[140] Hannes Mähne, Helge Wylezich, Stefan Slesazeck, Thomas Mikolajick, Jozef Vesely, Volker Klemm, and David Rafaja. Room temperature fabricated $NbO_x/Nb_2O_5$ memory switching device with threshold switching effect. In *2013 5th IEEE International Memory Workshop*, pages 174–177. IEEE, 2013.

[141] Jieun Bae, Inrok Hwang, Yuhyun Jeong, Sung-Oong Kang, Sahwan Hong, Jong-wan Son, Jinsik Choi, Jinsoo Kim, June Park, Maeng-Je Seong, et al. Coexistence of bi-stable memory and mono-stable threshold resistance switching phenomena in amorphous $NbO_x$ films. *Applied Physics Letters*, 100(6):062902, 2012.

[142] Xinjun Liu, Sharif Md Sadaf, Myungwoo Son, Jubong Park, Jungho Shin, Wootae Lee, Kyungah Seo, Daeseok Lee, and Hyunsang Hwang. Co-occurrence of threshold switching and memory switching in cells for crosspoint memory applications. *IEEE Electron Device Letters*, 33(2):236–238, 2012.

[143] Salinporn Kittiwatanakul, Stuart A Wolf, and Jiwei Lu. Large epitaxial bi-axial strain induces a mott-like phase transition in $VO_2$. *Applied Physics Letters*, 105(7):073112, 2014.